2012

Physical and Thermal Properties of Zirconium Tungstate Nanoparticles with Different Morphologies from Hydrothermal Synthesis

Hongchao Wu
Iowa State University

Physical and thermal properties of zirconium tungstate nanoparticles with different morphologies from hydrothermal synthesis

By**: Hongchao Wu**

A thesis submitted to the graduate faculty

in partial fulfillment of the requirements for the degree of

MASTER OF SCIENCE

Major: Materials Science and Engineering

Program of Study Committee:
Michael R. Kessler - Major Professor
Mufit Akinc
David Grewell

Iowa State University

Ames, Iowa

2012

Table of Contents

Acknowledgements

There is no goal achieved without the support of others, and no achievement obtained solely on one's own efforts. I would like to recognize those who have provided me with assistance and guidance during my two years of graduate study at Iowa State University.

First, I would like to thank my beloved parents for their significant financial support and ever-lasting spiritual encouragement. I would thank my major professor Dr. Michael Kessler for his continued support and advice on this project. I would also thank my committee members, Dr. Mufit Akinc and Dr. David Grewell for their valuable suggestions on my thesis. I would like to especially show my gratitude to my previous research advisor Dr. Prashanth Badrinarayanan for his significant instructions and suggestions on my initial research work and my journal manuscript. Furthermore, I have much appreciation for Dr. Mohammad Ahmad for his important suggestions on BET data analysis and XRD pattern refinements; Dr. Matthew Besser for assistance with the isothermal X-ray diffraction measurements; and graduate student Keenan Deutsch for his BET measurement. In addition, I should thank my lab assistant advisor Dr. Michael Martin for the opportunity to be an assistant in the Department of Materials Science and Engineering for a year and half. I also want to thank my research group member Mark Rogalski for his instruction and assistance of synthesis of zirconium tungstate nanoparticles and thermomechanical characterization of epoxy nanocomposites. Also, thanks to the research group members for their support during my research. I have immense gratitude for my dear friends Qin Ma, Weijie Yu and many others for their support while living in Ames. At last, I thank Iowa State University providing me with such valuable opportunity to pursue further education in my life.

Abstract

Negative thermal expansion (NTE) materials belong to a group of solids that perform contractions in volume under heating conditions, instead of thermal expansion observed in most other solids. Due to this special negative thermal property, NTE materials are gradually drawing research interest for their potential application as fillers in composites used to control thermal stress' generating from mismatch of thermal expansivity and to govern the overall thermal expansion behavior.

Zirconium tungstate (ZrW_2O_8) is a ceramic material that exhibits strong, isotropic NTE over a wide temperature range from 0.3 to 1050 K. The formation and transition of three phases ZrW_2O_8 can be achieved under certain temperatures and pressures. ZrW_2O_8 nanoparticles can be synthesized at lower temperatures by hydrothermal reaction followed by a subsequent heat treatment by converting the precursor $ZrW_2O_7(OH)_2 \cdot 2H_2O$ to ZrW_2O_8. However, nano-sized ZrW_2O_8 was reported to display a hydration phenomena when exposed to ambient external conditions. Through the careful selection of experimental parameters such as initial reactant types, acids types and concentrations, as well as reaction time and temperature, the effect of reaction conditions on morphologies and crystallite sizes of ZrW_2O_8 nanoparticles was characterized using scanning electron microscopy and powder X-ray diffraction. Three types of ZrW_2O_8 nanoparticles with distinct morphologies and crystallite size-scales were chosen for characterization and comparison. Thermal and physical properties, as well as the hydration problem, were compared using various techniques, including isothermal X-ray diffraction, Brunauer-Emmett-Teller (BET) surface area analyzer and thermogravimetric analysis. It was found that the synthesized ZrW_2O_8 nanoparticles present more negative CTE values than bulk-scaled in α-phase, and the CTE is dependent on the crystallite sizes of nanoparticles. All three

types of nanoparticles underwent different extents of hydration problem originated from moisture adsorption, which is determined by pores structure formed by agglomeration of nanoparticles. It was observed that ZrW_2O_8 nanoparticles with smaller dimensional sizes tended to form large pores and suffered from most severe hydrations.

Chapter 1. Introduction

1.1 Negative thermal expansion materials

The majorities of solid materials contain a positive coefficient of thermal expansion (CTE) and undergo an expansion in volume upon heating. The simplest level of thermal expansion can be illustrated by the asymmetry of the potential well of a diatomic molecule[1, 2]: As temperature increases, the gradual population of higher energy vibrational modes gives rise to an increase in the interatomic distances.

However, there are several materials that show the negative CTE values and exhibit a contraction in volume with a rise temperature. Such solids have important applications in composites materials to tailor the overall thermal expansion behavior. They are especially useful for zero expansion composites that can be utilized in high precision optical mirrors, fiber optic systems and the packaging industry[2]. The majority of materials that show the negative thermal expansion (NTE) behavior are oxides with a linear metal-oxygen-metal linkage and corner sharing MO_x polyhedral frame structure as shown Fig. 1-1. The heat absorption will excite the vibrations in the transverse direction of the oxygen atoms and cause a reduction in structure volume[3]. The NTE materials can be categorized into the structural families of cubic AM_2O_7 [2, 4, 5], cubic AM_2O_8 [6-8] and orthorhombic $A_2(MO_4)_3$ [9, 10], whose oxygen atom is connected by two metal atoms to form an open flexible structure. For the cubic AM_2O_7 structures, the typical example of such materials is ZrV_2O_7. The origin of NTE behavior is from the rotations of VO_4 tetrahedral and distortion of ZrO_6 octahedral[4]. In case of $A_2(MO_4)_3$, where octahedral A cationic site can be occupied by a trivalent cation (Sc^{3+}, Al^{3+}) and a tetrahedral M cationic site can be occupied by Mo^{6+} and W^{6+}, the transverse thermal vibrations occur in A-O-M linkages giving rise to the NTE

behavior. Cubic AM_2O_8 (A=Zr, Hf; M=W, Mo) is another well acknowledged structure family of materials that display the negative thermal expansion behavior. The most important and widely studied one is zirconium tungstate (ZrW_2O_8), which exhibits very strong and isotropic NTE over a wide temperature range from 0.3 to 1050 K[7].

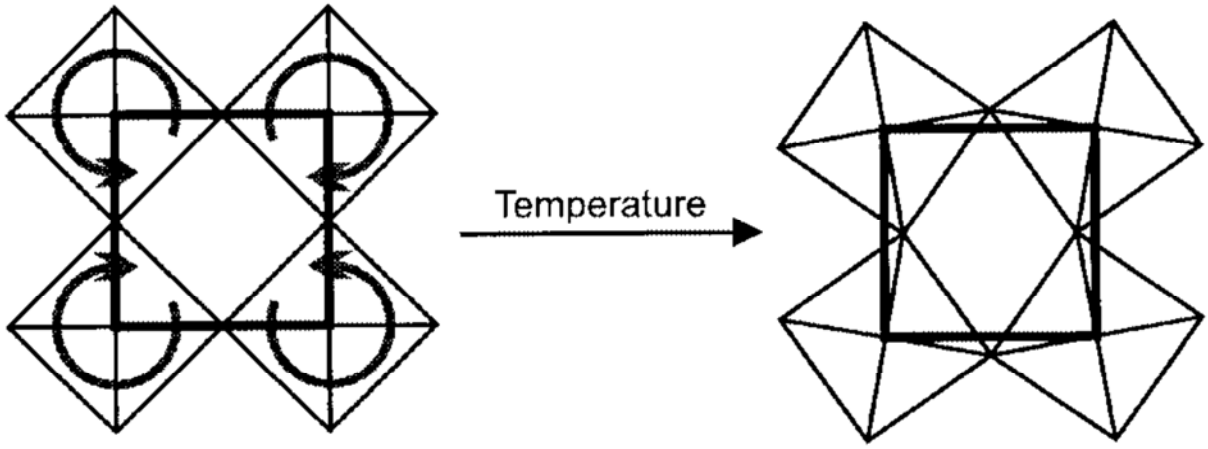

Fig. 1-1 A schematic representation of transverse vibrations of Metal-Oxygen-Metal bonds results in the NTE behavior in open framework of oxides[2].

1.2 Phase transition and NTE behavior in ZrW_2O_8

At room temperature, ZrW_2O_8 is in metastable state since it can only be thermodynamically stable from 1378 to 1530 K. As heating up to 1050 K, ZrW_2O_8 decomposes into ZrO_2 and WO_3[11]. Fig. 1-2 shows a cubic ZrW_2O_8 structure that consists of corner sharing ZrO_6 octahedra (in green) and WO_4 tetrahedra (in red). Each WO_4 tetrahedron only shares three of its four oxygen atoms and leaves an oxygen atom in free position[12]. Due to the uniquely flexible metal-oxygen-metal linkage, the transvers vibration of the oxygen atom, connected between the Zr and W atoms, excited at a low thermal energy results in small counter-rotations

of WO_4 and ZrO_2 polyhedra. This is the origin of the negative thermal expansion properties of ZrW_2O_8, and is also termed as a “quasi-rigid unit mode” by A. Pryde and coworkers[5, 13].

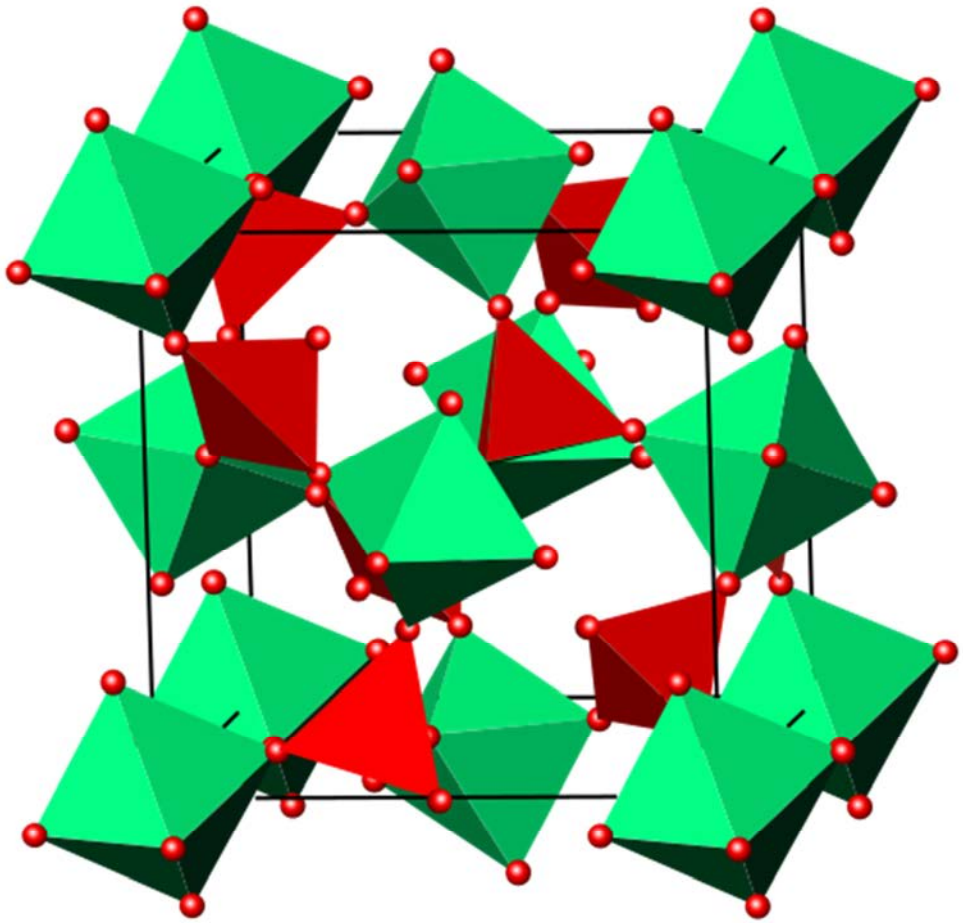

Fig. 1-2 Polyhedral representation of cubic crystal structure of ZrW_2O_8

To our knowledge, there are three phases of ZrW_2O_8 existence under certain temperature and pressure conditions. An early study on NTE behavior of ZrW_2O_8, done by A. Sleight and coworkers[7], revealed that discontinuous changes of expansion at 430 K is observed in the temperature range of 0.3 to 1050 K, which indicates a reversible order-disordered α-β phase transition. Below 430 K, α phase ZrW_2O_8 shows the cubic crystal structure (space group $P2_13$) with the CTE value of -8.8×10^{-6} °C^{-1}. When ZrW_2O_8 is heated above 430 K, α-ZrW_2O_8

transforms into β-ZrW_2O_8 with CTE of -4.9 × 10^{-6} °C^{-1} (space group $Pa\bar{3}$) due to the disordering of WO_4 tetrahedra[7]. The mechanism of the phase transition from acentric to centric cubic also stems from the special flexible structure of ZrW_2O_8: At low temperatures, since the corner-sharing structure of ZrO_6 and WO_3 led to $ZrW_2O_6^{4+}$, the two free oxygen ions coordinate with the tungsten atom to form WO_4 groups. At higher temperatures, the positions of the two terminal oxygen ions become disordered and migrate to the position that bonds with two WO_4 tetrahedra groups with equal probabilities[2].

Another irreversible phase transition of ZrW_2O_8 was observed and reported by J. Evans *et al* in 1997[14]. It is shown that γ-ZrW_2O_8 can be obtained under pressures at 0.2 GPa from α-ZrW_2O_8. The γ-phase with orthorhombic structure (space group $P2_12_12_1$) can be reverted back to α-phase under heating at 393 K and ambient pressure. In this irreversible transition process, about 5% reduction in volume is observed, which is caused by the migration of oxygen atoms bonded to the tungsten atom[14]. It is noted that γ-ZrW_2O_8 also exhibits negative CTE but one order of magnitude less than cubic α-ZrW_2O_8 due to the lowering of framework flexibility, which is assumed to be contributed to the less pronounced negative thermal expansion characteristic.

When the applied pressure reaches a higher level, an irreversible amorphization of ZrW_2O_8 is present. C. Perottoni and J. Jornada[15] reported that orthorhombic γ-ZrW_2O_8 undergoes pressure induced amorphization starting from 1.5 GPa to above 3.5 GPa with no Bragg peaks observed. Although the amorphous zirconium tungstate can be preserved after removal of the external pressure, it can be recrystallized into α-ZrW_2O_8 under ambient pressure upon heating above 923 K[15]. In recent years, several studies have been done to understand the ZrW_2O_8 and

$ZrMo_2O_8$'s amorphization mechanism by investigating the changes in microscopic local structure[16-20].

1.3 Synthesis of ZrW_2O_8

A wide variety of methods have been reported for the synthesis of ZrW_2O_8. In 1959, J. Graham and coworkers[21] first reported the successful synthesis of ZrW_2O_8 by the traditional solid state reaction followed by quenching to avoid decomposition of ZrO_2 and WO_3. Due concerns regarding the quality of synthesized ZrW_2O_8 with this method and the importance of exploring alternative methods, several researches investigated the sol-gel routes to synthesize ZrW_2O_8[22, 23]. M. Dadachov and R. Lambrecht[24] revealed that the hydrothermal method facilitated the formation of single crystalline ZrW_2O_8 at a lower temperature. C. Georgi and H. Kern[25] reported a ZrW_2O_8 preparation method by an amorphous citrate process.

Although several methods are available for synthesis of zirconium tungstate, only two methods are reported to be effective for synthesis of nano-scaled zirconium tungstate. The first method is the combination of sol-gel and reverse micelle methods reported by Sullivan and Lukenhart[26] in 2005. Yet, there is a small amount of impurity of WO_3 in the synthesized ZrW_2O_8 that restricts its application. The hydrothermal reaction method, is the most widely applied for synthesis of pure and highly crystallized nanoparticles. In this method, the precursor of AM_2O_8, hydroxide hydrate $AM_2O_7(OH)_2 \cdot 2H_2O$, can be obtained from a certain combination of reactants reacting in an acidic medium at a high temperature and high pressure; then the cubic AM_2O_8 can be obtained through a calcination process to dehydrate the precursor. In recent years, several works reported on the synthesis of optimized ZrW_2O_8 nanoparticles by investigating the experimental variables in the hydrothermal reaction. Q. Xing *et al.* [27] and X. Xing *et al.*[28] investigated the crystallization and growth of ZrW_2O_8 nanorods by altering the acidity of the

reaction medium. J. Colin *et al.*[29] conducted a more detailed study of the effects of experimental conditions, including acid types and concentration, reaction temperature and time on morphologies via the hydrothermal method. He found that higher concentrations of counter ions with the presence of chloride ions significantly improved crystallization kinetics of nanoparticles in an acidic solution. Kozy and coworkers[30] reported that the hydrothermal synthesis of ZrW_2O_8 nanoparticles with width of 10 to 15 nm and length up to 500 nm depended on the reaction conditions. They also reported that non-agglomerated and individual nanoparticles could be produced by using a mixture solution of high concentrations of acids and 1-butanol. The hydrothermal method is a widely studied synthesis method not only for ZrW_2O_8, but also for Mo-substituted ZrW_2O_8 and $ZrMo_2O_8$. In previous works, C. Lind *et al.*[6] and S. Allen *et al.*[31] reported that synthesized the cubic $ZrMo_2O_8$ can be obtained from dehydration of $ZrMo_2O_7(OH)_2 \cdot 2H_2O$ in hydrothermal reaction. Besides that, several studies of the nano-sized $ZrW_{2-x}Mo_xO_8$ were conducted and proved to be effective using the hydrothermal route[32-34].

1.4 Hydration phenomena of nano-sized ZrW_2O_8

The hydration of zirconium tungstate imposes a potential problem that will limit the practical application of ZrW_2O_8. The first study revealing the hydrated cubic $ZrW_2O_8 \cdot xH_2O$ synthesized by the hydrothermal method was reported by N. Duan *et al.*[35]. Water insertion of ZrW_2O_8 not only causes the collapse of structure framework and a 10 vol% contraction with no changes in Zr-O or W-O bond length by the increase of tungsten coordination and slight twisting of ZrO_6 octahedra, but also changes in space group from $P2_13$ to $Pa\bar{3}$. It was reported that , the unit cell parameter changes from 9.15 Å to 8.84 Å followed with CTE for water-inserted ZrW_2O_8 displayed weakly positive values as 1 mole of water inserted in 1 mole of ZrW_2O_8 to form $ZrW_2O_8 \cdot 1H_2O$[35]. In the recent study by N. Banek and coworkers[36] regarding the

autohydration of nano-sized cubic ZrW_2O_8, indicated that the origin of nano-sized ZrW_2O_8 hydration was attributed to the increasing defect sites on the surface of nanoparticles which formed during the synthesis with the addition of alcohol for the unagglomeration of ZrW_2O_8 nanoparticles. However, no further detailed information was revealed about how the defects and surface area of nanoparticles effect he hydration reaction.

1.5 ZrW_2O_8 composites

Due to the significance of NTE, zirconium tungstate can be used as filler integreated into various materials to produce composites with the controllable CTE. Previously, several research projects on composites with ZrW_2O_8 were done by choosing metal and ceramic as the matrix materials. X. Yang and coworkers[37] reported that ZrO_2/ZrW_2O_8 composites synthesized with weight ratio of ZrO_2 and WO_3 was 2.5:1 showed a nearly zero CTE value (0.67×10^{-6} K^{-1}). X. Yan and coworkers[38] reported that CTE of Cu/ZrW_2O_8 composites achieved to 4.85×10^{-6} K^{-1} when 65 vol% of ZrW_2O_8 was applied. J. Tani and coworkers[39] reported that CTE of Phenolic/ZrW_2O_8 composites decreased from 46×10^{-6} to 14×10^{-6} K^{-1} when increased filler loadings from 0 to 52 vol% were applied.

However, the most applicable ZrW_2O_8 composites are based on a polymer matrix. These are the most applicable not only for being inexpensive and their easy processing method, but also for their ability to facilitate the formation of a homogeneous mixture when combined with ZrW_2O_8. Sullivan and Lukenhart[26] first reported ZrW_2O_8/polyimide composites that with 22 vol% micron-sized ZrW_2O_8 resulted in 30% reduction in CTE. P. Badrinarayanan and coworkers[40] reported a 92% reduction in CTE of ZrW_2O_8/cyanate ester resin can be achieved by the incorporation of 65 vol% micron-sized ZrW_2O_8. The size of filler may critically influence the performance and processing of the composite. On one hand, the properties of nano-scale

materials have been shown to be significantly different from bulk properties of the same material. For example, nano-sized copper oxide (CuO) was observed to display a negative CTE value of -1.1 × 10^{-4} K^{-1} compared with the positive CTE of bulk CuO under the same temperature ranges[41]. In previous work, Badrinarayanan, P. and coworkers[42] observed differences in the α-phase thermal expansion behavior between bulk ZrW_2O_8 and ZrW_2O_8 nanoparticles synthesized through either the sol-gel or hydrothermal method, with the nanoparticles exhibiting greater magnitude of negative CTE values in the α-phase. On the other hand, due to smaller particles with larger surface areas this facilitates good particle dispersion in polymer matrices. A reduction of particle size to the nano-scale could help achieve optimal performance with lower loadings. For instance, it has been reported that using only 2 wt% of nano-silica in epoxy thin film composites can achieve equivalent mechanical properties and thermal stability as the composite with a micron-silica loading of 15 wt% and 30 wt%, respectively[43]. Thus, polymer nanocomposites that incorporate nano-sized ZrW_2O_8 opens a new realm for investigation of tailoring thermal expansion for applications that are widely used in microelectronic devices and aerospace facilities. One of the recent works done by P. Badrinarayanan and M. Kessler[44] revealed that a 10 vol% of ZrW_2O_8 nanoparticles synthesized by a hydrothermal reaction gave rise to a 20% reduction in CTE.

Apart from reducing the size-scale of the filler, it is necessary to perform proper surface treatment to the ZrW_2O_8 when mixing it with different polymer melts. The hydroxyl groups on the synthesized ZrW_2O_8 nanoparticles surface may be compatible with epoxy resin, but failed to show promising interactions with polyimides[45]. The goal of surface functionalization is to improve the compatibility between the modified filler and the matrix, and alter the physical

properties of the composites. Thus, nano-sized unagglomerated ZrW_2O_8 with proper surface functionalization is the key to produce nanocomposites with superior performance.

1.6 Research objective

The research project includes two sections in this thesis: First, is work focusing on synthesis of zirconium tungstate nanoparticles with different morphologies and crystallite sizes, by controlling the experimental parameters during the hydrothermal reaction; this is discussed in Chapter 3. A systemic study of the comparison of raw materials, types and concentrations of acids, reaction time and temperature on morphologies and crystallite sizes of ZrW_2O_8 was investigated.

The second part of the research is to study of the effect of ZrW_2O_8 nanoparticles morphology and crystallite sizes, on negative thermal properties and on the extent of hydration; this is discussed in Chapter 4. Three types of synthesized ZrW_2O_8 nanoparticles with distinct morphologies and crystallite sizes were chosen for the characterization CTE values. Explanation of the origin of the hydration phenomena was studied by characterizing the pore structure formed in nanoparticles.

Chapter 2 Experimental techniques

2.1 Materials

To synthesize ZrW_2O_8 nanoparticles, different initial compounds were selected, including: zirconium oxynitrate hydrate ($ZrO(NO_3)\cdot xH_2O$), zirconium acetate (ZrAc) solution in dilute acetic acid (Zr 16%), and zirconium perchlorate hydrate ($ZrO(ClO_4)_2\cdot xH_2O$), sodium tungstate dihydrate ($Na_2WO_4\cdot 2H_2O$), ammonium metatungstate hydrate ($(NH_4)_6H_2W_{12}O_{40}\cdot xH_2O$), and sodium metatungstate hydrate ($Na_6W_{12}O_{39}\cdot xH_2O$) was chosen as the tungsten source for all synthesis experiments. All chemicals were purchased from Sigma-Aldrich (St Louis, MO).

2.2 Synthesis

A hydrothermal reaction is a synthesis method for the crystallization of phases of an aqueous solution under a high temperature and vapor pressure. Originally, the term “hydrothermal” was used in the field of geology. Currently, a hydrothermal reaction is a widely used method for the synthesis of crystalline materials where the reaction is oftern carried out in a Teflon vessel sealed in a stainless autoclave. The major advantage of hydrothermal synthesis is it facilitates the crystallization of a single crystal product with good quality, which is especially advantageous for the crystalline phases that are unstable at their melting temperatures. Besides that, since the reaction proceeds under a high temperature and high pressure, the reactions efficiency can be improved due to the higher solubility of the reactants in the solvents. Based on the merits of hydrothermal synthesis, various kinds of compounds can be synthesized by hydrothermal reaction, including oxides, molybdates, carbonates and silicates, etc.

Zirconium tungstate hydroxide hydrate, the precursor of zirconium tungstate was obtained by a hydrothermal reaction in an acidic solution. The molarity ratio of zirconium to tungstate was 0.08/0.10 for all experiments, as mentioned by Kozy and coworkers[30] since it

facilitates the smallest average particle size. In order to synthesize nanoparticles with different morphologies, several reaction variables were attempted including raw reactants, acids types and concentration, reaction time, and reaction temperature. To examine the effect of the initial reactants, different compounds of zirconium and tungstate were selected for synthesis experiments.

The raw material compositions for a typical experiment consisted of 0.259 g $ZrO(NO_3)\cdot xH_2O$ (or 0.347 g $ZrO(ClO_4)_2\cdot xH_2O$ or 1.544 g ZrAc solution) and 0.330 g $Na_2WO_4\cdot 2H_2O$ (or 0.242 g $(NH_4)_6H_2W_{12}O_{40}\cdot xH_2O$ or 0.2347 g $Na_6W_{12}O_{39}\cdot xH_2O$). Each were dissolved separately in a specific amount of deionized water to prepare the reacting solutions. Both solutions were then combined slowly and simultaneously in a 23 ml Teflon Parr Bomb to form a mixture. The solutions were stirred continuously for several minutes, followed by the slow addition of the acid solution (5 M, 7 M of HCl or 3 M, 5 M of $HClO_4$) where white precipitates formed during mixing. In case of adding $HClO_4$, 2.758 g NaCl was needed to provide a chloride source and to accelerate the reaction kinetics according to previous work[30]. The total solution occupied 41% of the Teflon Parr Bomb's volume. After fully mixing the solution for several minutes, the Teflon Parr Bomb vessel was sealed and placed in a convection oven to facilitate a reaction at set temperatures (130 °C or 160 °C) and times (12 h or 24 h). After the completion of the reaction, the white precipitates were removed from the Parr Bomb vessel and centrifuged approximately 5 to 6 times with deionized water to remove any residual acids. After drying in a vacuum oven at 75 °C for 24 h, a fine and white powder of the precursor $ZrW_2O_7(OH)_2\cdot 2H_2O$ was obtained by gently grinding the mixture with a mortar and pestle. The final product of ZrW_2O_8 powders was obtained by performing the calcination of the precursor at 600 °C for 30 min

2.3 Characterization

Several techniques were employed for the characterization of prepared zirconium tungstate nanoparticles, including X-ray diffraction (XRD), isothermal X-ray diffraction, scanning electron microscopy (SEM), thermogravimetric analysis (TGA), and Brunauer-Emmett-Teller (BET) surface area analysis.

2.3.1 X-ray diffraction (XRD)

X-ray diffraction is an optical characterization technique widely used to characterize crystalline materials due to the nature of the diffraction (i.e. Bragg's Law: $n\lambda = 2dsin\theta$). A repeating lattice governs the diffraction pattern, where atoms are fixed in periodic positions within crystalline unit cells. In addition, XRD can also be performed on semi-crystalline and amorphous materials to extract useful information about the structure of the samples.

Initial diffraction patterns are a result of scattering the material's electron cloud, and then subsequent diffraction occurs due to the interference from the scattered wave fronts. The conditions for maximum diffraction intensity are formulated in Bragg's law, which is depicted in Fig. 2-1. For an infinitely repeating lattice with spacing d, impinging waves with wavelength λ will scatter and constructively interfere at various angles of incidence, θ. The order of diffraction, which is the difference of path length between two waves, is given by an integer n.

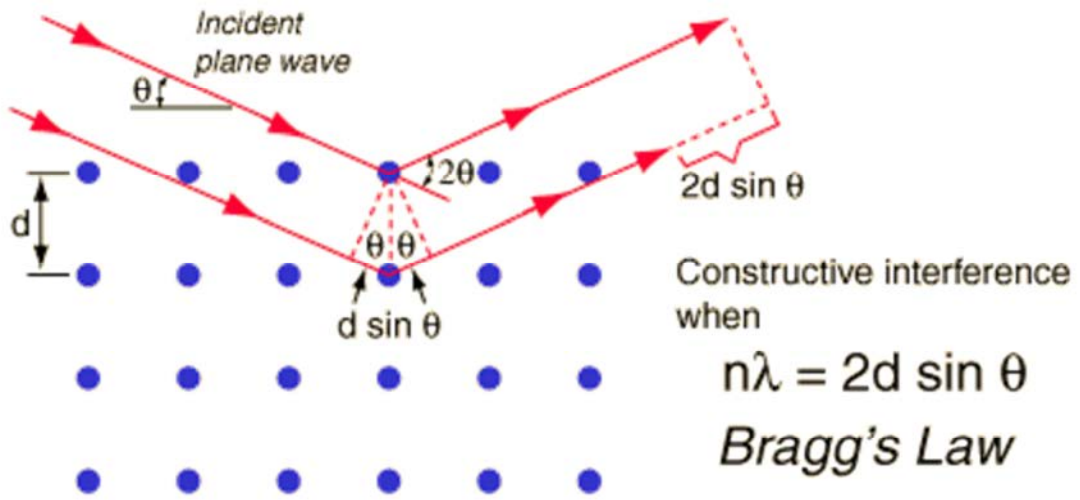

Fig. 2-1 Diagram of determining Bragg's law

It is also possible to estimate the crystallite size of sample from XRD pattern by applying Scherrer's equation:

$$\tau = \frac{K\lambda}{\beta cos\theta} \tag{2-1}$$

where, τ is crystallite size, K is shape factor with the typical value of 0.9, λ is X-ray wavelength, β is full width at half maximum (FWHM) in radians, and θ is angle of incident beam. However, it is necessary to make a correction to the FWHM data obtained from XRD due to the instrument's broadening peak width.

In this experiment, the XRD spectra at room temperature was obtained by using a Scintag Powder XRD instrument with Cu-Kα radiation with a wavelength of 1.5418 Å, scanning range from 10° to 40° at 40 kV/30 mA with scan step of 0.02°. Jade 6 software was used to fit XRD patterns and calculate crystallite sizes for both $ZrW_2O_7(OH)_2 \cdot 2H_2O$ and ZrW_2O_8 based on Scherrer's equation, with the FWHM values obtained from the diffraction peaks. Silicon

standard data was employed to correct the error from the broadening peaks caused by the instrument.

2.3.2 Isothermal X-ray diffraction

Isothermal XRD measurement is a special XRD technique that can facilitate the characterization of XRD patterns at various temperatures, which provides information about the changes in structure of the sample depending on changes in temperature. In this research, the isothermal XRD was employed to characterize the changes in lattice parameter of unit cells in ZrW_2O_8 for calculation of CTE values. The measurement was carried out on a PAnalytical instrument together with a temperature controllable hot stage. The procedure for measurement is: first, the samples were heated to 600 °C at a rate of 20 °C/min to evaporate any water residue in the samples and eliminate the effects of adsorbed moisture observed in previous work[42]; then, a cycle of cooling and heating was performed between room temperature and 600 °C in 10 °C temperature steps from 20 to 200 °C, and in 50 °C steps from 200 °C to 600 °C, with heating and cooling rates of 5 °C/min between each measurement temperature. The diffraction data was collected in scan steps of 0.02° from 10° to 90° for 100 second exposure times at each testing temperature. The lattice parameters at different temperatures were obtained by performing Rietveld refinement of each XRD pattern with a General Structure Analysis System (GSAS). In each refinement, a pseudo-Voigt profile of type 2 was employed for fitting the peak profile and 28 histogram variables were refined, including background terms, scaling factors, cell parameters, profile parameters, as well as atomic displacement parameters. The final results for all the refined data were obtained from different temperatures shown as: χ^2 from 2.1 to 5.2 and R-factors (R_{wp}) from 4.0 % to 6.7 %.

2.3.3 Scanning electron microscopy (SEM)

Scanning electron microscopy is an important technique providing information about a sample's surface topography and composition by scanning the sample with a high energy beam of electrons that interacts with the atoms within the sample. Due to the small wavelength of electron beam on the surface, SEM facilitates a high resolution image of the morphologies of a sample.

In this experiment, the nanoparticle morphologies and size scales were characterized by FEI Quanta 250 field emission SEM at 10.00 kV under a high vacuum measurement condition. To prepare the sample, the ZrW_2O_8 nanoparticles were sealed in 20 ml vials containing an acetone solution and placed in the ultrasonic bath for sonication to get fully dispersed; then two drops of the mixture were placed onto a piece of glass on a carbon black grid. After the solution evaporated and only left nanoparticles on the slide, samples were sputtered a coating layer of iridium with thickness of 2 nm on the surface to inhibit "charging" for non-conductive samples under high energy electron beams in SEM. Nanoparticle sizes were measured by the Quartz PCI viewer V5.1 software.

2.3.4 Thermogravimetric analysis (TGA)

Thermogravimetric analysis (TGA) is a type of thermal analysis measurement used to detect changes in the weight of a material as a function of temperature or time, under a controlled atmosphere. Measurements are used primarily to determine the composition of materials and to predict their thermal stability at temperatures up to 1000°C. The technique can be used to characterize materials that exhibit a weight loss or gain due to decomposition, oxidation, or dehydration under a continuous heating environment. In this research, TA Instruments Q50 TGA was used to study the dehydration process in calcination and hydration phenomena of the

synthesized ZrW_2O_8 nanoparticles by determining the weight loss of their water contents. The procedure of determining dehydration is to weigh approximately 10 mg of a sample in an alumina pan and then heat that sample under Nitrogen gas to 600 °C at rate of 20 °C/min and isothermally for 30 min; For the study of the amount of water hydrates gain during hydration process, 10 mg samples were heated under nitrogen gas to 190 °C at a rate of 20 °C/min and held for 10 min until no further weight loss was observed.

2.3.5 Brunauer-Emmett-Teller (BET) surface area analyzer

A Brunauer-Emmett-Teller (BET) surface area analyzer is a principal technique for the analysis of the surface of a sample such as surface area and porosity of a solid[46]. The mechanism of BET analysis is based on the adsorption and desorption of gases such as N_2 onto the sample as a function of relative pressure and can be illustrated in Fig. 2-2. At low pressures, the gas molecules first begin to be adsorbed at isolated random sites on the surface of sample; as the gas pressure increases, the monolayer is formed on the sample and more layers can be built up to form multiple layers if the amount of N_2 is increased further, and finally when all the pores are filled at a very high pressure it is called condensation. This can be measured and used to estimate the pore size, volume and distribution. The BET equation is shown below:

$$\frac{1}{v(p_0/p-1)} = \frac{1}{v_m c} + \frac{c-1}{v_m c}\left(\frac{p}{p_0}\right) \tag{2-2}$$

where, p and p_0 are the equilibrium and saturation pressure of adsorption, v is the volume of gas adsorption, v_m is the volume of gas adsorbed by monolayer, c is BET constant, expressed as:

$$c = exp\left(\frac{E_1 - E_L}{RT}\right) \tag{2-3}$$

where, E_1 and E_L are the heat of adsorption for first layer and higher layers. The total surface area is described as the external surface area plus the micro-pores area and can be calculated by the following Equation 2-4:

$$S_{BET,Total} = \frac{(v_m N s)}{V} \tag{2-4}$$

where, v_m is the molar volume of adsorbed gas for monolayer, N is Avogadro's number, s is adsorption cross section, V is molar volume of adsorbed gas.

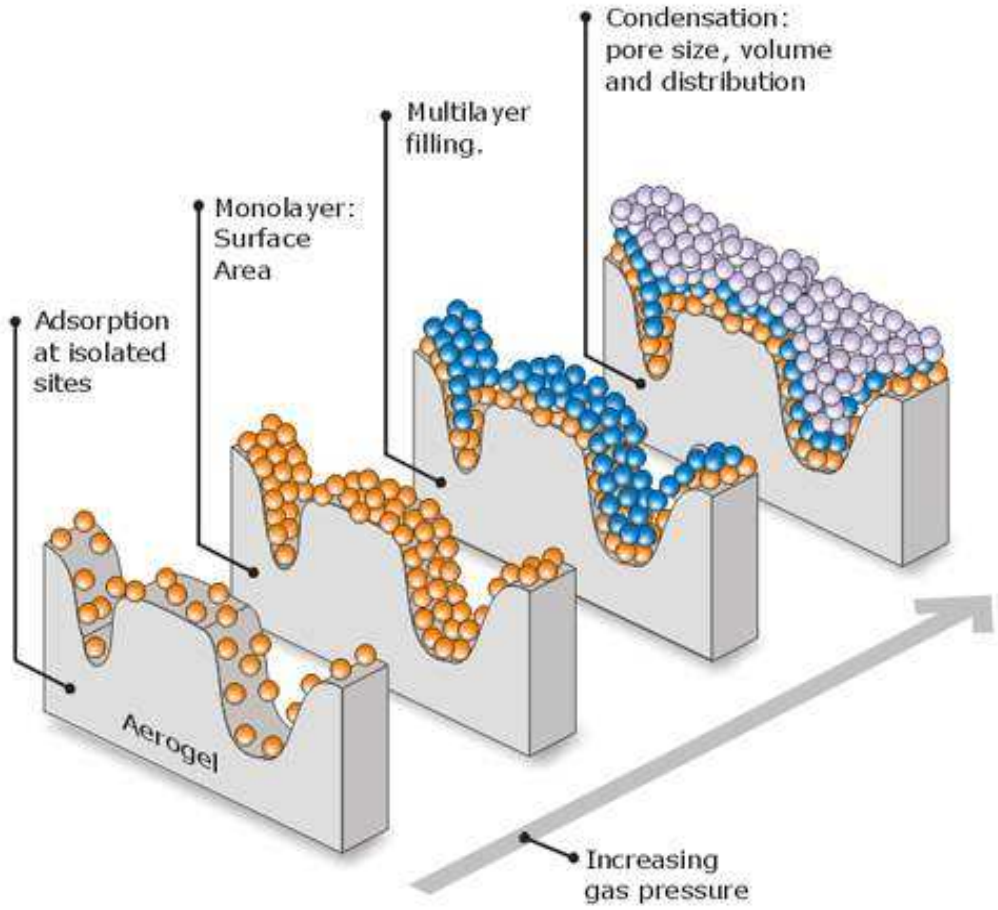

Fig. 2-2 Scheme of pore filling during the BET analysis

A porous material is a solid with a pore matrix in its continuous structure, such as Zeolite. However, some other solids can also create pores without these pore structures. For instance, nanoparticles tend to join together under a strong electrostatic force on the surface to form agglomerates, the voids created by the aggregation of the nanoparticles constitute a pore system on the sample. Pore can be classified into three types according to the width of pore system in the solids as shown in Table 2-1. For micropore structures, due to the proximity of the walls, the interaction potential is much higher than in wider pores structures. In mesopores, capillary condensation plays an important role. In macropore structures, pore ranges are very wide.

Table 2-1 Classification of pores according to width

Pore type	**Width**
Mircopores	d < 2 nm
Mesopores	2 nm < d < 50 nm
Macropores	d > 50 nm

Adsorption and desorption of isotherms are very important for BET surface area and porosity analysis. They describe the amount of gas adsorbed and desorbed over a wide range of relative pressures at a fixed temperature and can be used to characterize the surface porosity. There are five typical isotherm types proposed by Brunauer, Demingand Tell as shown in Fig. 2-3. In a type I isotherm, adsorption takes place in the solid's micropores and no further adsorption is continued. A type II isotherm is often observed in the adsorption of gases into a non-porous solid with pore diameters larger than 2nm. A type III isotherm is regularly observed in nonporous or macropore structures, and adsorption proceeds as the adsorbate interaction with an adsorbed layer is greater than the interaction with the adsorbent surface. Also, type III isotherms show a weak interaction between a gas and solid which causes a small uptake at low pressures. The adsorbate-adsorbate force promotes the adsorption of further molecules once one molecule

is adsorbed. A type IV isotherm with a characteristic hysteresis loops occurs in pores ranging of 1.5 – 100 nm. A type V isotherm takes place in a mesoporous or microporous solid with weak interaction forces between adsorbent-adsorbate, which is similar to a type-III isotherm.

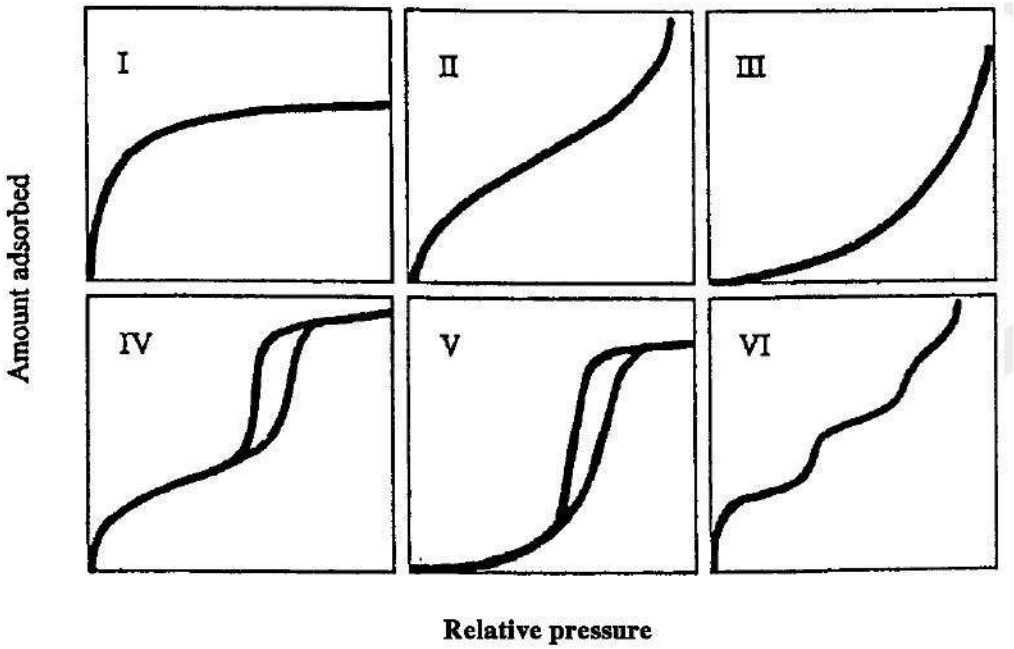

Fig. 2-3 Different types of adsorption and desorption isotherm

In this experiment, Micromeritics ASAP 2020 Surface Area and Porosity Analyzer was used to examine the surface area and pore structures of the synthesized ZrW_2O_8 nanoparticles. The procedure for the characterization is: first the same is put into a tube and degased under a high temperature (~300 °C) to eliminate the existing adsorbed matters such as water; then the tube is connected to the analysis station and cools down evacuating the system. After certain amount of nitrogen (N_2) is introduced to keep the system in equilibrium, the pressure is measured. Then another amount of nitrogen is added and pressure is measured again. As long as the pressure does not change it means that the nitrogen is adsorbed on the surface of the sample. If

the pressure increases it means that surface is covered completely with nitrogen. When atmospheric pressure is reached, the procedure is repeated in reverse with nitrogen leaving the sample and the pressure is again measured after equilibrium. The measurements are completed when system has returned to its initial vacuum pressure.

Chapter 3 Study on controlling morphologies and crystallite sizes of $ZrW_2O_7(OH)_2 \cdot 2H_2O$ nanoparticles

In this research, experimental conditions were varied for the synthesis of ZrW_2O_8 nanoparticles with different morphologies and crystallite sizes using the hydrothermal reaction technique. This included different initial reactants such as a ZrAc solution, $ZrO(NO_3) \cdot xH_2O$, and $ZrO(ClO_4)_2 \cdot xH_2O$ for zirconium compounds; $Na_2WO_4 \cdot 2H_2O$, $(NH_4)_6H_2W_{12}O_{40} \cdot xH_2O$, $Na_6W_{12}O_{39} \cdot xH_2O$ for tungsten sources, various acidic mediums (5 M, 7 M of HCl or 3 M, 5 M of $HClO_4$), and reaction time was varied (12 h and 24 h) as well as temperature (130 °C and 160 °C).

3.1 X-ray diffraction results of nano-scaled ZrW_2O_8 and $ZrW_2O_7(OH)_2 \cdot 2H_2O$

The crystal structures of both $ZrW_2O_7(OH)_2 \cdot 2H_2O$ and ZrW_2O_8 were identified using the X-ray diffraction technique. Tetragonal $ZrW_2O_7(OH)_2 \cdot 2H_2O$ and cubic ZrW_2O_8 nanoparticles could be obtained without containing any impurities, such as WO_3, under all hydrothermal routes tested in this work, as confirmed by the x-ray diffraction patterns shown in Fig. 3-1.

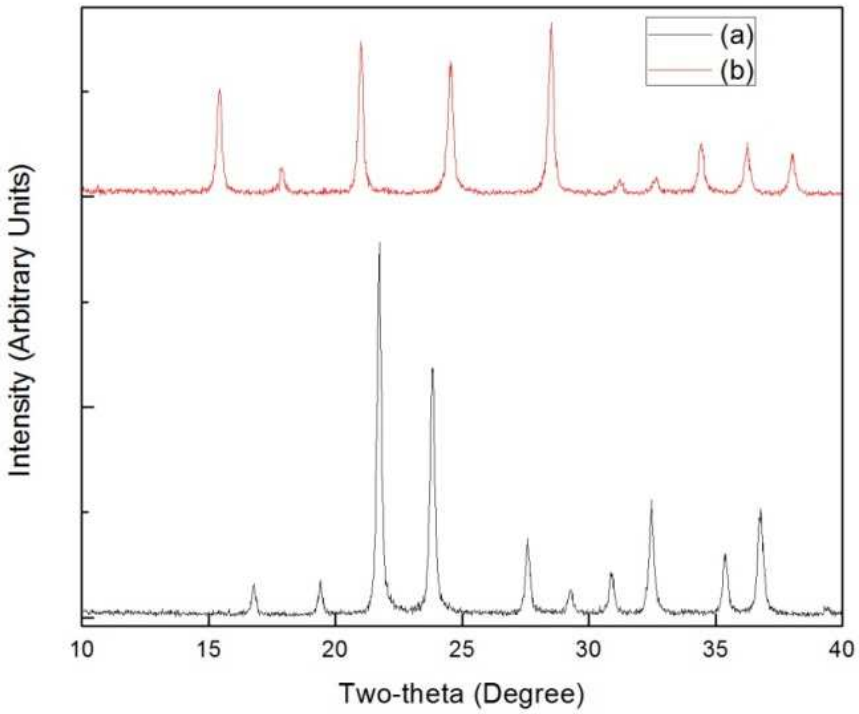

Fig. 3-1 XRD pattern of (a) ZrW_2O_8 and (b) $ZrW_2O_7(OH)_2 \cdot 2H_2O$

However, differences in experimental conditions led to diffraction patterns with different Bragg's peak intensities and different widths due to variations in crystallite sizes of the nanoparticles. The detailed data of crystallite sizes for each experimental batch is shown in Table 3-1. It was found that the crystallite sizes of $ZrW_2O_7(OH)_2 \cdot 2H_2O$ ranged from 20 to 66 nm, depending on experimental parameters. The smallest crystallite size was observed from the system of $ZrO(ClO_4)_2/Na_2WO_4$ and $ZrO(NO_3)_2/Na_2WO_4$ under 5 M $HClO_4$ acidic solution, which were 17 nm and 20 nm, respectively. The largest crystallite size was found in the synthesis condition at 160 °C. The experimental condition played an important role in the nucleation and growth of ZrW_2O_8 nanoparticles. Under most circumstances, the crystallite size is not always identical to the particles size due to the agglomeration of nanoparticles or multiple crystals

joining together to form larger particles, thus to have a better understanding of changing in shapes and sizes of nanoparticles, it is practical to use SEM technology to study the effects of experimental variables on morphologies.

3.2 Effects of experimental parameters on morphologies of $ZrW_2O_7(OH)_2 \cdot 2H_2O$ nanoparticles

3.2.1 Effect of initial reactants

Since the morphologies of the precursor $ZrW_2O_7(OH)_2 \cdot 2H_2O$ resemble ZrW_2O_8 nanoparticles after heat treatment for crystal structure transformation, in this experiment it is possible to characterize the particles of $ZrW_2O_7(OH)_2 \cdot 2H_2O$ for comparison. Various initial zirconium and tungstate reactants were employed in different combinations to study the effect these variations had on the morphologies of synthesized ZrW_2O_8 nanoparticles.

First, $Na_2WO_4 \cdot 2H_2O$ was chosen as the tungsten source to react with three types of zirconium raw materials in the same HCl acidic medium. The morphologies of three kinds of $ZrW_2O_7(OH)_2 \cdot 2H_2O$ nanoparticles are shown in Fig. 3-2. It was observed that different initial zirconium compounds reacting with Na_2WO_4 yielded nanoparticles with distinct morphologies. As seen in Fig. 3-2(a) and (d), $ZrW_2O_7(OH)_2 \cdot 2H_2O$ nanoparticles with crystalline sizes of 30 nm exhibit small capsule-like rods with lengths between 200–500 nm and widths of 50–80 nm obtained when ZrAc solution reacted with $Na_2WO_4 \cdot 2H_2O$. Upon using $ZrO(ClO_4)_2 \cdot xH_2O$, the $ZrW_2O_7(OH)_2 \cdot 2H_2O$ particles with crystallite sizes of 45 nm were bundle-like rods fused at one end with lengths ranging from 500 to 900 nm and widths between 30 to 80 nm, as shown in Fig. 3-2(b) and (e). Large and long rectangular rods with particles sizes of 0.8–1.5 μm in length and

70–180 nm in width were obtained when $ZrO(NO_3)\cdot xH_2O$ was chosen for the reaction, as shown in Fig. 3-2(c) and (f).

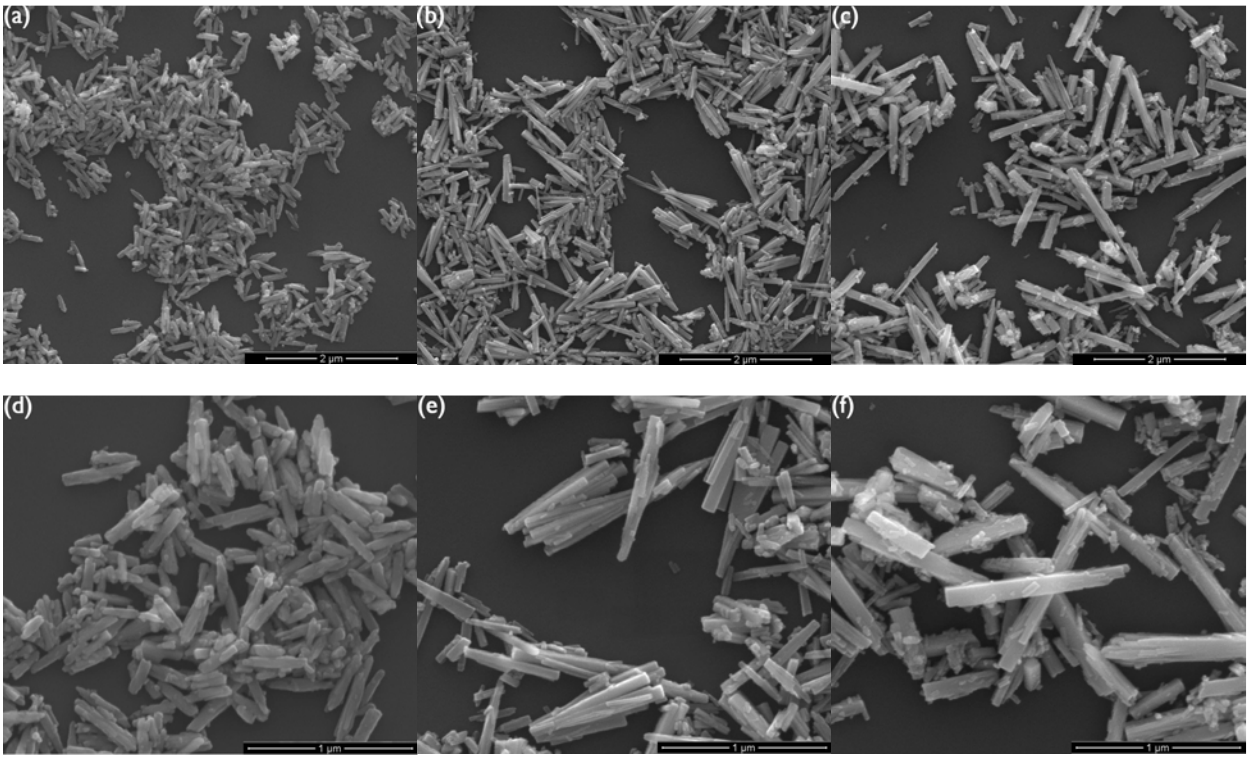

Fig. 3-2 SEM images of $ZrW_2O_7(OH)_2\cdot 2H_2O$ synthesized under the following conditions: 7 M HCl at 130 °C for 12 h with $Na_2WO_4\cdot 2H_2O$ and zirconium raw materials of ZrAc in (a) 20000X and (d) 50000X, $ZrO(ClO_4)_2\cdot xH_2O$ at (b) 20000X and (d) 50000X, and $ZrO(NO_3)\cdot xH_2O$ at (c) 20000X and (f) 50000X)

Then, $ZrW_2O_7(OH)_2\cdot 2H_2O$ nanoparticles were synthesized using the same reactants under a $HClO_4$ acidic medium with all other conditions fixed. As shown in Fig. 3-3 (a) and (d), rectangular nanorods (ca. 350-800 nm by 40-90 nm) were individually displayed and obtained by a ZrAc and $Na_2WO_4\cdot 2H_2O$ in 3 M $HClO_4$ reaction medium. However, the morphologies of $ZrW_2O_7(OH)_2\cdot 2H_2O$ nanoparticles synthesized when $ZrO(ClO_4)_2\cdot xH_2O$ and $ZrO(NO_3)\cdot xH_2O$ were selected for reaction, appeared quite differently compared with the previous combination. Both were nanorods that appeared very thin in width and exhibited an extent of agglomeration to

perform large particles. The crystalline sizes for these two types of nanoparticles were also relatively small, which were 17 nm and 20 nm, respectively. Also, the $ZrW_2O_7(OH)_2 \cdot 2H_2O$ nanoparticles showed distinctively in morphologies obtained from HCl and $HClO_4$ mediums by comparing Fig. 3-2 and Fig. 3-3, the additives of acids exert significant effects on controlling crystallization and growth of nanoparticles, the more systematic experiments on acids types and concentration were carried on and reported in 3.2.2 and 3.2.3.

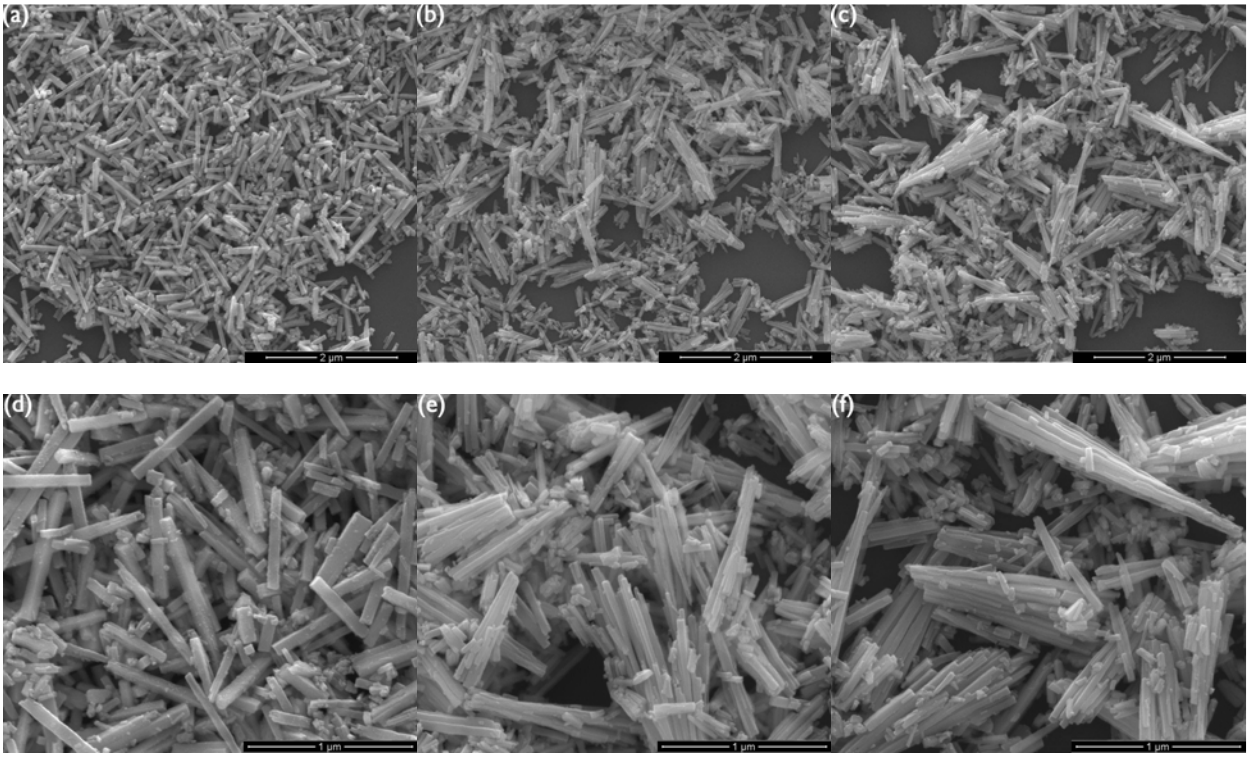

Fig. 3-3 SEM images of $ZrW_2O_7(OH)_2 \cdot 2H_2O$ synthesized under the following conditions: 3 M $HClO_4$ at 130 °C for 12 h with $Na_2WO_4 \cdot 2H_2O$ and zirconium raw materials of ZrAc in (a) 20000X and (d) 50000X, $ZrO(ClO_4)_2 \cdot xH_2O$ at (b) 20000X and (e) 50000X, and $ZrO(NO_3) \cdot xH_2O$ at (c) 20000X and (f) 50000X

Then, to compare the initial compounds effect on $ZrW_2O_7(OH)_2 \cdot 2H_2O$ nanoparticles on tungsten, $Na_2WO_4 \cdot 2H_2O$, $(NH_4)_6H_2W_{12}O_{40} \cdot xH_2O$ and $Na_6W_{12}O_{39} \cdot xH_2O$ were selected to react with identical zirconium compounds. First, the ZrAc solution reacted with $Na_2WO_4 \cdot 2H_2O$ and

$(NH_4)_6H_2W_{12}O_{40}\cdot xH_2O$ respectively, and the produced nanoparticles morphologies are displayed in Fig. 3-4. From observation, the $ZrW_2O_7(OH)_2\cdot 2H_2O$ appear as short rods with two sharp ends when the ZrAc and $Na_2WO_4\cdot 2H_2O$ mixture reacted in 7 M HCl for 24 h at 130 °C, as seen in Fig. 3-4(a) and (c). Observed from Fig. 3-4 (b) and (d) rectangular nanorods with inhomogeneous sizes can be yielded by using ZrAc and $(NH_4)_6H_2W_{12}O_{40}\cdot xH_2O$ under the same experimental conditions.

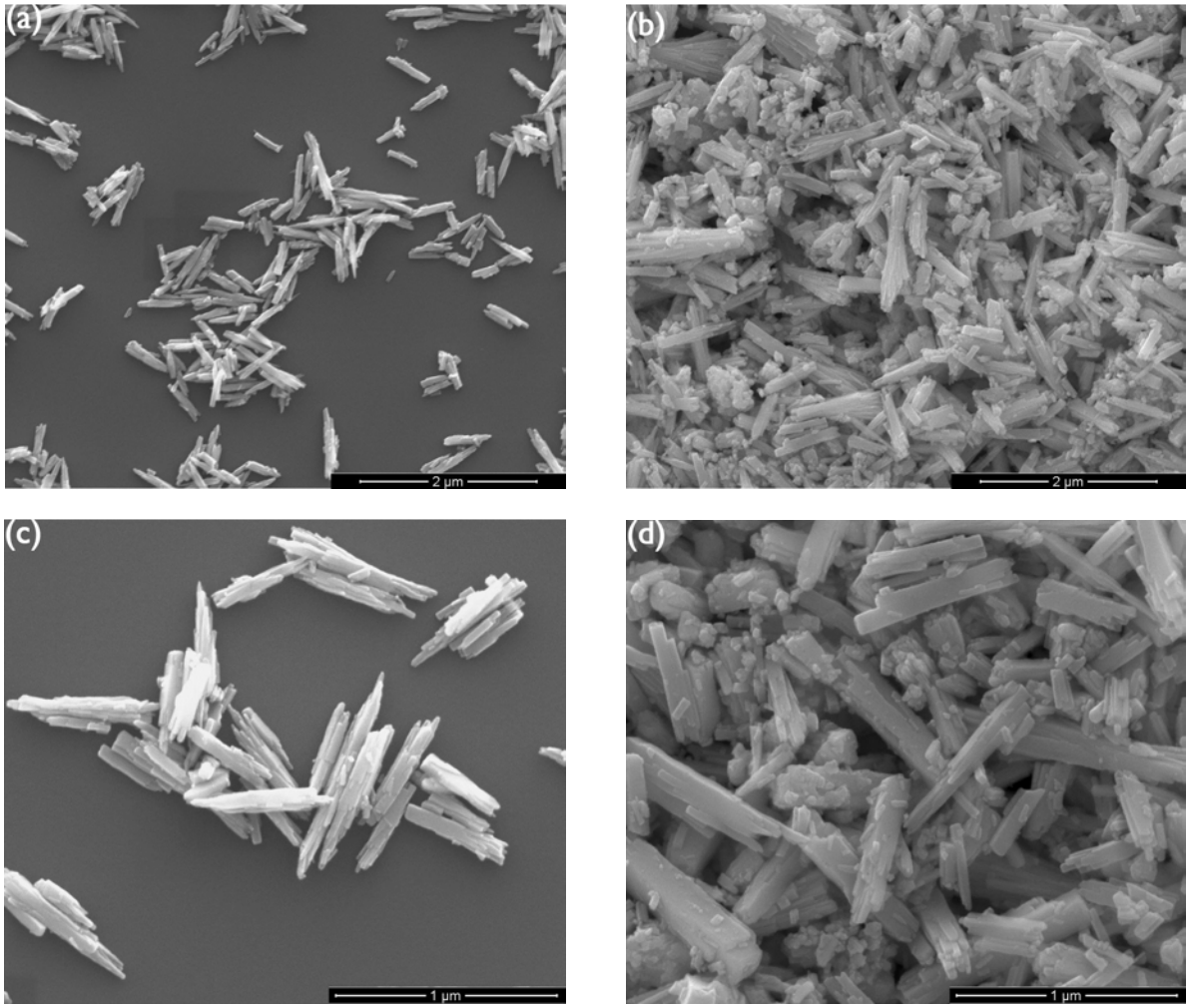

Fig. 3-4 SEM images of $ZrW_2O_7(OH)_2\cdot 2H_2O$ synthesized under the following conditions: 7 M HCl at 130 °C for 24 h with ZrAc and tungstate raw materials of $Na_2WO_4\cdot 2H_2O$ at (a) 20000X and (c) 50000X, and $(NH_4)_6H_2W_{12}O_{40}\cdot xH_2O$ at (b) 20000X and (d) 50000X

In the following experiments, $ZrO(ClO_4)_2 \cdot xH_2O$ was used as a zirconium source to react with different tungstate materials under the same reaction conditions. It is found in Fig. 3-5(a) and (d) that the synthesized $ZrW_2O_7(OH)_2 \cdot 2H_2O$ nanoparticles appear as bundle-like shape with uniform sizes ca. 500-800 nm in length by ca. 40-80 nm in width when $Na_2WO_4 \cdot 2H_2O$ was involved in the reaction. However, particles with wide size distributions on both the micron and nano-scales were found from the combination of $ZrO(ClO_4)_2 \cdot xH_2O$ and $(NH_4)_6H_2W_{12}O_{40} \cdot xH_2O$. The $ZrW_2O_7(OH)_2 \cdot 2H_2O$ also displayed inhomogeneous size-scales and ill-defined shapes when synthesized by choosing $Na_6W_{12}O_{39} \cdot xH_2O$ as the tungstate raw reactant in Fig. 3-5(c) and (f).

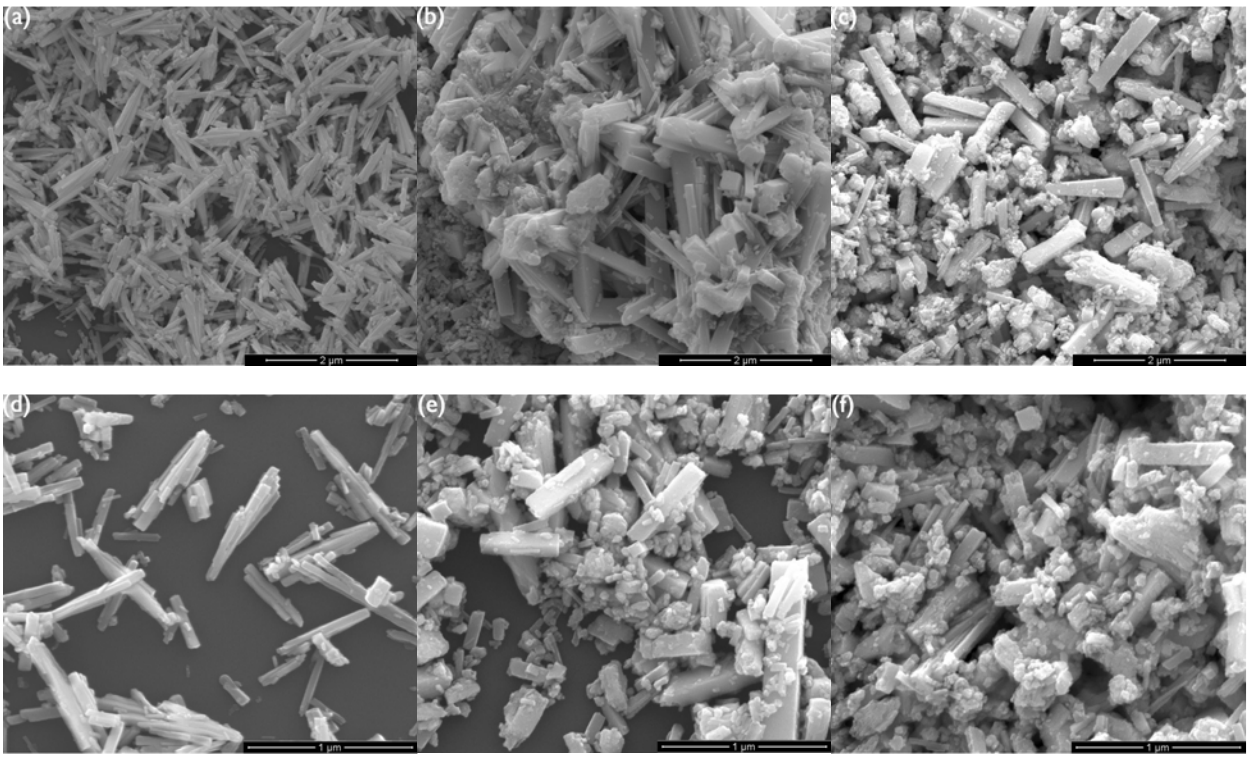

Fig. 3-5 SEM images of $ZrW_2O_7(OH)_2 \cdot 2H_2O$ synthesized under the following conditions: 7 M HCl at 130 °C for 24 h with $ZrO(ClO_4)_2 \cdot xH_2O$ and tungstate raw materials of $Na_2WO_4 \cdot 2H_2O$ at (a) 20000X and (d) 50000X, $(NH_4)_6H_2W_{12}O_{40} \cdot xH_2O$ at (b) 20000X and (e) 50000X, and $Na_6W_{12}O_{39} \cdot xH_2O$ at (c) 20000X and (f) 50000X

Finally, $ZrO(NO_3)_2 \cdot xH_2O$ was reacted with $Na_2WO_4 \cdot 2H_2O$ and $(NH_4)_6H_2W_{12}O_{40} \cdot xH_2O$ under same reaction conditions, respectively, for comparison. As seen in Fig. 3-6, $ZrW_2O_7(OH)_2 \cdot 2H_2O$ appeared as individual rectangular rods with length of ca. 0.5 to 1.2 µm and width of 70 to 160 nm when $Na_2WO_4 \cdot 2H_2O$ was tested. On the other hand, particles synthesized by $Na_6W_{12}O_{39} \cdot xH_2O$ also appeared to lack in uniformity of shape or sizes. Some particles showed long thin rods length up to ca. 2 µm but others as appeared as ill-defined shapes only 300 to 500 nm.

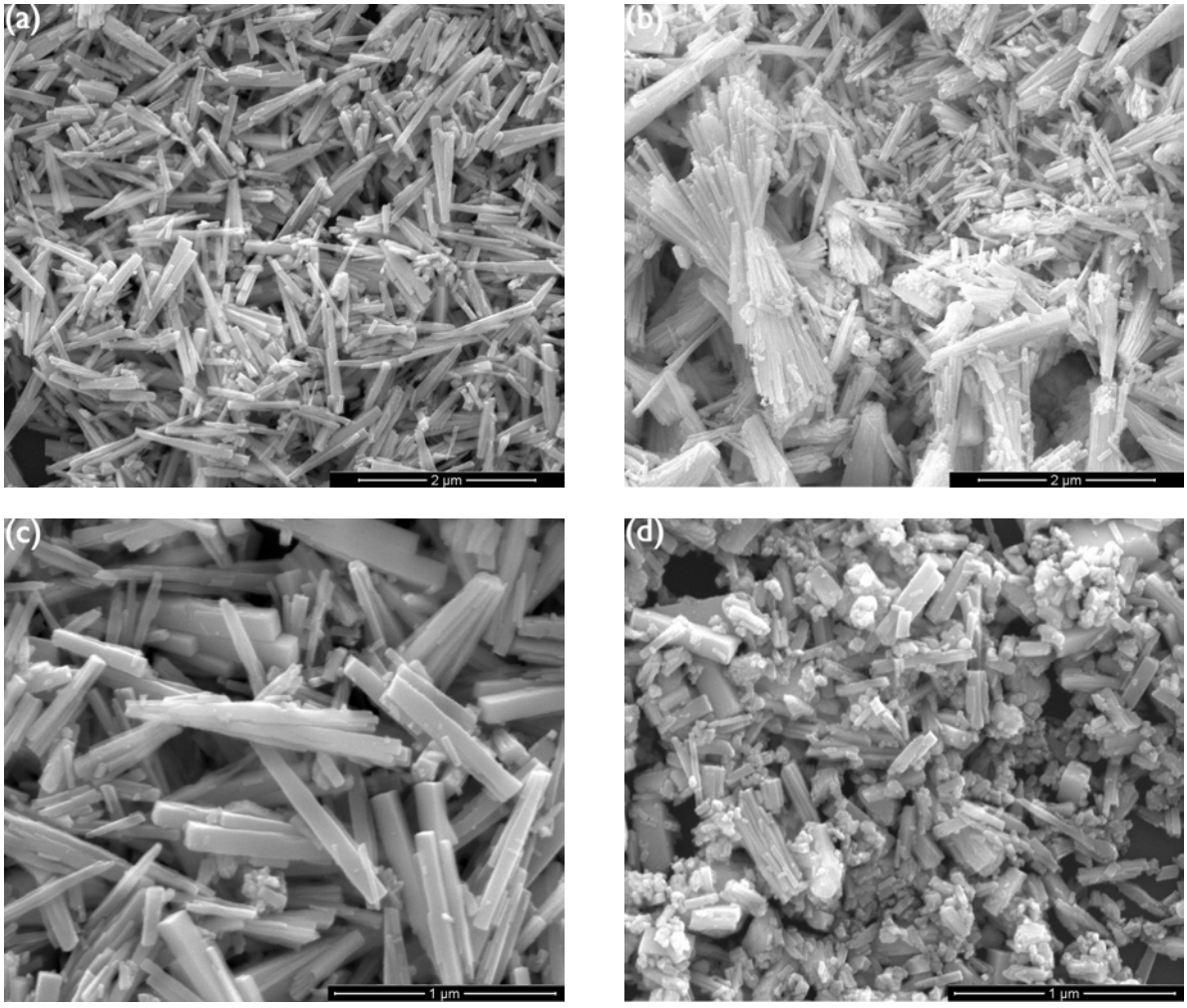

Fig. 3-6 SEM images of $ZrW_2O_7(OH)_2 \cdot 2H_2O$ synthesized under the following conditions: 7 M HCl at 130 °C for 24 h with $ZrO(NO_3)_2 \cdot xH_2O$ and tungstate raw materials of $Na_2WO_4 \cdot 2H_2O$ at (a) 20000X and (c) 50000X, and $(NH_4)_6H_2W_{12}O_{40} \cdot xH_2O$ at (b) 20000X and (d) 50000X

Based on the aforementioned study of how the initial raw materials effected the morphologies and crystallite sizes of $ZrW_2O_7(OH)_2 \cdot 2H_2O$, different morphologies and size-scales can be determined using various starting materials. Three types of zirconium compounds when reacted with $Na_2WO_4 \cdot 2H_2O$ yielded nanoparticles with homogeneous and distinctive shapes and sizes. However, the other two tungstate compounds, $(NH_4)_6H_2W_{12}O_{40} \cdot xH_2O$ and $Na_6W_{12}O_{39} \cdot xH_2O$, were not successful in the synthesis of $ZrW_2O_7(OH)_2 \cdot 2H_2O$ nanoparticles due to non-uniform morphologies and wide size distribution. Thus, further research on controlling the morphologies of nanoparticles was based on the ZrAc, $ZrO(ClO_4)_2 \cdot xH_2O$ and $ZrO(NO_3)_2 \cdot xH_2O$ reaction with $Na_2WO_4 \cdot 2H_2O$.

3.2.2 Effect of acid types

Since the hydrothermal synthesis of $ZrW_2O_7(OH)_2 \cdot 2H_2O$ nanoparticles can only be achieved in an acidic medium, it is important to investigate the effect of acid type and concentration on crystallite size and morphology of the nanoparticles. As reported in prior work, it was found that nanoparticles with different crystallite sizes and morphologies can be obtained by altering the acids used in the reaction[30]. The following studies focus on how the types of acidic mediums influence the formation of $ZrW_2O_7(OH)_2 \cdot 2H_2O$ nanoparticles in a hydrothermal condition.

First, a ZrAc solution and $Na_2WO_4 \cdot 2H_2O$ reacted in 5 M HCl and 5 M $HClO_4$ solution produced $ZrW_2O_7(OH)_2 \cdot 2H_2O$ nanoparticles which appear to have nearly the same morphologies of rectangular nanorods with size-scales of 0.3-1 μm by 50-100 nm, shown in Fig. 3-7. The crystallite sizes of both nanoparticles were close, 29 and 34 nm respectivly. Therefore, it can be concluded that different acid types had little effect on the morphologies of $ZrW_2O_7(OH)_2 \cdot 2H_2O$.

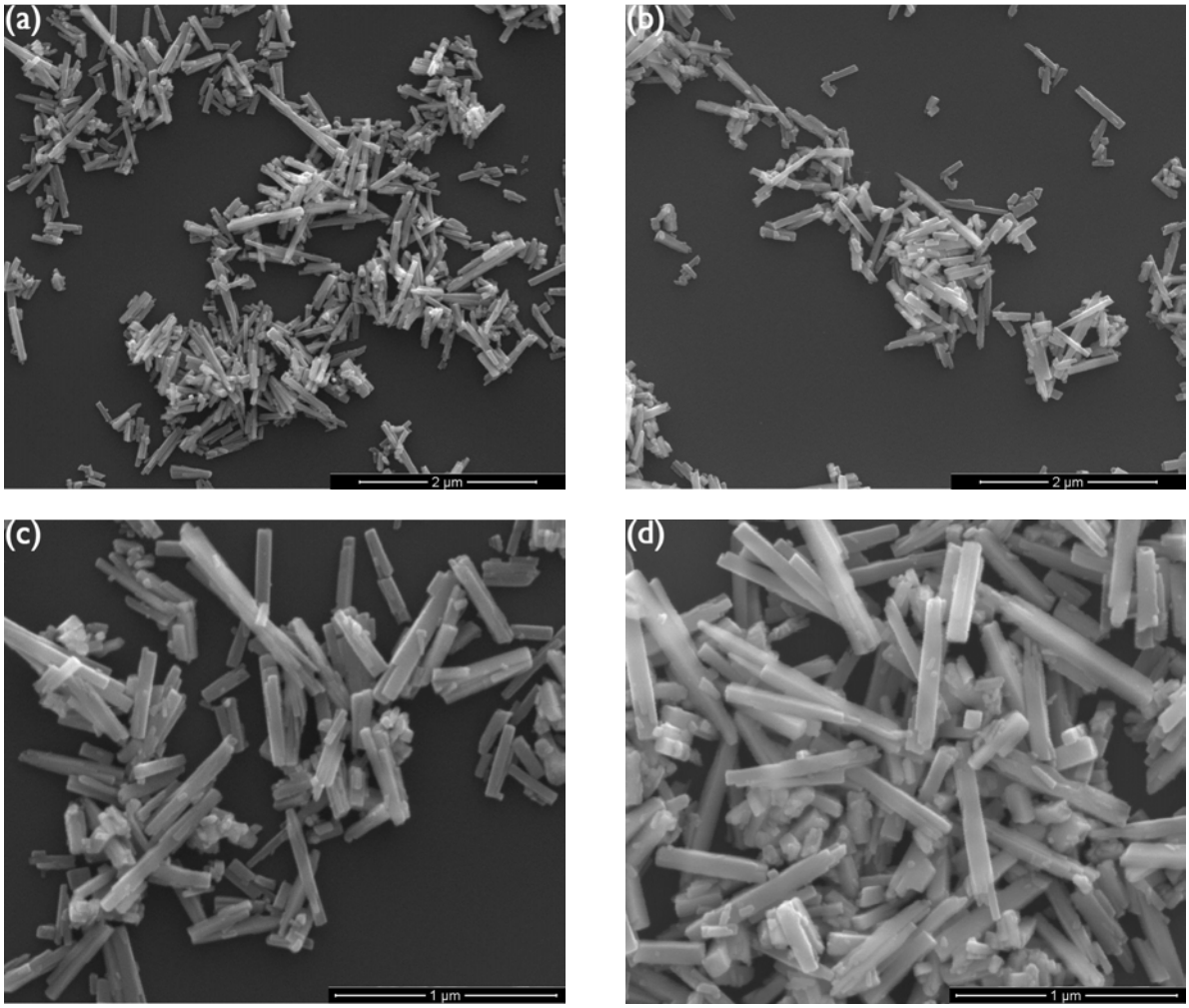

Fig. 3-7 SEM images of $ZrW_2O_7(OH)_2 \cdot 2H_2O$ synthesized under the following conditions: ZrAc and $Na_2WO_4 \cdot 2H_2O$ mixture at 130 °C for 24 h in 5 M HCl at (a) 20000X and (c) 50000X, and 5 M $HClO_4$ at (b) 20000X and (d) 50000X

In case of $ZrO(ClO_4)_2 \cdot xH_2O$, HCl and $HClO_4$ acids of the same molarity were also tried and an obvious change in morphologies of the nanoparticles was observed, shown in Fig. 3-8. When the reaction was carried out in 5 M HCl, the particles showed as bundle-like shapes with 300-800 nm by 40-70 nm, whose crystallite size was 46 nm. However, the synthesized $ZrW_2O_7(OH)_2 \cdot 2H_2O$ turned into larger peanut-like particles with a width of 90-150 nm that agglomerated with several thin nanoparticles with width of 10-40 nm. Interestingly, the

crystallite size for the latter one was 17 nm, which indicated that crystallite size represents the width of individual particles.

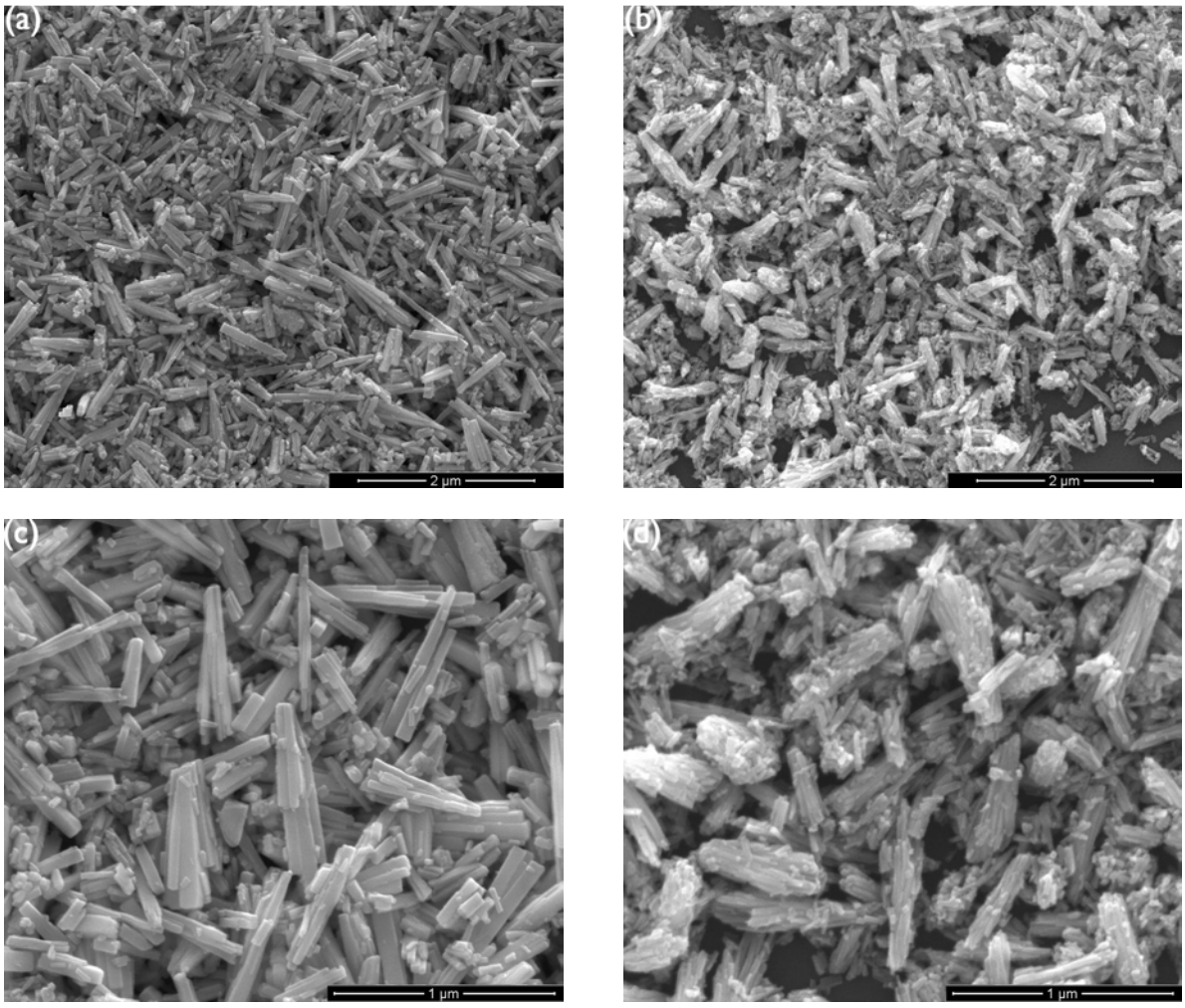

Fig. 3-8 SEM images of $ZrW_2O_7(OH)_2 \cdot 2H_2O$ synthesized under the following conditions: $ZrO(ClO_4)_2 \cdot xH_2O$ and $Na_2WO_4 \cdot 2H_2O$ mixture at 130 °C for 24 h in 5 M HCl at (a) 20000X and (c) 50000X, and 5 M $HClO_4$ at (b) 20000X and (d) 50000X

The same observation was also noticed from using $ZrO(NO_3)_2 \cdot xH_2O$ as the zirconium starting materials and reacted with 5 M of HCl and $HClO_4$ acids shown in Fig. 3-9. The nanoparticles synthesized under HCl were individually present, but the severity of the agglomeration of the nanoparticles made each particle's edges difficult to identify.

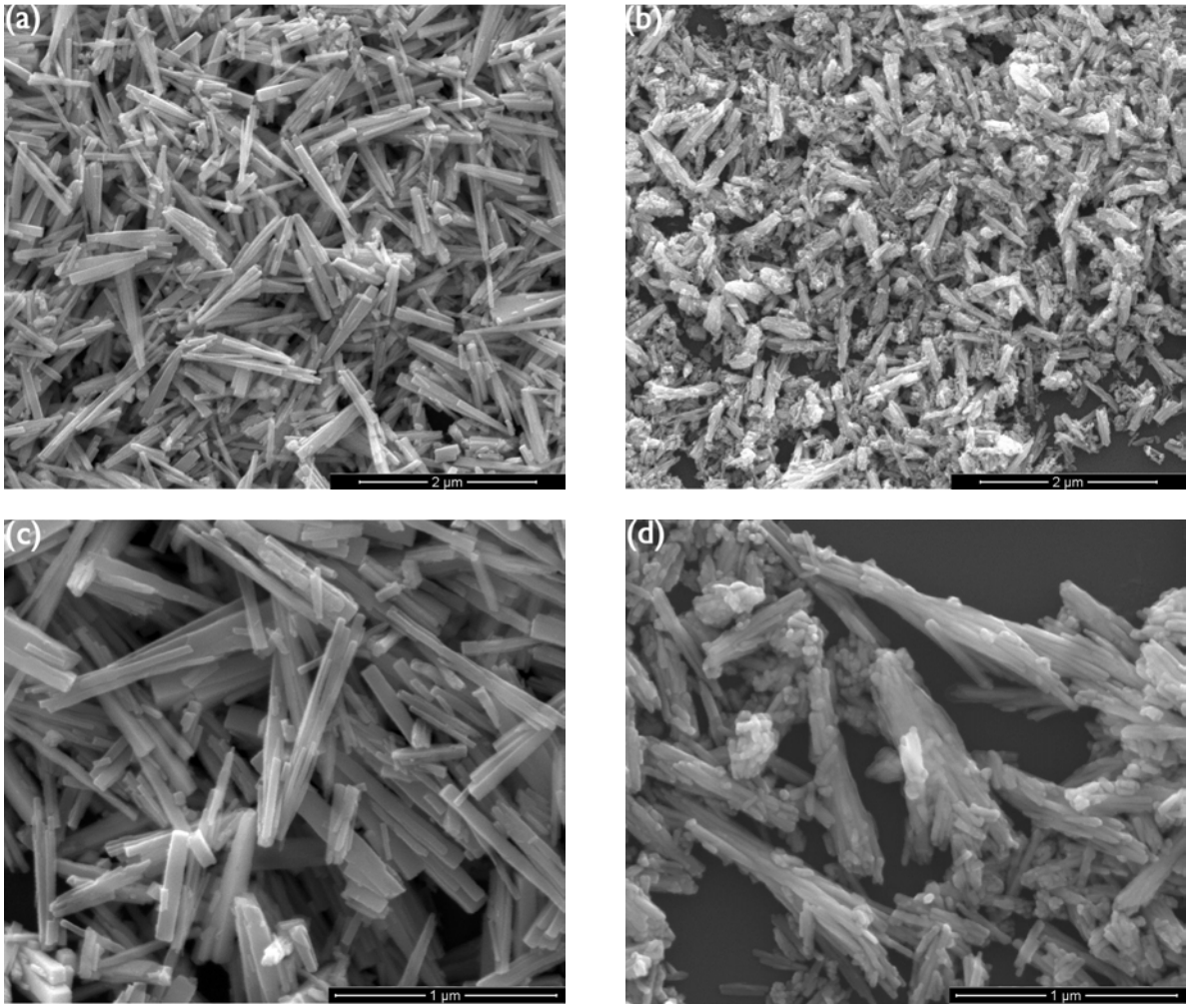

Fig. 3-9 SEM images of $ZrW_2O_7(OH)_2 \cdot 2H_2O$ synthesized under the following conditions: $ZrO(NO_3)_2 \cdot xH_2O$ and $Na_2WO_4 \cdot 2H_2O$ mixture at 130 °C for 24 h in 5 M HCl at (a) 20000X and (c) 50000X, and 5 M $HClO_4$ at (b) 20000X and (d) 50000X

The reason for this phenomenon can be explained from the mechanism of crystallization and growth for $ZrW_2O_7(OH)_2 \cdot 2H_2O$ in a hydrothermal reaction. There are two factors that influence the nanoparticles morphology and crystallite size. One is the crystallization mechanism of $ZrW_2O_7(OH)_2 \cdot 2H_2O$ nanoparticles in an acidic medium, as referenced by the previous report that a higher concentration of counter ions with the presence of chloride ions significantly improves crystallization kinetics of nanoparticles in an acidic solution[29]. The other is the

interaction between the nanoparticles induced by the strong electrostatic attraction force on the high energy surface of nanoparticles. In this experiment, the formation and growth of $ZrW_2O_7(OH)_2 \cdot 2H_2O$ nanoparticles became faster to overcome the particles' interaction, this means that individual rods can be synthesized in a HCl acidic medium. However, fewer free Cl^{-1} ions existed in $HClO_4$ solution and the addition of NaCl failed to provide sufficient quantities of Cl^{-1} due to lower solubility in such high a concentration mixture. So the nanoparticles crystallization proceeded at a relatively slower rate. Meanwhile, the strong attractive interaction among the nanoparticles restricted the further growth of $ZrW_2O_7(OH)_2 \cdot 2H_2O$. As a result, the combination of these two factors resulted in the agglomeration of thinner nanoparticles and smaller crystallite sizes in the $HClO_4$ acidic medium.

3.2.3 Effect of acid concentration

Besides acid type, the concentration of the reaction medium is also a significant influence on the crystallization and growth of $ZrW_2O_7(OH)_2 \cdot 2H_2O$. The study of the effect of acid concentration on nanoparticles' morphologies was investigated in depth.

In case that HCL added to $ZrW_2O_7(OH)_2 \cdot 2H_2O$ synthesized from the ZrAc and $Na_2WO_4 \cdot 2H_2O$ solution, shows various sizes of nanoparticles depending on the molarity of the acid used in the experiment. It was seen from Fig. 3-10 that the nanoparticles appear similar in size scale (0.3-1 µm by 30-70 nm) when 5 M HCl was involved compared with the ones (300-800 nm by 50-80 nm) obtained from 7 M HCl solution. Also the particles appear as rectangular rods in lower concentration acid mediums, while it was observed that the nanoparticles were characterized as capsule-like shapes at relativly higher concentrated solutions. The phenomenon was opposite the findings by previous researchers[29], who indicated that the high concentration of

counter-ions in an acid enhanced the growth of $ZrW_2O_7(OH)_2 \cdot 2H_2O$ nanoparticles. The reason for this discrepancy needs further investigation.

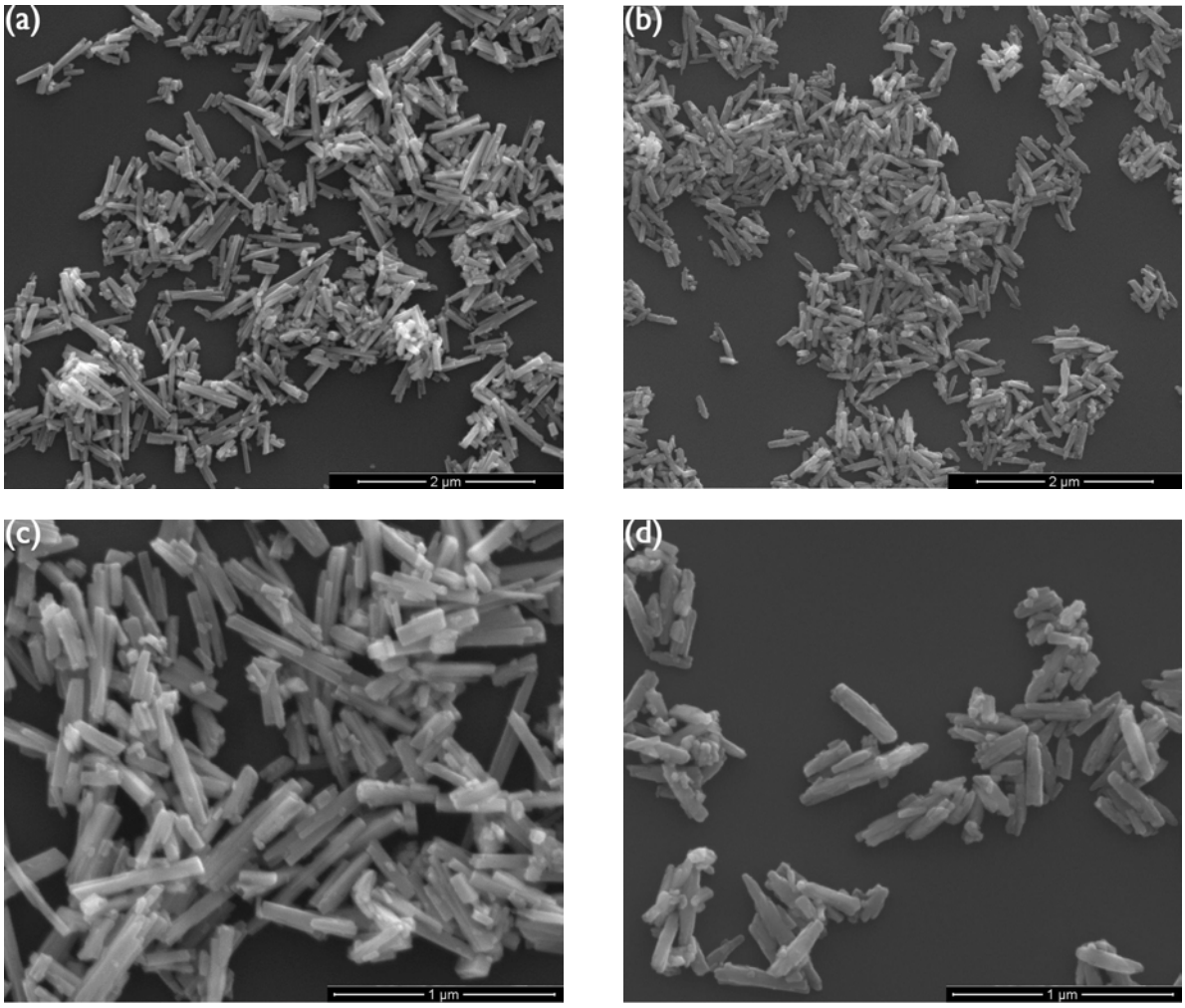

Fig. 3-10 SEM images of $ZrW_2O_7(OH)_2 \cdot 2H_2O$ synthesized under the following conditions: ZrAc and $Na_2WO_4 \cdot 2H_2O$ mixture at 130 °C for 24 h in 5 M HCl at (a) 20000X and (c) 50000X, and 7 M HCl at (b) 20000X and (d) 50000X

Again synthesis was carried in an HCl solution, the bundle-like $ZrW_2O_7(OH)_2 \cdot 2H_2O$ nanoparticles were formed from the $ZrO(ClO_4)_2 \cdot xH_2O$ and $Na_2WO_4 \cdot 2H_2O$ solutions. However, both of the two kinds of nanoparticles yielded from the acidic mediums of different concentrations, looked similar both in particles size (300-800 nm by 40-70 nm) and crystallite

size (46 ± 4 nm). Thus, in this case, the morphologies of $ZrW_2O_7(OH)_2 \cdot 2H_2O$ had a weak correlation with the concentration of HCl acid.

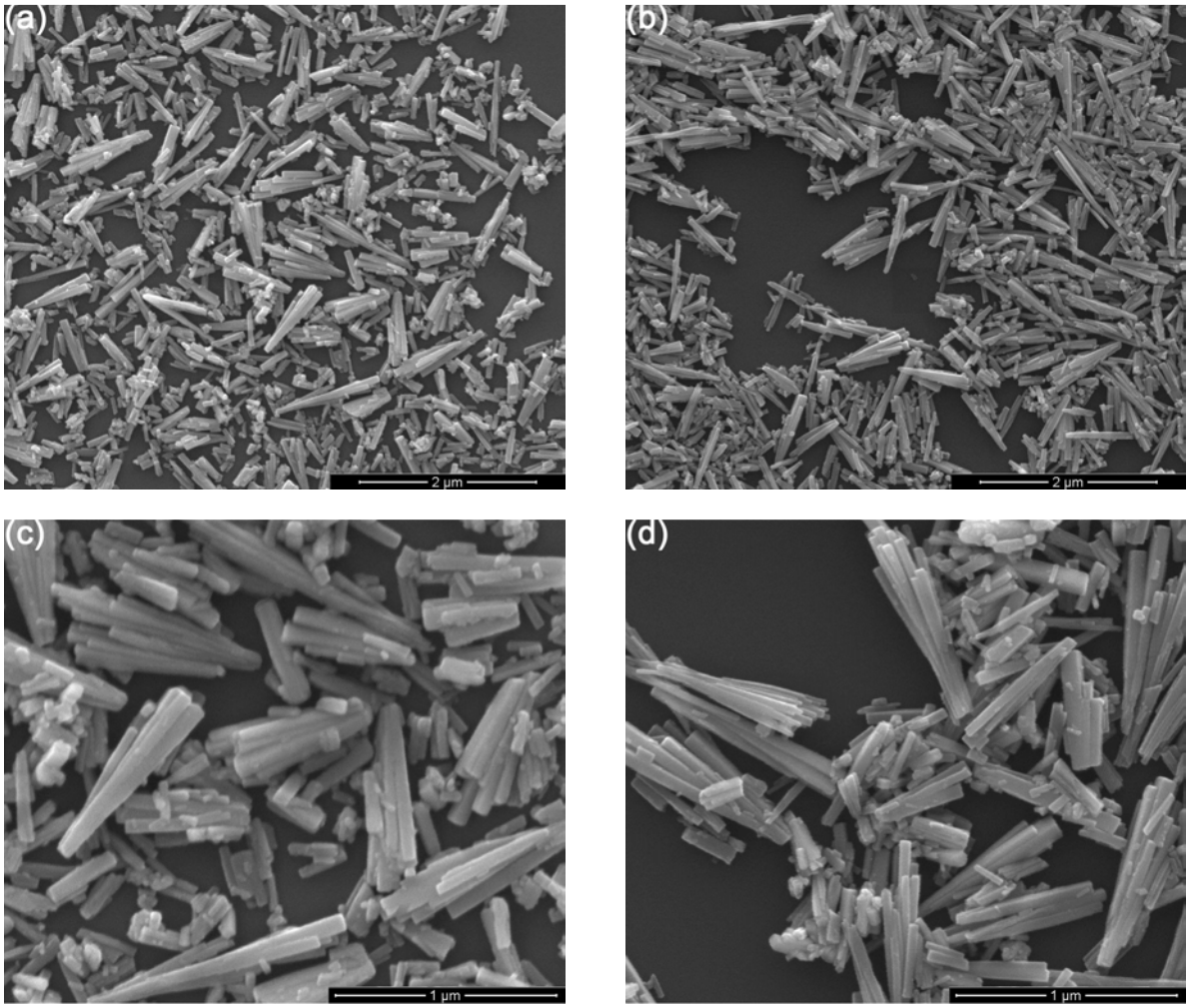

Fig. 3-11 SEM images of $ZrW_2O_7(OH)_2 \cdot 2H_2O$ synthesized under the following conditions: $ZrO(ClO_4)_2 \cdot xH_2O$ and $Na_2WO_4 \cdot 2H_2O$ mixture at 130 °C for 24 h in 5 M HCl at (a) 20000X and (c) 50000X, and 7 M HCl at (b) 20000X and (d) 50000X

However, the morphology of $ZrW_2O_7(OH)_2 \cdot 2H_2O$ changed slightly when using $ZrO(NO_3)_2 \cdot xH_2O$ and $Na_2WO_4 \cdot 2H_2O$ for the reaction in 5 M and 7 M HCl. As shown in Fig. 3-12, the particles synthesized in 5 M HCl appeared as individual rods with a width of 30-90 nm to

70-160 nm in 7 M HCl, but the particles tended to grow larger in crystallite size from 50 to 63 nm. In addition, the surface roughness was strongly dependent on the concentration of the acid. It was found that the particles present a higher roughness under 7 M HCl than 5 M HCl.

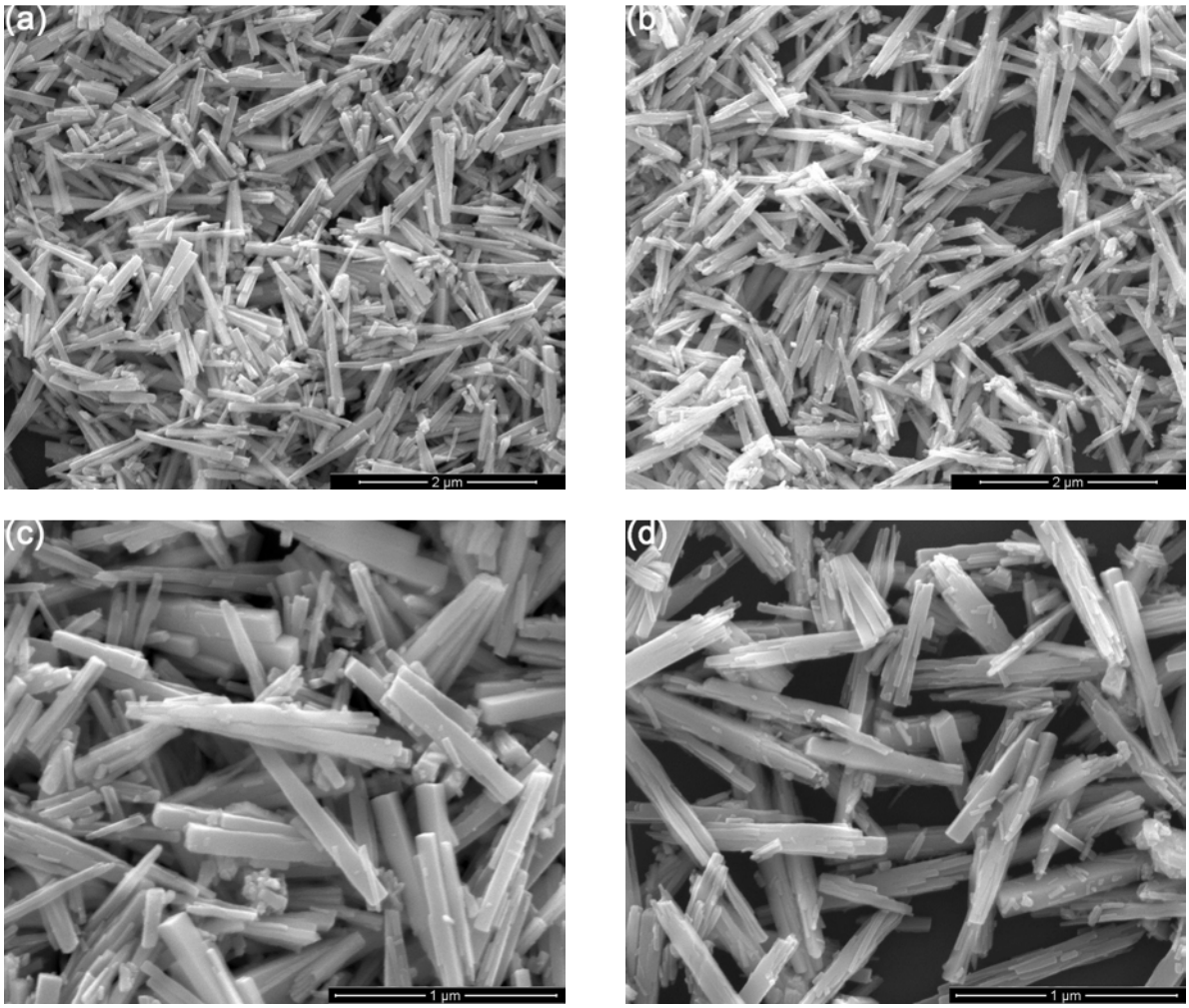

Fig. 3-12 SEM images of $ZrW_2O_7(OH)_2 \cdot 2H_2O$ synthesized under the following conditions: $ZrO(NO_3)_2 \cdot xH_2O$ and $Na_2WO_4 \cdot 2H_2O$ mixture at 130 °C for 24 h in 5 M HCl at (a) 20000X and (c) 50000X, and 7 M HCl at (b) 20000X and (d) 50000X

When $HClO_4$ was used as the acid for the reaction, it was found that in the mixture of ZrAc and $Na_2WO_4 \cdot 2H_2O$ the acid concentration was less effective in changing the morphologies of $ZrW_2O_7(OH)_2 \cdot 2H_2O$. This yielded similar dimensional sizes of nanoparticles with 0.3-1 µm in

length and by 50-100 nm in width as shown in Fig. 3-13. However, when compared with the nanoparticles obtained from different raw material systems, acid concentration showed significant effects on controlling the morphologies of the nanoparticles, especially on the extent of agglomeration among particles.

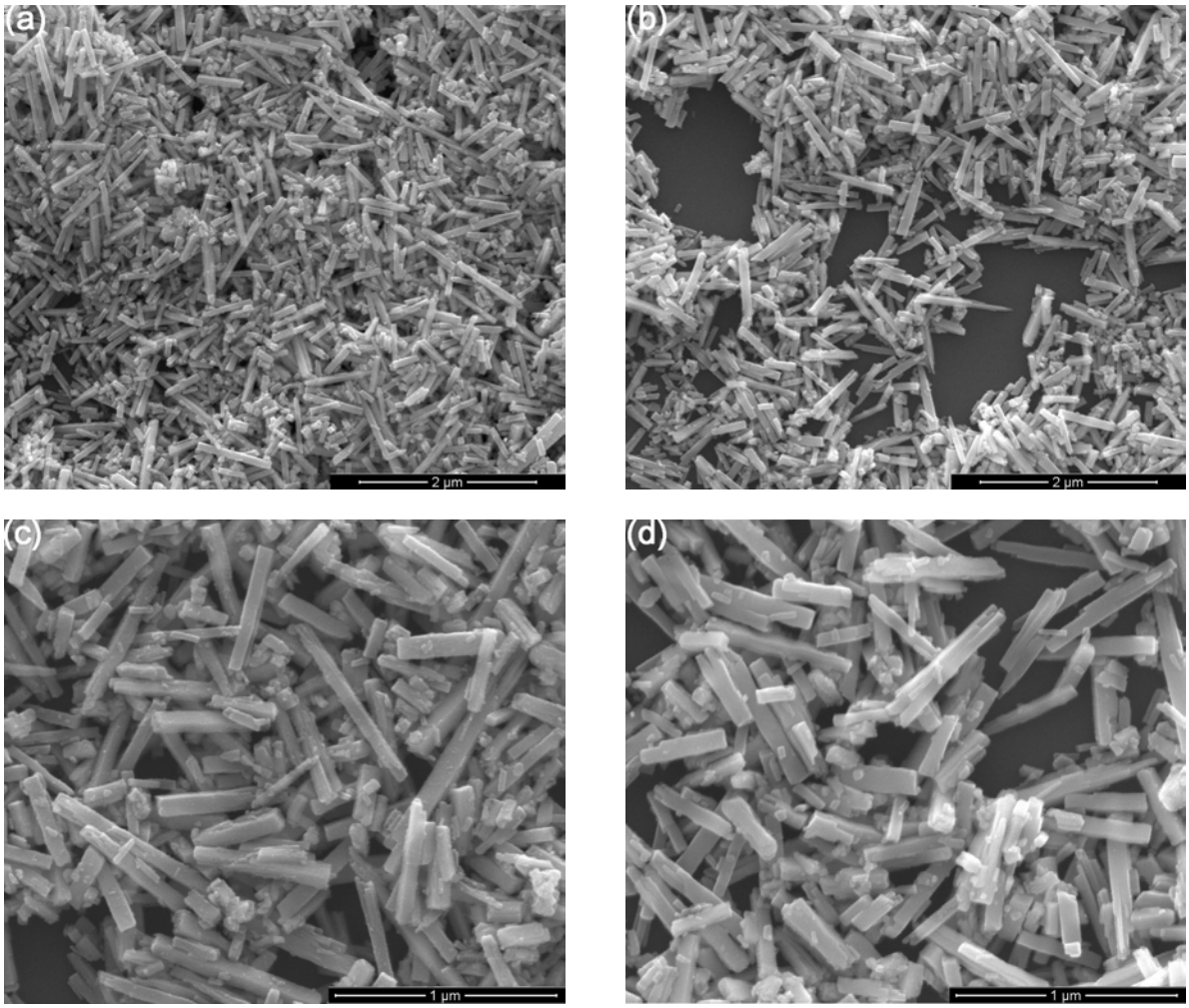

Fig. 3-13 SEM images of $ZrW_2O_7(OH)_2 \cdot 2H_2O$ synthesized under the following conditions: ZrAc and $Na_2WO_4 \cdot 2H_2O$ mixture at 130 °C for 24 h in 3 M $HClO_4$ at (a) 20000X and (c) 50000X, and 5 M $HClO_4$ at (b) 20000X and (d) 50000X

Fig. 3-14 and 3-15 show the influence of $HClO_4$ molarity on the morphologies of the nanoparticles. The synthesized $ZrW_2O_7(OH)_2 \cdot 2H_2O$ from the two mixtures ($ZrO(ClO_4)_2 \cdot xH_2O$ /

$Na_2WO_4 \cdot 2H_2O$ and $ZrO(NO_3)_2 \cdot xH_2O$ / $Na_2WO_4 \cdot 2H_2O$) displayed agglomeration in different degrees depending on the acid concentration that was used. For 3 M $HClO_4$, the nanoparticles got fused together lengthwise and edgewise between each individual particle. However, by increasing the acid to 5 M, the particles showed more severe agglomeration, the individual particles aggregated into large peanut-like particles and were difficult to be identified. Also when comparing the crystallite size of nanoparticles, the $ZrW_2O_7(OH)_2 \cdot 2H_2O$ with smaller crystallite sizes (17-20 nm) were obtained from higher concentrations of acid compared with lower concentrations, whose crystallites sizes were 32-35 nm which were similar to the widths of each individual nanoparticle from the SEM images. Based on the above observations, it can be concluded that when using the acidic $HClO_4$ medium, higher concentrations of counter-ions tended to restrict the growth of the crystals due to the strong agglomeration that occurs between the nanoparticles.

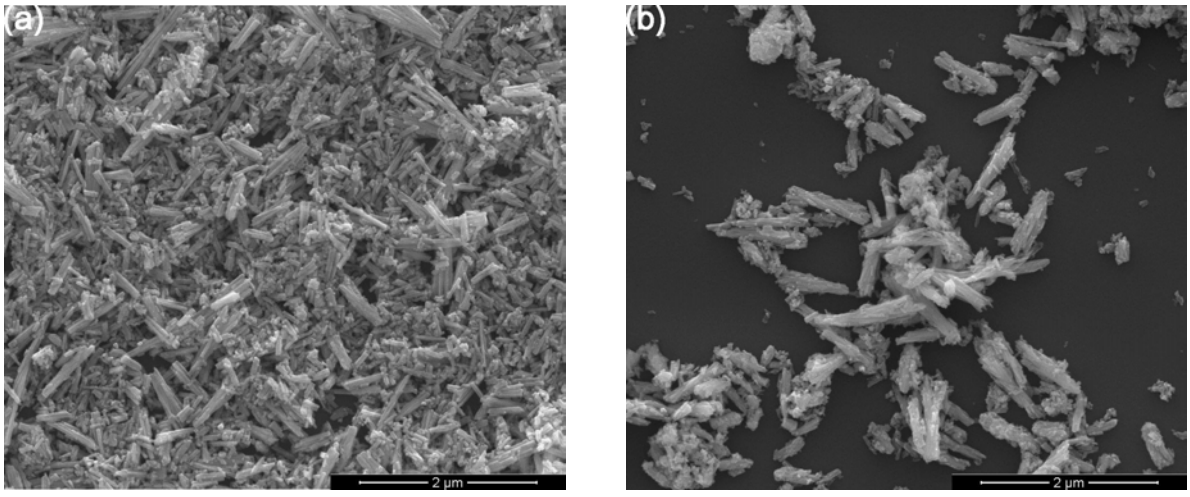

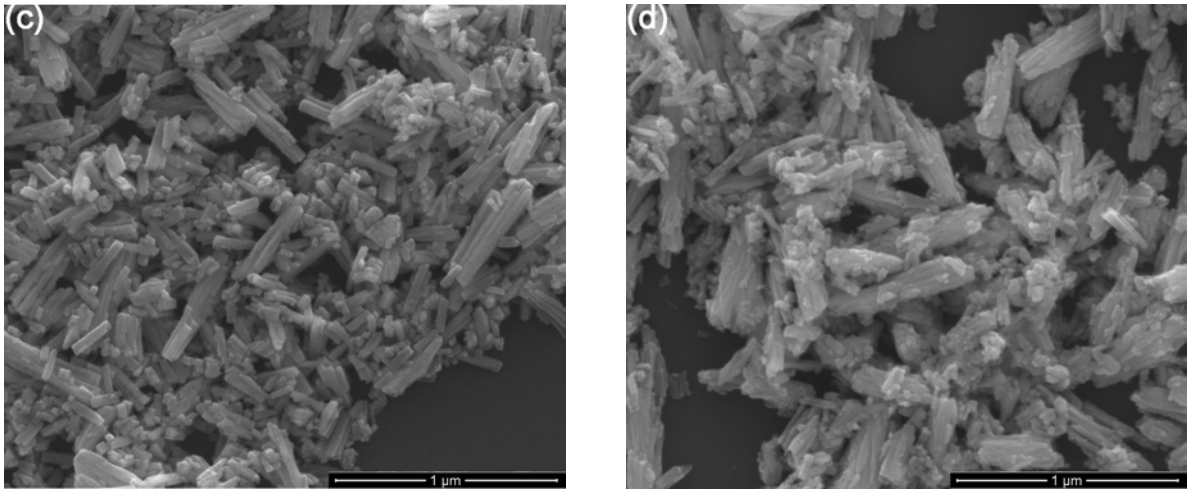

Fig. 3-14 SEM images of $ZrW_2O_7(OH)_2 \cdot 2H_2O$ synthesized under the following conditions: $ZrO(ClO_4)_2 \cdot xH_2O$ and $Na_2WO_4 \cdot 2H_2O$ mixture at 130 °C for 24 h in 3 M $HClO_4$ at (a) 20000X and (c) 50000X, and 5 M $HClO_4$ at (b) 20000X and (d) 50000X

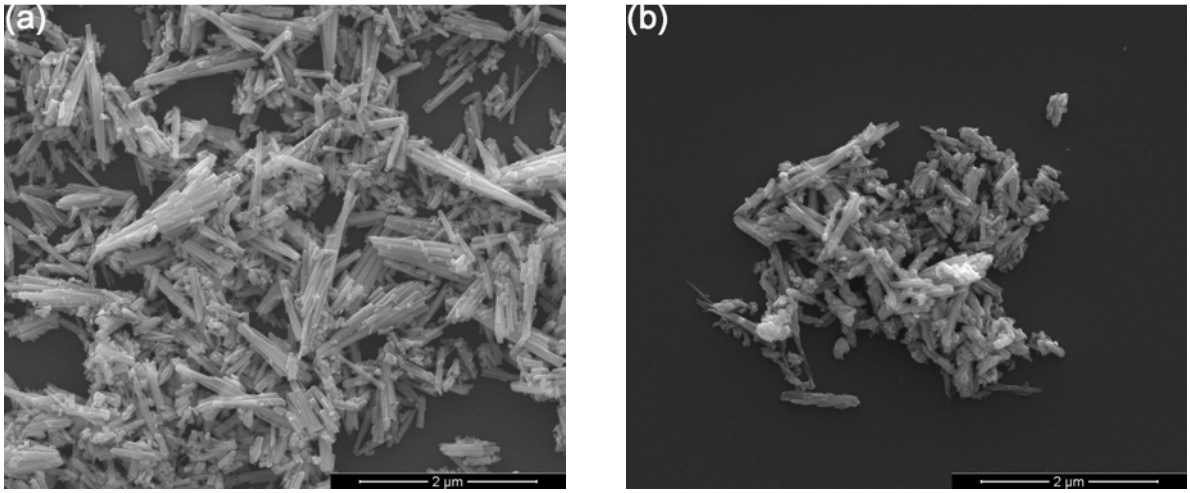

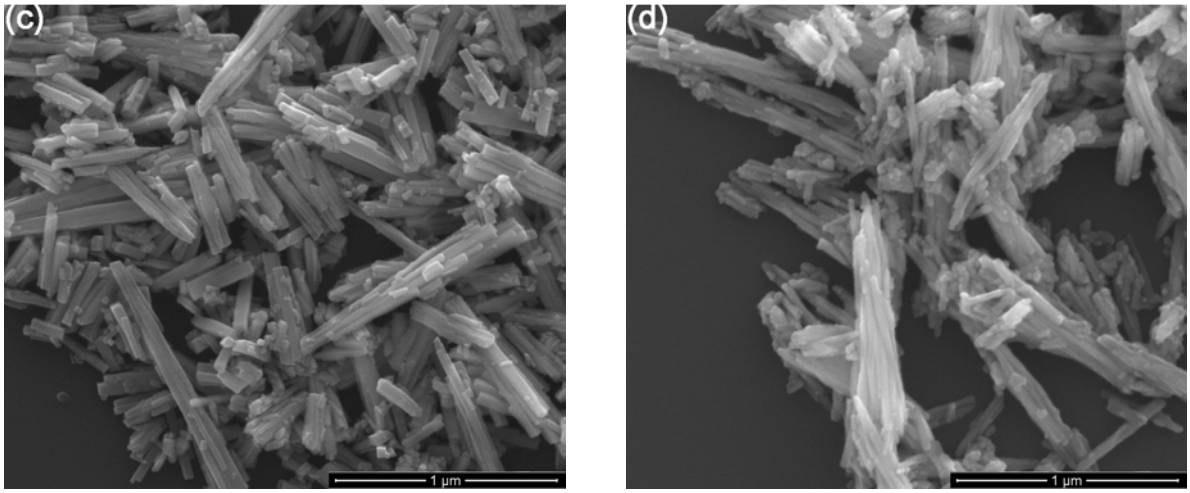

Fig. 3-15 SEM images of $ZrW_2O_7(OH)_2 \cdot 2H_2O$ synthesized under the following conditions: $ZrO(NO_3)_2 \cdot xH_2O$ and $Na_2WO_4 \cdot 2H_2O$ mixture at 130 °C for 24 h in 3 M $HClO_4$ at (a) 20000X and (c) 50000X, and 5 M $HClO_4$ at (b) 20000X and (d) 50000X

3.2.4 Effect of reaction temperature

Reaction temperature is another important experimental variable to control the growth of $ZrW_2O_7(OH)_2 \cdot 2H_2O$ nanoparticles in the hydrothermal reaction. In this experiment, two temperatures were studied to determine their effect on synthesis.

In case of the reaction of ZrAc and Na_2WO_4 solutions, 7 M HCl was used as shown in Fig. 3-16, and it was noted that the obtained $ZrW_2O_7(OH)_2 \cdot 2H_2O$ particles were found to be larger in size (200-800 nm by 50-100 nm) at 160 °C than the ones obtained at 130 °C (200-500 nm by 50-80 nm). This observation indicated that the higher temperature improved the crystallization and growth kinetics of the nanoparticles under a hydrothermal reaction.

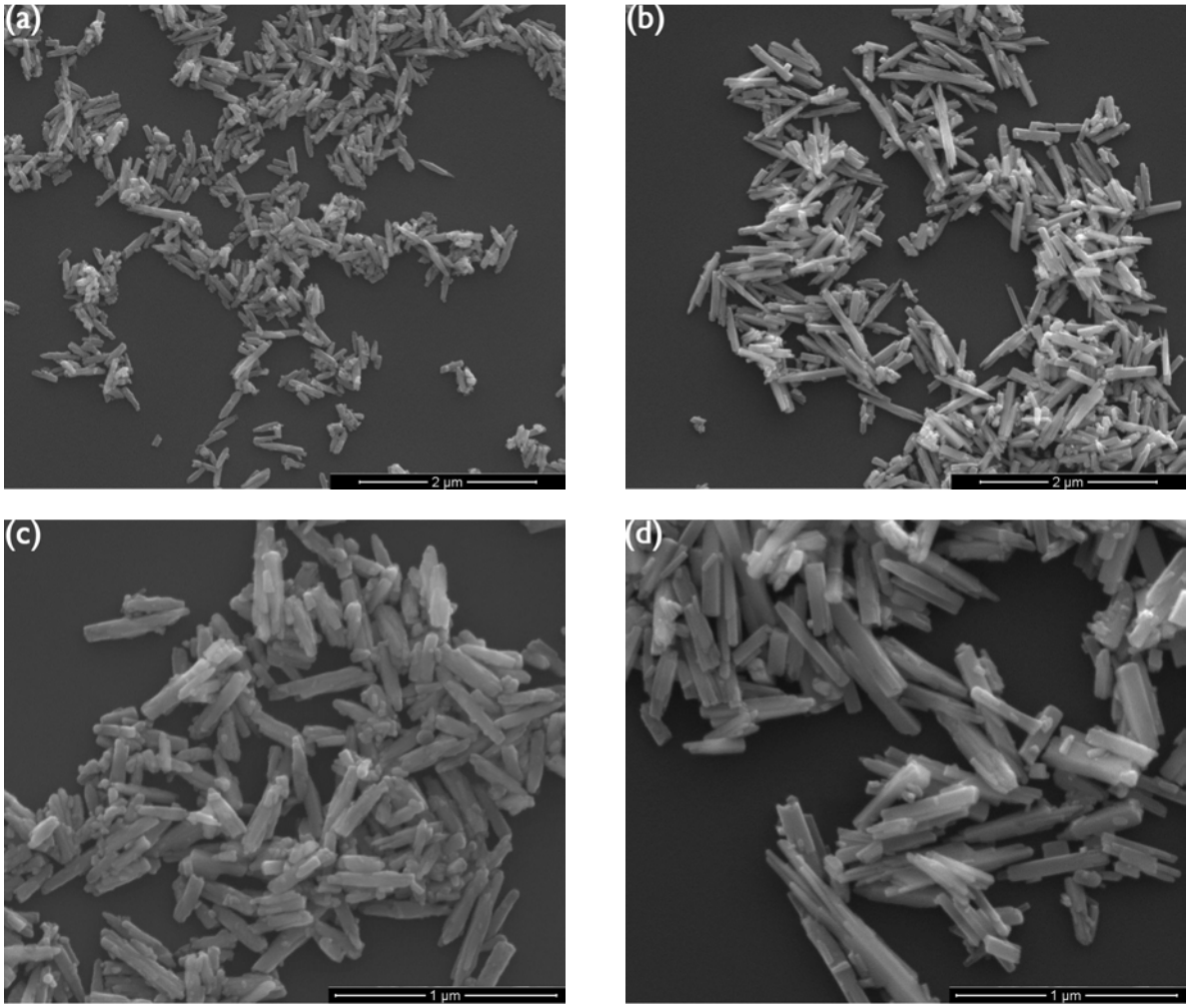

Fig. 3-16 SEM images of $ZrW_2O_7(OH)_2 \cdot 2H_2O$ synthesized under the following conditions: ZrAc and $Na_2WO_4 \cdot 2H_2O$ mixture for 12 h in 7 M HCl at 130 °C (a) 20000X and (c) 50000X, and at 160 °C (b) 20000X and (d) 50000X

Also, the same observation was shown in the same solution reacted in 3 M $HClO_4$. As the reaction was carried out at a higher temperature, the particles became much longer than the ones reacted at lower temperature. The size of $ZrW_2O_7(OH)_2 \cdot 2H_2O$ synthesized under 130 °C was 350-800 nm by 40-90 nm, but both of the length and width were nearly doubled by heating the temperature to 160 °C.

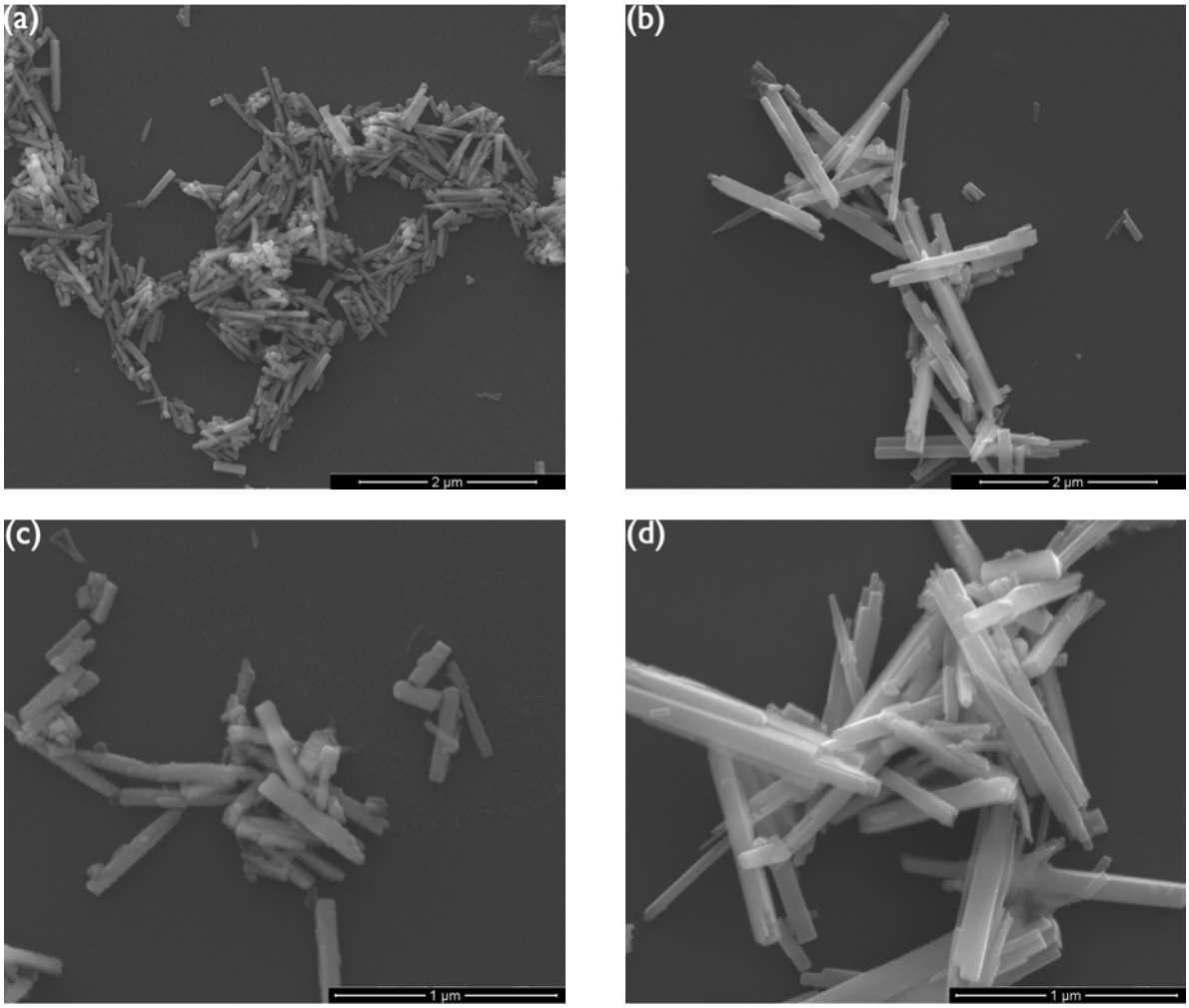

Fig. 3-17 SEM images of $ZrW_2O_7(OH)_2 \cdot 2H_2O$ synthesized under the following conditions: ZrAc and $Na_2WO_4 \cdot 2H_2O$ mixture for 12 h in 3 M $HClO_4$ at 130 °C (a) 20000X and (c) 50000X, and at 160 °C (b) 20000X and (d) 50000X

In the case of $ZrO(ClO_4)_2 \cdot xH_2O$ and $Na_2WO_4 \cdot 2H_2O$ reacted in 5 M HCl, the same bundle-like nanoparticles appeared at two different reaction temperatures, but the dimensional sizes for the obtained $ZrW_2O_7(OH)_2 \cdot 2H_2O$ varied. To be specific, the particles sizes were characterized as 0.4-1 µm by 40-80 nm when the reaction was carried on at 130 °C. While, the sizes of $ZrW_2O_7(OH)_2 \cdot 2H_2O$ synthesized at 160 °C were measured as 0.8-1.7 µm by 70-180 nm.

Since the width of the particles can be regarded as the crystallite size, reactions at a higher temperature facilitated the growth of crystals in a hydrothermal reaction.

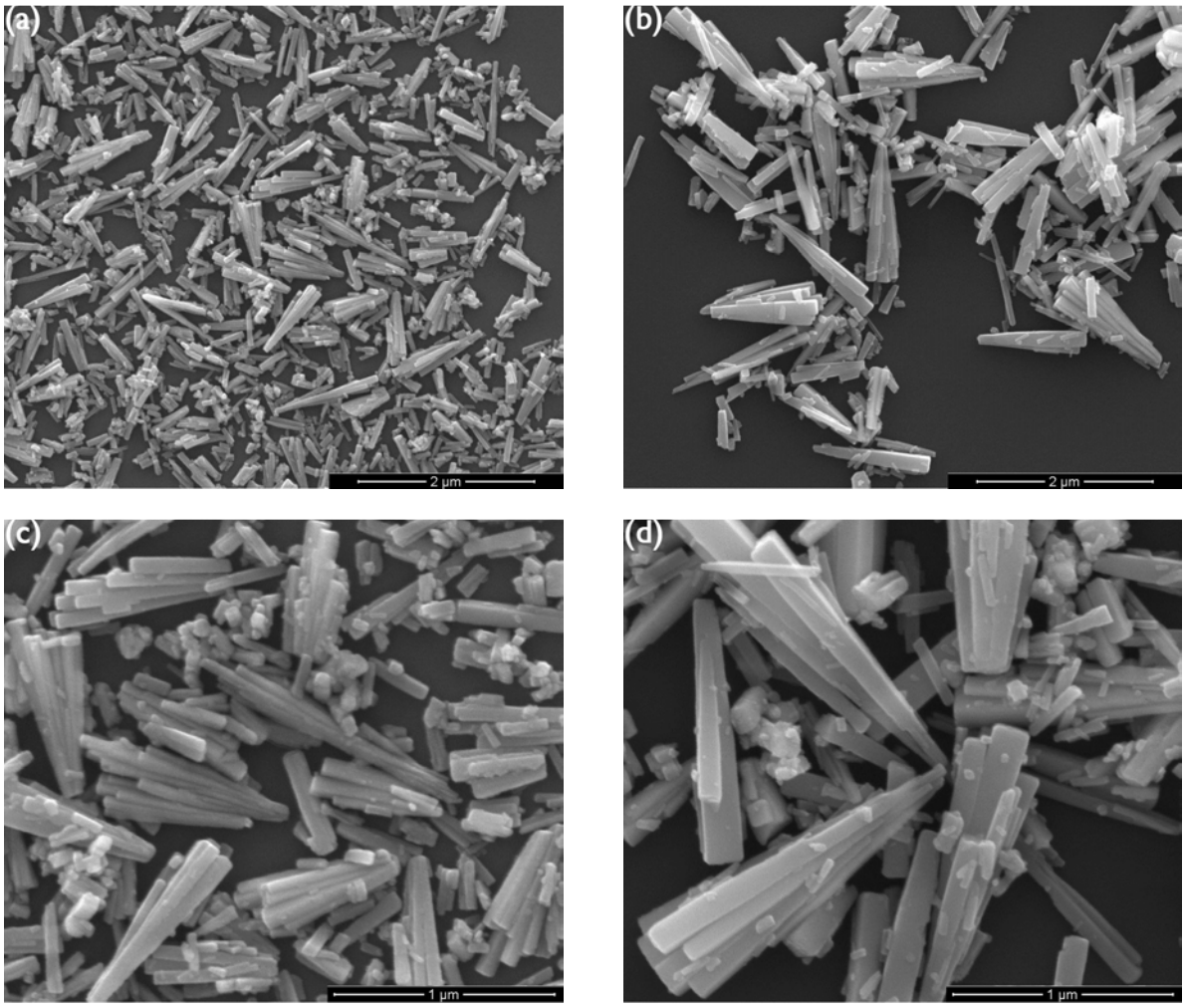

Fig. 3-18 SEM images of $ZrW_2O_7(OH)_2 \cdot 2H_2O$ synthesized under the following conditions: $ZrO(ClO_4)_2 \cdot xH_2O$ and $Na_2WO_4 \cdot 2H_2O$ mixture for 12 h in 5 M HCl at 130 °C (a) 20000X and (c) 50000X, and at 160 °C (b) 20000X and (d) 50000X

When the same reactants reacted in 3 M $HClO_4$ for temperature comparison, a similar trend of increased nanoparticle size was shown, Fig. 3-19. At relatively low temperatures, particles performed slight agglomeration by joining smaller individual nanoparticles of sizes 200-450 nm by 30-70 nm. These particles were found to be extensively longer in length (1-2 µm)

but the widths were unchanged (30-90 nm). Also based on the comparison of SEM images, the degree of agglomeration was not strongly correlated to the reaction temperature as was the acid concentration.

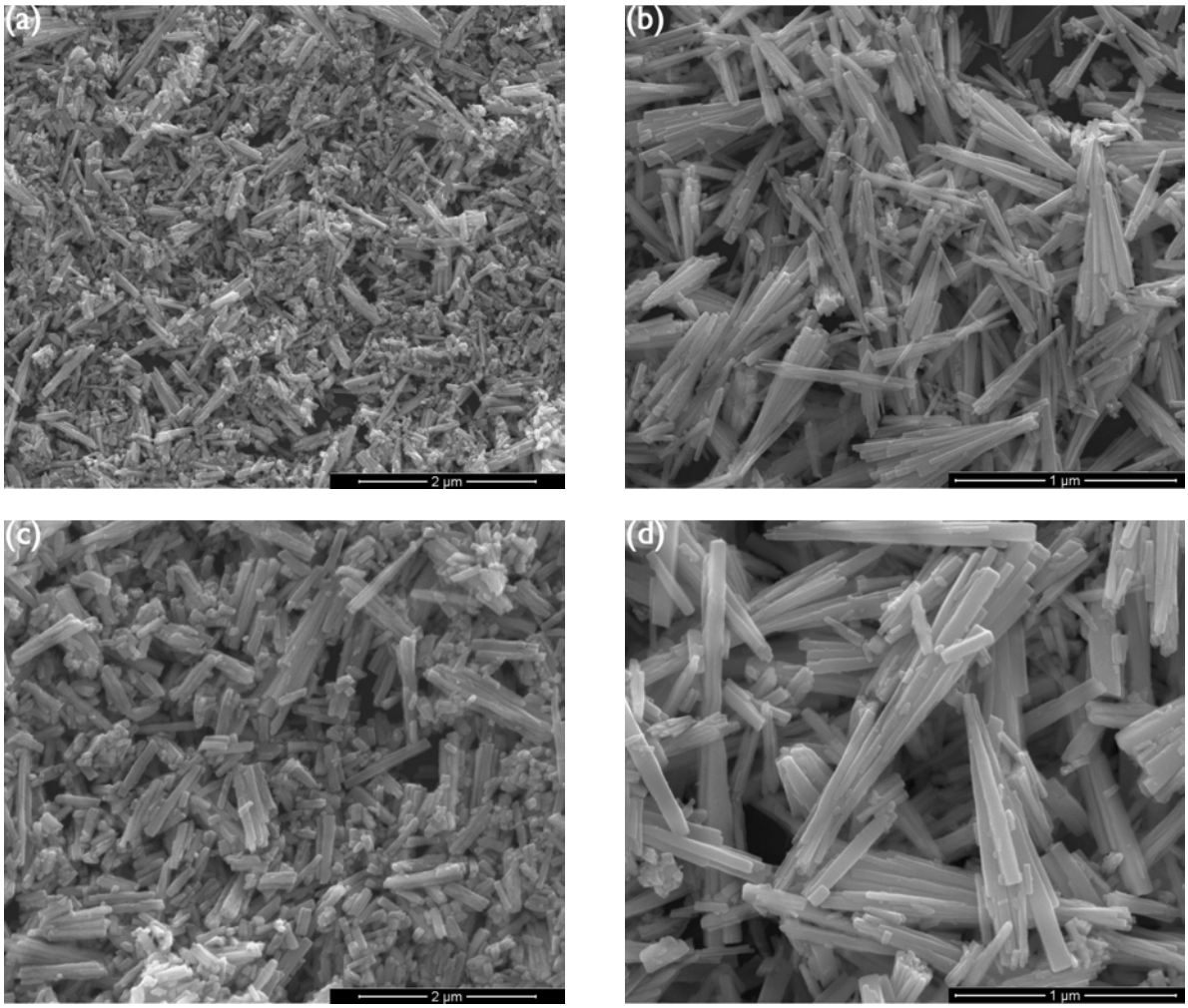

Fig. 3-19 SEM images of $ZrW_2O_7(OH)_2 \cdot 2H_2O$ synthesized under the following conditions: $ZrO(ClO_4)_2 \cdot xH_2O$ and $Na_2WO_4 \cdot 2H_2O$ mixture for 12 h in 3 M $HClO_4$ at 130 °C (a) 20000X and (c) 50000X, and at 160 °C (b) 20000X and (d) 50000X

When switching to the new reaction system of $ZrO(NO_3)_2 \cdot xH_2O$ and $Na_2WO_4 \cdot 2H_2O$ taking place in 5M HCl, the morphologies of the obtained $ZrW_2O_7(OH)_2 \cdot 2H_2O$ were characterized as individual rectangular rods, as shown in Fig. 3-20. To study the effect of

temperature on the morphologies, 130°C and 160 °C were again tested. As the reaction proceeded at a low temperature, the sizes of synthesized nanoparticles showed a length of 0.4-1.3 µm and a width of 30-90 nm, the crystallite size was 40 nm. Yet, it was noted that the obtained $ZrW_2O_7(OH)_2 \cdot 2H_2O$ appeared to be 0.3-1.3 µm by 50-170 nm, and the crystallite size became as large as 60 nm.

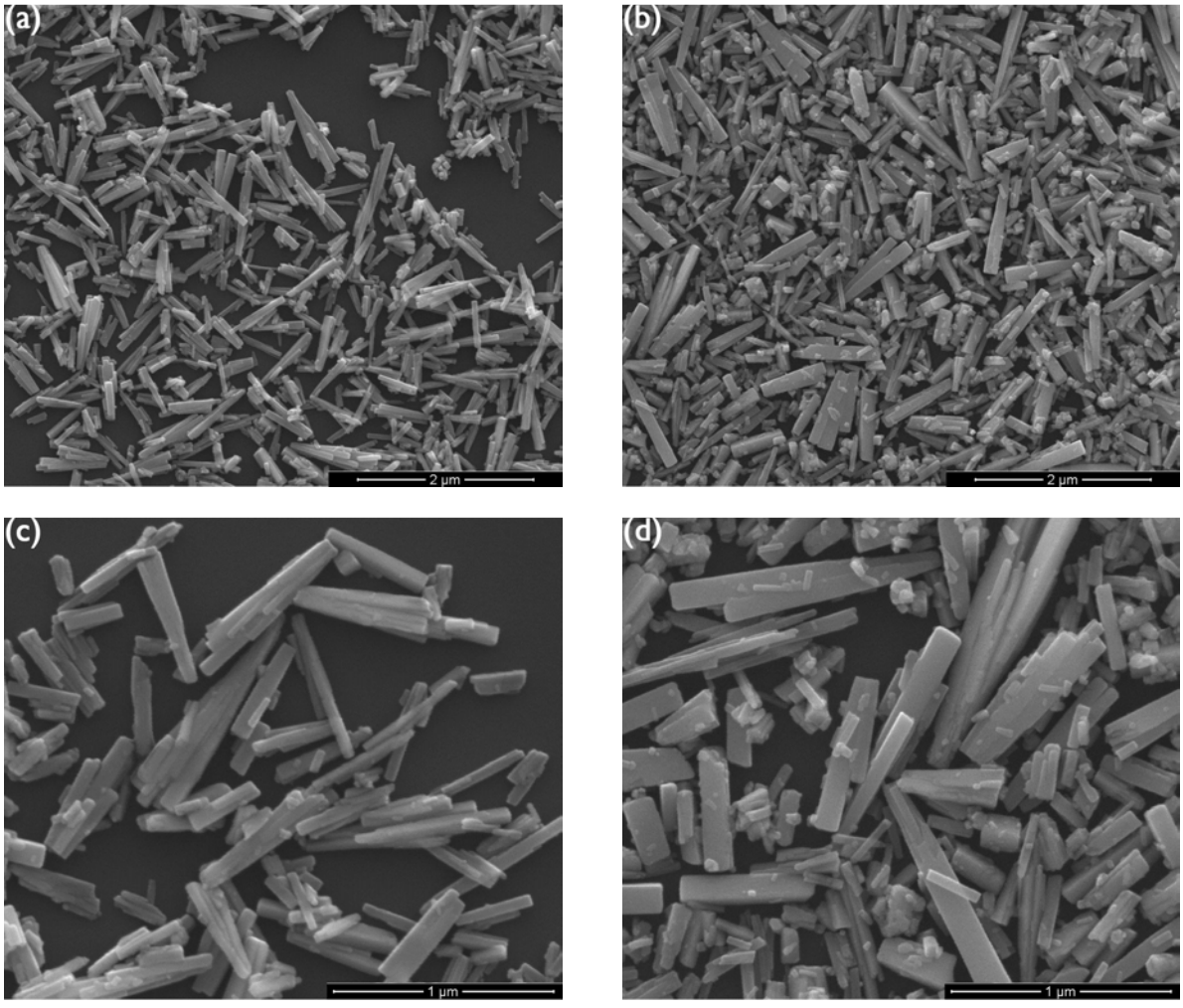

Fig. 3-20 SEM images of $ZrW_2O_7(OH)_2 \cdot 2H_2O$ synthesized under the following conditions: $ZrO(NO_3)_2 \cdot xH_2O$ and $Na_2WO_4 \cdot 2H_2O$ mixture for 12 h in 5 M HCl at 130 °C (a) 20000X and (c) 50000X, and at 160 °C (b) 20000X and (d) 50000X

Interestingly in case of $HClO_4$, a similar observation of a change in nanoparticle morphology again occurred between different reaction systems of $ZrO(ClO_4)_2 \cdot xH_2O$ / $Na_2WO_4 \cdot 2H_2O$ in 3 M $HClO_4$ as previously studied. The particles were generated into a slightly agglomerated form at 130 °C, with length of 150-500 nm and width of 30-60 nm for the individual nanoparticles. As the reaction temperature was raised to 160 °C, the slightly aggregated nanoparticles grew larger along the length without changing crystallite size (ca. 20 nm). The dimensional scale of the $ZrW_2O_7(OH)_2 \cdot 2H_2O$ was measured as 0.5-1.5 µm by 70-180 nm.

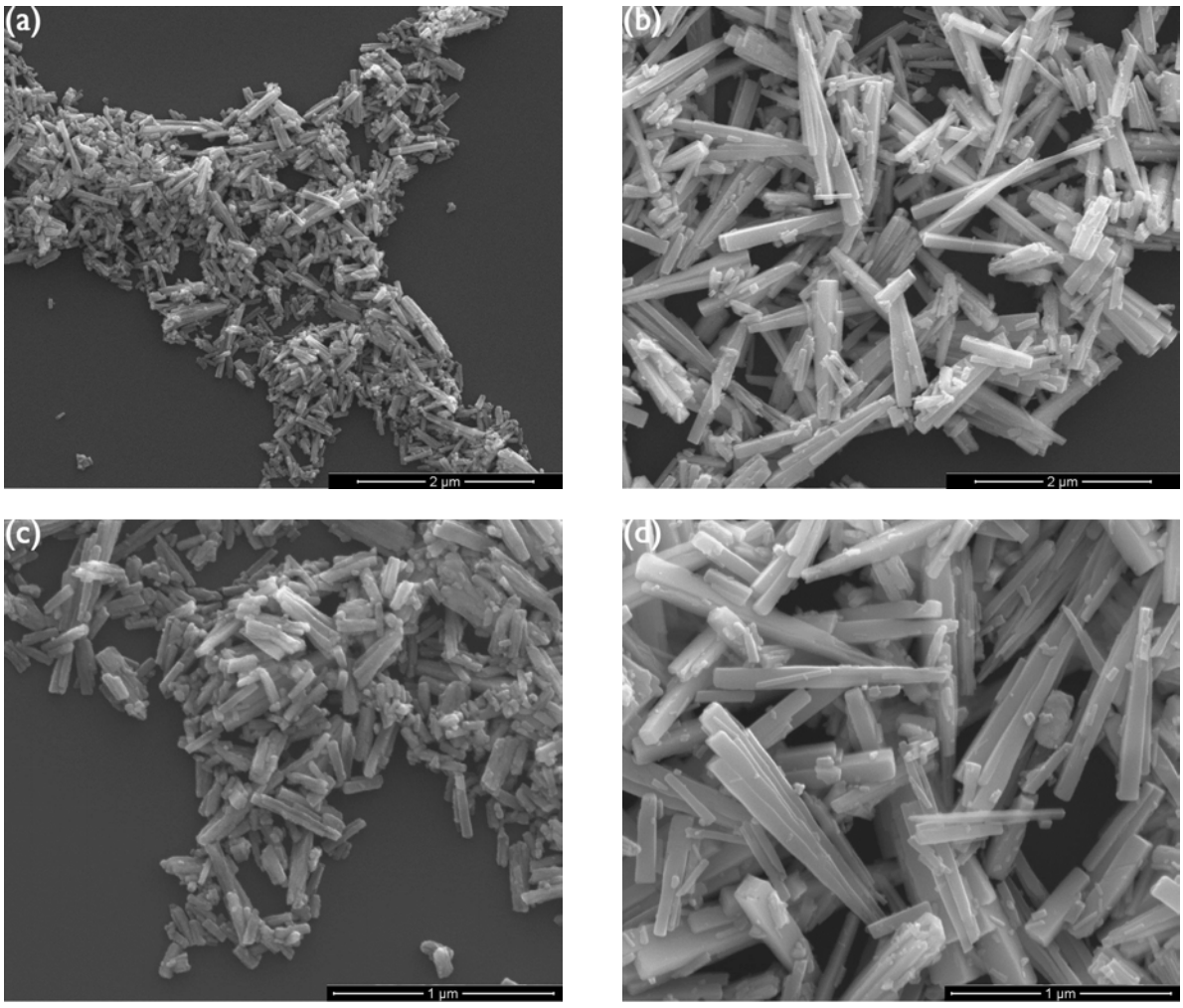

Fig. 3-21 SEM images of $ZrW_2O_7(OH)_2 \cdot 2H_2O$ synthesized under the following conditions: $ZrO(NO_3)_2 \cdot xH_2O$ and $Na_2WO_4 \cdot 2H_2O$ mixture for 12 h in 3 M $HClO_4$ at 130 °C (a) 20000X and (c) 50000X, and at 160 °C (b) 20000X and (d) 50000X

Based on the comparison of the effect of temperature on the morphology of $ZrW_2O_7(OH)_2 \cdot 2H_2O$, the crystallization and growth of the nanoparticles can be facilitated with a higher temperature, and the particles become larger in size-scale compared with the ones yielded at a lower temperature.

3.2.5 Effect of reaction time

After studying the effect of synthetic parameters on the morphologies and crystallite sizes of $ZrW_2O_7(OH)_2 \cdot 2H_2O$ nanoparticles including the variations in initial reactants, acids and reaction temperature, the last variable to be investigated experimentally was the hydrothermal reaction time. Based on all the conducted experiments, the effect of reaction time on the morphologies of the nanoparticles was not as obvious as in the previously studied variables. There were only three batches of experiments that reacted in the 3 M $HClO_4$ solution at 130 °C and displayed observational changes in morphologies. Also, the crystallite sizes of the synthesized $ZrW_2O_7(OH)_2 \cdot 2H_2O$ appeared slightly different when the reaction was proceeded at different reaction times. From general observation, it was concluded that the nanoparticles synthesized at a longer reaction time appeared larger in both crystallite size and nanoparticle size. The reason for this can be explained by Ostwald ripening, which states that small crystals dissolve and redeposit onto other crystals in a solution to form larger particles.

As shown in Fig. 3-22, the $ZrW_2O_7(OH)_2 \cdot 2H_2O$ nanoparticles appeared as individual rectangular shapes obtained from the ZrAc solution and $Na_2WO_4 \cdot 2H_2O$ mixture reacted at 130 °C. As the reaction proceded for 12 h, the dimensional scale of the nanoparticles was characterized as 350-800 nm by 40-90 nm. The $ZrW_2O_7(OH)_2 \cdot 2H_2O$ grew slightly longer to a

length of 0.5-1 μm if the reaction time was doubled. However, the crystallite size and average width of nanoparticles was sustained even if the reaction time was varied. This indicated that reaction time merely effected the growth of nanoparticles lengthwise as long as the crystallization was completed.

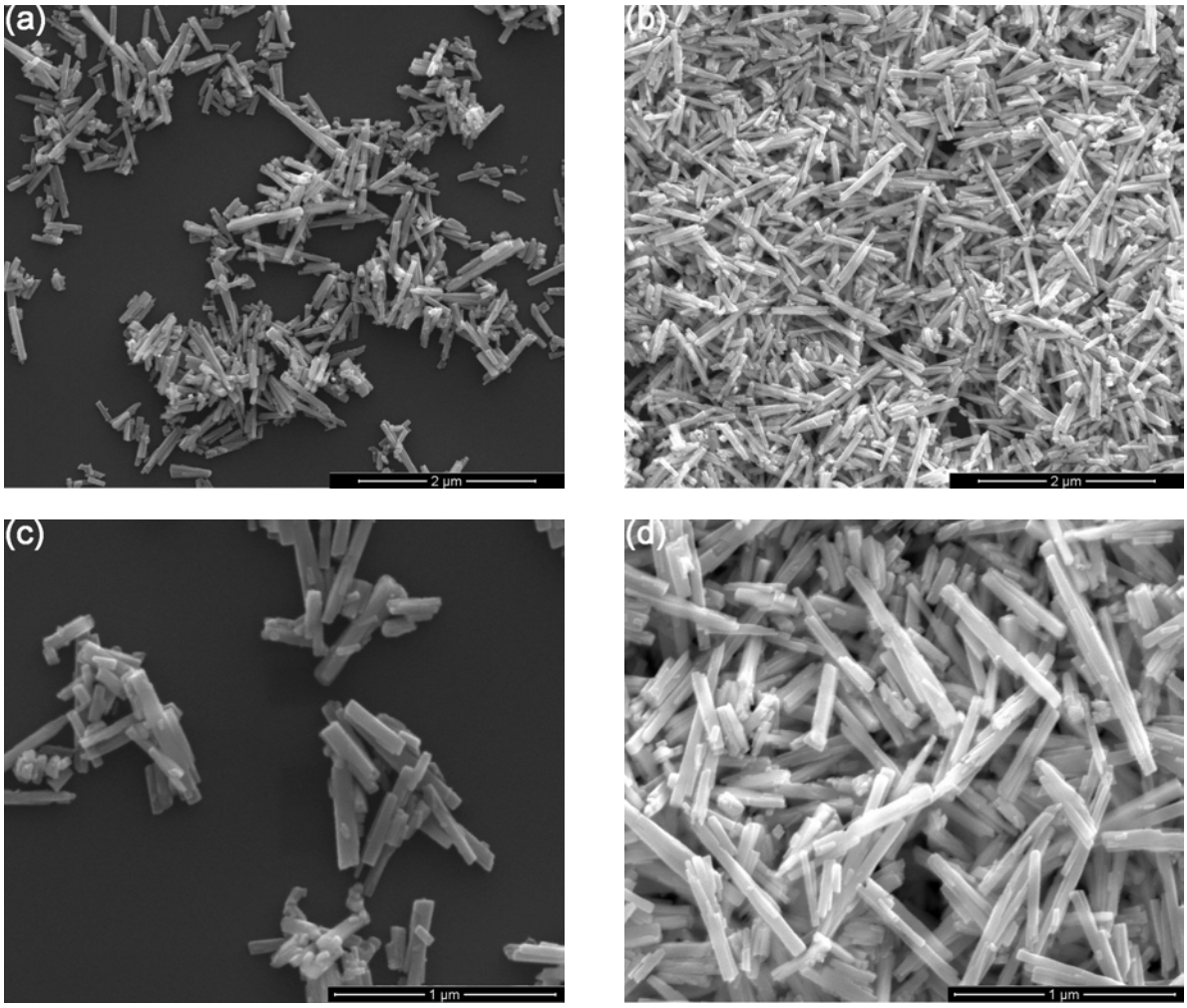

Fig. 3-22 SEM images of $ZrW_2O_7(OH)_2 \cdot 2H_2O$ synthesized under the following conditions: ZrAc solution and $Na_2WO_4 \cdot 2H_2O$ mixture in 3 M $HClO_4$ at 130 °C for 12 h at (a) 20000X and (c) 50000X, and for 24 h at (b) 20000X and (d) 50000X

When the reaction time was varied in another system, the same observation occurred, which confirmed the effect of the reaction time on controlling the growth of $ZrW_2O_7(OH)_2 \cdot 2H_2O$

in a hydrothermal synthetic approach. The nanoparticles obtained from a $ZrO(ClO_4)_2 \cdot xH_2O$ / $Na_2WO_4 \cdot 2H_2O$ solution related for 12 h appeared as lightly agglomerated short rods that were 200-450 nm in length and 30-70 nm in width. As expected, the short rods became significantly longer up to 1 µm as the experiment proceeded for a longer reaction time, which can be observed in Fig. 3-23.

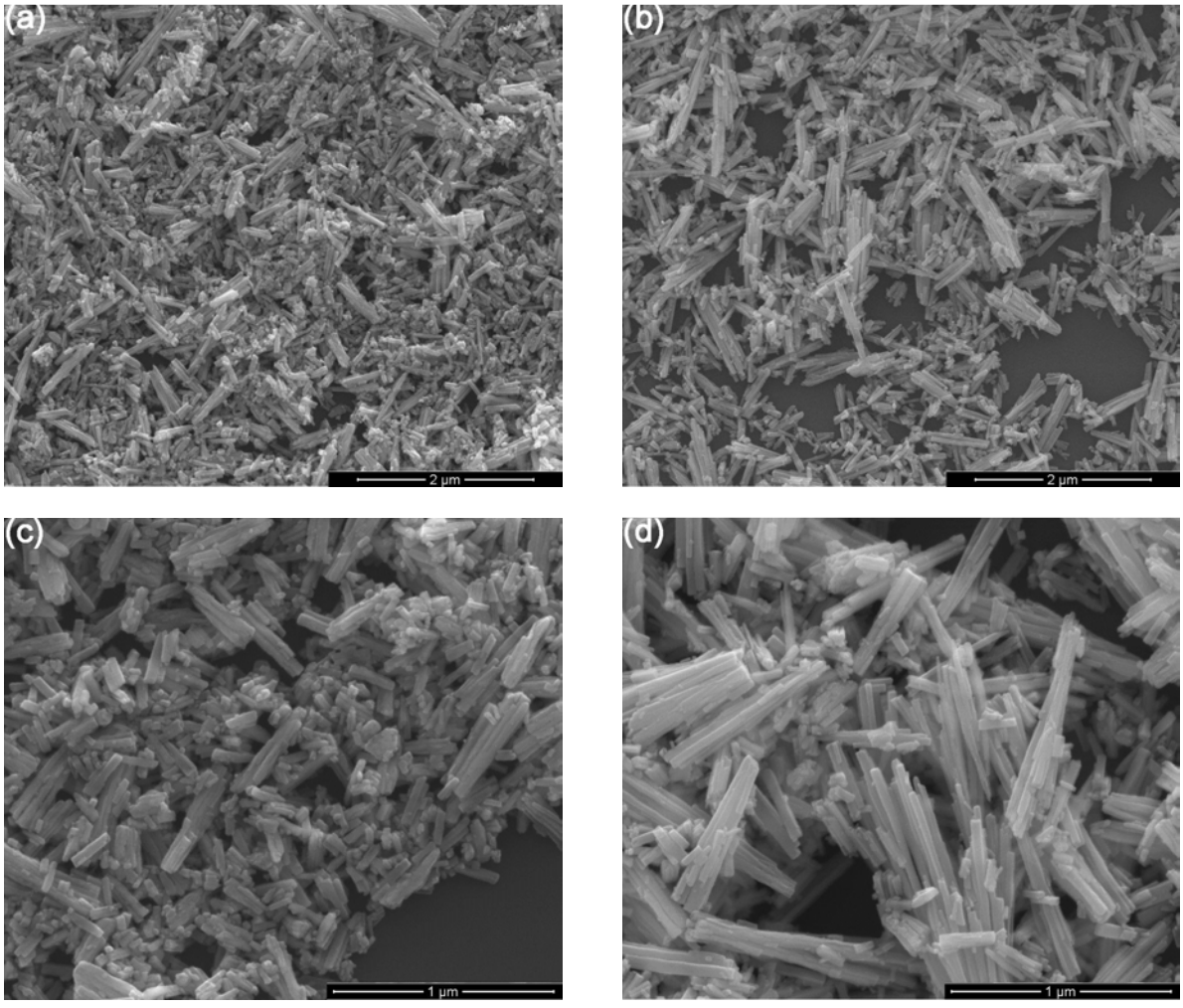

Fig. 3-23 SEM images of $ZrW_2O_7(OH)_2 \cdot 2H_2O$ synthesized under the following conditions: $ZrO(ClO_4)_2 \cdot xH_2O$ and $Na_2WO_4 \cdot 2H_2O$ mixture in 3 M $HClO_4$ at 130 °C for 12 h at (a) 20000X and (c) 50000X, and for 24 h at (b) 20000X and (d) 50000X

As the reaction system comprised of $ZrO(NO_3)_2 \cdot xH_2O$ and $Na_2WO_4 \cdot 2H_2O$ progressed, the morphologies of the synthesized $ZrW_2O_7(OH)_2 \cdot 2H_2O$ appeared similar to the previously discussed reaction system of $ZrO(ClO_4)_2 \cdot xH_2O$ and $Na_2WO_4 \cdot 2H_2O$. Observed in Fig. 3-24, $ZrW_2O_7(OH)_2 \cdot 2H_2O$ nanoparticles showed increasing lengths from 150-500 nm to 0.3-1.3 µm as reaction time was prolonged from 12 h to 24 h.

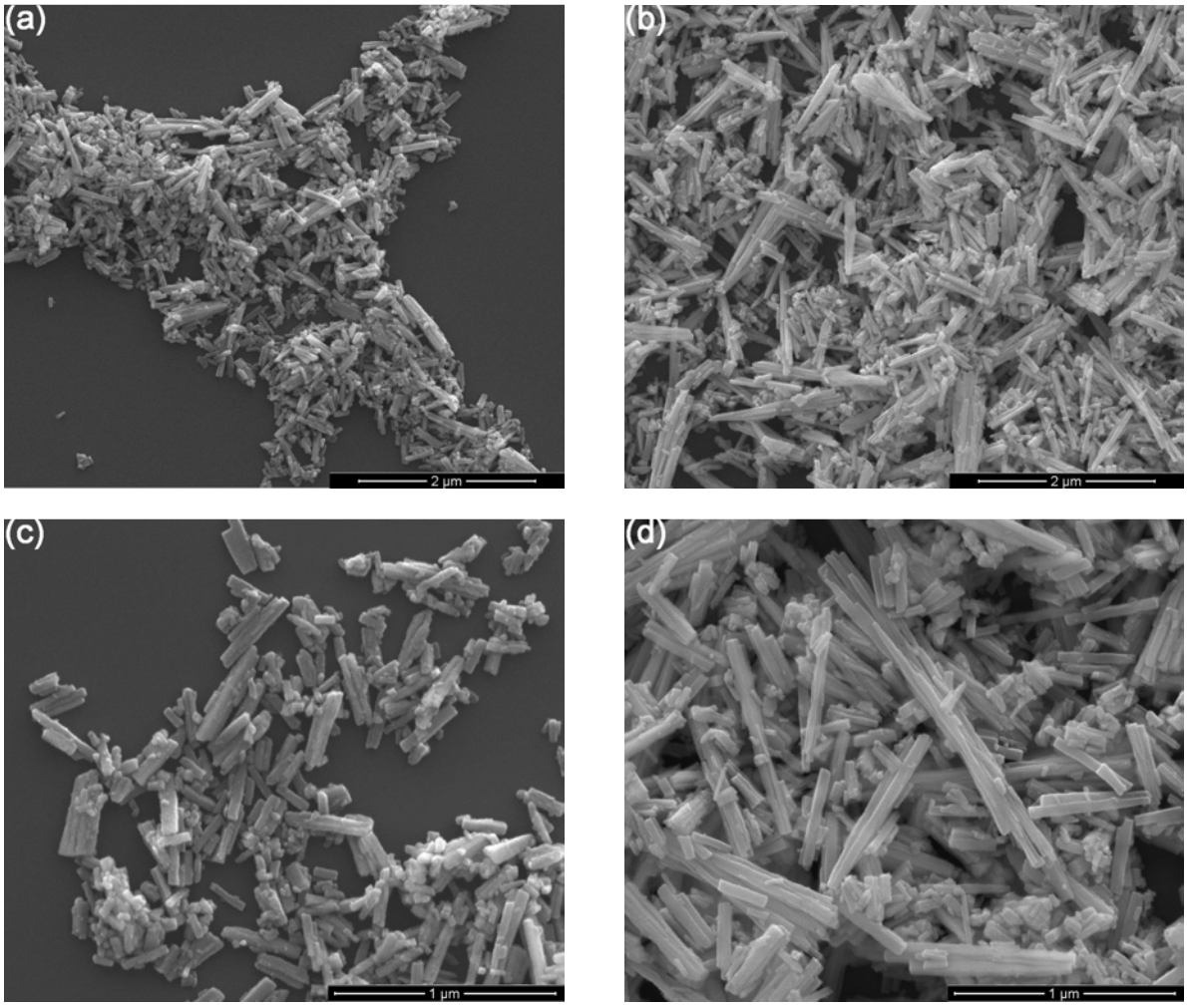

Fig. 3-24 SEM images of $ZrW_2O_7(OH)_2 \cdot 2H_2O$ synthesized under the following conditions: $ZrO(NO_3)_2 \cdot xH_2O$ and $Na_2WO_4 \cdot 2H_2O$ mixture in 3 M $HClO_4$ at 130 °C for 12 h at (a) 20000X and (c) 50000X, and for 24 h at (b) 20000X and (d) 50000X

Table 3-1. Summary of experimental variables and description of $ZrW_2O_7(OH)_2 \cdot 2H_2O$

Materials	Acid	Reaction time	Reaction temperature	Particle shapes	Particle sizes	Crystalline sizes
$ZrAc/Na_2WO_4$	5M HCl	12 h	130 °C	Individual long rods (fine surface) Individual long rods (fine surface)	0.2-1 µm by 30-70 nm	34±5 nm
		24 h			0.3-1 µm by 30-70 nm	29±3 nm
		12 h	160 °C		0.3-1.5 µm by 60-120 nm	46±2 nm
	7M HCl	12 h	130 °C	Individual short rods (rough surface)	200-500 nm by 50-80 nm	30±3 nm
		24 h			300-800 nm by 50-80 nm	26±4 nm
		12 h	160 °C		200-800 nm by 50-100 nm	38±2 nm
	3M $HClO_4$	12 h	130 °C	Individual long & regular rods (fine surface)	350-800 nm by 40-90 nm	30±1 nm
		24 h			0.5-1 µm by 50-100 nm	34±2 nm
		12 h	160 °C		1-2 µm by 60-150 nm	59±1 nm
	5M $HClO_4$	12 h	130 °C	Individual long & regular rods (fine surface)	0.3-1 µm by 50-90 nm	42±4 nm
		24 h			300-800nm by 50-90nm	31±4 nm
		12 h	160 °C		0.3-1.5 µm by 60-120 nm	47±2 nm
$ZrO(ClO_4)_2/Na_2WO_4$	5M HCl	12 h	130 °C	Bundle-like rods	0.4-1.5 µm by 40-80 nm	43±1 nm
		24 h			300-800 nm by 40-70 nm	46±3 nm
		12 h	160 °C	Large bundle-like rods (fine surface)	0.5-1.7 µm by 70-180 nm	65±2 nm
	7M HCl	12 h	130 °C	Bundle-like rods	300-900 nm by 30-80 nm	45±3 nm
		24 h			300-800 nm by 40-80 nm	50±1 nm
		12 h	160 °C	Large Bundle-like rods	1-1.5 µm by 90-150 nm	66±1 nm
	3M $HClO_4$	12 h	130 °C	Lightly agglomerated	200-450 nm by 30-70 nm	24±2 nm

				short and thin rods		
		24 h		Agglomerated short and thin rods	0.4-1 µm by 20-50 nm	32±5 nm
		12 h	160 °C	Bundle-like thin and long rods	1-2 µm by 30-90 nm	39±1 nm
	5M $HClO_4$	12 h	130 °C	Thin rods agglomerating into large rods	300-900 nm by 10-40 nm (Individual) to 100-300 nm (agglomeration)	17±3 nm
		24 h			0.3-1 µm by 10-40 nm (Individual) to 90-150 nm (agglomeration)	17±4 nm
		12 h	160 °C	N/A	N/A	Amorphous
$ZrO(NO_3)_2$/ Na_2WO_4	5M HCl	12 h	130 °C	Long and thin bundle-like rods (fine surface)	0.4-1.3 µm by 30-90 nm	40±2 nm
		24 h		Slightly agglomerated long and thin bundle-like rods (fine surface)	0.4-1.2 µm by 30-90 nm	50±3 nm
		12 h	160 °C	Mixture of individual and bundle-like various sizes rods (fine surface)	0.3-1.3 µm by 50-170 nm	60±2 nm
	7M HCl	12 h	130 °C	Individual large rods (rough surface)	0.5-1.5 µm by 70-180 nm	38±1 nm
		24 h			0.5-1.2 µm by 70-160 nm	63±1 nm
		12 h	160 °C	Individual multiple-sized rods (rough surface)	0.3-1 µm by 70-130 nm	60±6 nm
	3M $HClO_4$	12 h	130 °C	Lightly agglomerated	150-500 nm by 30-60 nm	26±3 nm

				small and regular rods		
		24 h		Agglomerated long and thin rods	0.3-1.3 µm by 30-70 nm	35±2 nm
		12 h	160 °C	Lightly agglomerated very long rods	0.5-1.5 µm by 70-180 nm	39±4 nm
	5M $HClO_4$	12 h	130 °C	Highly agglomerated multiple undefined shapes	300-800 nm by 30-70 nm	20±1 nm
		24 h		Highly agglomerated long and thin rods	0.5-1 µm by 20- 70 nm	20±2 nm
		12 h	160 °C	N/A	N/A	Amorphous

* $ZrW_2O_7(OH)_2 \cdot 2H_2O$ nanoparticles synthesized by $Na_6W_{12}O_{39} \cdot xH_2O$ and $(NH_4)_6H_2W_{12}O_{40} \cdot xH_2O$ were not included due to inhomogeneous of size-scales of nanoparticles

3.3 Conclusion

In this chapter, a series of systematic studies on the effects of synthetic variables including different initial raw materials, acid types, acid concentration, reaction time and reaction temperature on morphologies and crystallite sizes of $ZrW_2O_7(OH)_2 \cdot 2H_2O$ nanoparticles were conducted. Based on these series of experiments, the morphologies of synthesized $ZrW_2O_7(OH)_2 \cdot 2H_2O$ nanoparticles were found to be greatly dependent on the chosen initial reactants and the particles with the most optimized homogenous size distribution and shape can be obtained by using $Na_2WO_4 \cdot 2H_2O$ as the tungsten source. The acidic medium played significant role in controlling the nanoparticle's morphology and crystallite sizes as well. As the reaction proceeded in HCl, the obtained particles appeared as individual well defined shapes and the surface roughness was influenced by the acidic molarity. While the nanoparticles obtained from the $HClO_4$ solution showed the morphologies as agglomerated forms that aggregated by

several thin individual nanoparticles lengthwise, the extent of the agglomeration was dependent on the concentration of the acid. It was also observed from the experiments that reaction temperature affected the kinetic crystallization of $ZrW_2O_7(OH)_2 \cdot 2H_2O$. Higher temperatures tended to accelerate the crystal growth of the nanoparticles and resulted in larger particles' dimensional sizes and crystallite sizes. Lastly, reaction time had the least apparent effect on the morphologies compared to the other parameters, which inferred that the nucleation of $ZrW_2O_7(OH)_2 \cdot 2H_2O$ at a hydrothermal condition was completed within 12 h. However, the Ostwald ripening could give explanation to the observed general increase in crystallite and particles sizes as the reaction proceeded for longer than 12 h. Based on the efforts to control the morphologies of $ZrW_2O_7(OH)_2 \cdot 2H_2O$ nanoparticles, the careful selection of experimental parameters is crucial for optimizing the obtained nanoparticles to be used in composite applications.

Chapter 4 Characterization of thermal and physical properties of zirconium tungstate nanoparticles

4.1 Selection of zirconium tungstate nanoparticles for characterization

As the synthesis of zirconium tungstate nanoparticles with different morphologies was discussed in the prior chapter, it is important to study their negative thermal expansion properties and their potential hydration problems which were dependent upon the morphologies and crystallite sizes. Following the previous synthesis efforts, three types of $ZrW_2O_7(OH)_2 \cdot 2H_2O$ nanoparticles with different morphologies and crystallite sizes were chosen as the candidates for the characterization of their physical and thermal properties, as specified in Table 4-1. The morphologies of the three ZrW_2O_8 candidates are shown in Fig. 4-1 (a) through (f). As this table is compared with the morphologies of previous $ZrW_2O_7(OH)_2 \cdot 2H_2O$ nanoparticles, it was noted that though the change in crystal form, from tetragonal to a cubic crystal structure during the calcination process, was not accompanied by a change in the nanoparticle morphology.

Table 4-1 Physical description of three types of ZrW_2O_8 nanoparticles

Nanoparticle type	Raw materials	Experimental conditions	Morphology	Size-scales (nm)
1	$ZrO(ClO_4)_2 \cdot xH_2O$ and $Na_2WO_4 \cdot 2H_2O$	7M HCl, 12 h, 160 °C	Large, bundle-like rods	Length: 900-1400 Width: 80-130
2	$ZrO(NO_3)_2 \cdot xH_2O$ and $Na_2WO_4 \cdot 2H_2O$	7M HCl, 12 h, 130 °C	Large, rectangular rods	Length: 600-1200 Width: 70-120
3	ZrAc solution and $Na_2WO_4 \cdot 2H_2O$	7M HCl, 12 h, 130 °C	Small, capsule-like, short rods	Length: 100-400 Width: 40-60

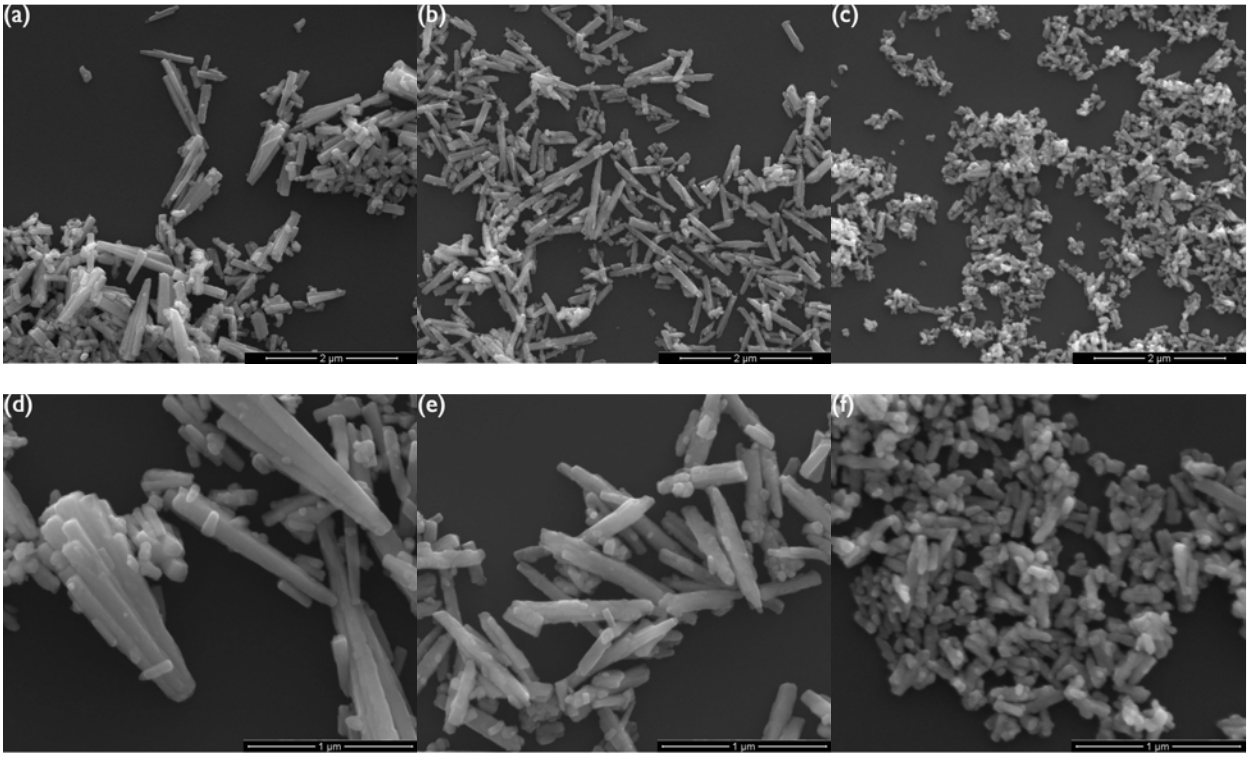

Fig. 4-1 SEM images of ZrW_2O_8 calcined at 600 °C for 30 min created under different hydrothermal conditions: $ZrO(ClO_4)_2 \cdot xH_2O$ / $Na_2WO_4 \cdot 2H_2O$ in 7M HCl at 160 °C for 12h at (a)20000X and (d)50000X, $ZrO(NO_3) \cdot xH_2O$ / $Na_2WO_4 \cdot 2H_2O$ in 7M HCl at 130 °C for 12 h at (b)20000X and (e)50000X, and ZrAc solution / $Na_2WO_4 \cdot 2H_2O$ in 7M HCl at 130 °C for 12 h at (c)20000X and (f)50000X

The TGA results indicated that the weight loss during the calcination process could be used to estimate the degree of dehydration from the precursor $ZrW_2O_7(OH)_2 \cdot 2H_2O$ to final product ZrW_2O_8. According to Fig. 4-2, the weight losses of the three chosen candidates under calcination were 10.66 wt%, 10.61 wt% and 10.85 wt%, respectively. Based on the weight loss values, it is possible to quantify the removal of hydrates and to deduce the reaction for the transition from $ZrW_2O_7(OH)_2 \cdot 2H_2O$ to ZrW_2O_8, which is shown as:

$ZrW_2O_7(OH)_2 \cdot 2H_2O \rightarrow ZrW_2O_8 + 3H_2O\uparrow$.

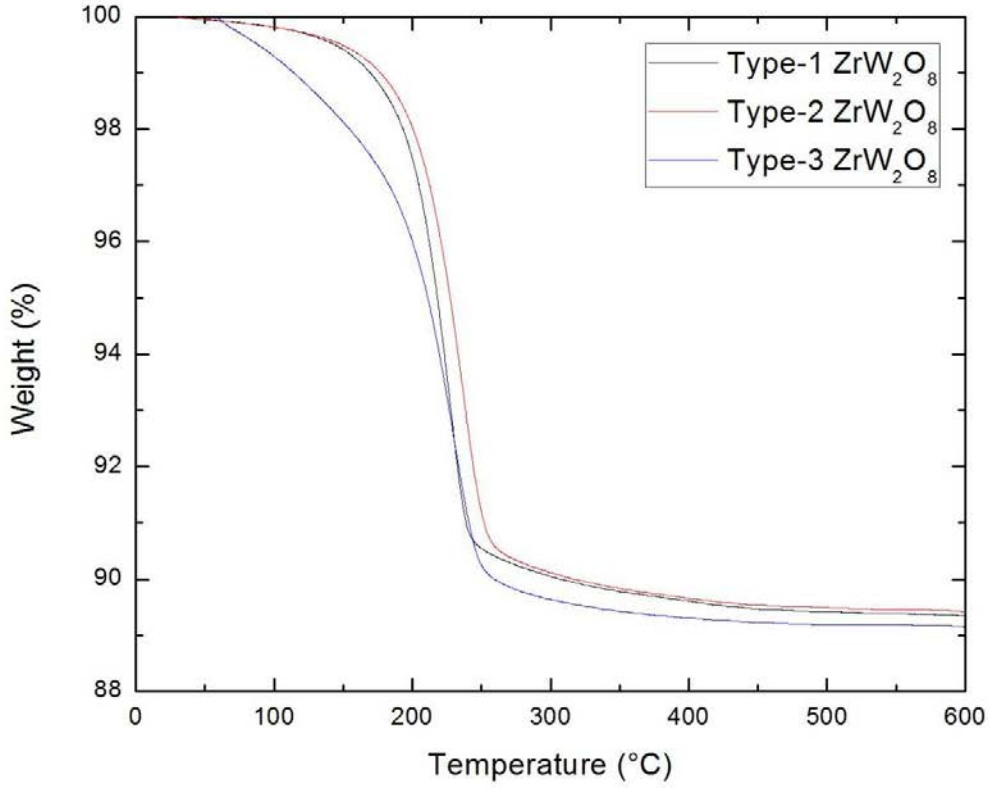

Fig 4-2. Weight loss of calcination to form ZrW_2O_8 from $ZrW_2O_7(OH)_2 \cdot 2H_2O$

4.2 Characterization of negative thermal expansion properties

The thermal properties of ZrW_2O_8 nanoparticles can be characterized by their NTE behavior using the coefficient of thermal expansion (CTE) value. The CTE value (α) can be derived from the XRD patterns according to equation (4-1):

$$\alpha = \frac{1}{a_0}\frac{da}{dT} \tag{4-1}$$

where a_0 is the initial lattice parameter and da/dT is the change in lattice parameter with temperature. The dependence of the lattice parameter on temperature for the three chosen ZrW_2O_8 nanoparticles was obtained from the isothermal XRD measurement shown in Fig. 4-3.

The error bar at each data point indicated the standard deviation of the two separate measurements at a temperature obtained during the first cooling and the following heating procedures. It was found that ZrW_2O_8 exhibited noticeable reductions in lattice parameters from 9.15 to 9.12 Å with a rise in temperature from 30°C to 600 °C for the three studied samples. This indicated that the unique NTE property of ZrW_2O_8. Also, as can be seen from the three curves of three types of nanoparticles they exhibited a significant change in slope at temperatures between 160°C and 170 °C for all three candidates. This can be attributed to a phase transition from the cubic α-phase to the β-phase, which was characterized by a disordered cubic lattice as discussed in chapter 1[7]. In addition, when performing the Rietveld refinement of the XRD patterns obtained from 70°C to 160 °C, it was necessary to refine both the α-phase and β-phase simultaneously to improve the quality of fit. This meant that the phase transition of ZrW_2O_8 does not occur suddenly but in a gradual process within a fixed temperature range. The initial β-phase ZrW_2O_8 first appears at 70 °C as a minor phase and the temperature is increased the content of the β-phase ZrW_2O_8 formed from the α-phase, and finally becomes the pure β-phase above 170 °C. The results obtained from the Reiveld refinements of the three types of ZrW_2O_8 nanoparticles with GSAS are summarized in Table 4-2.

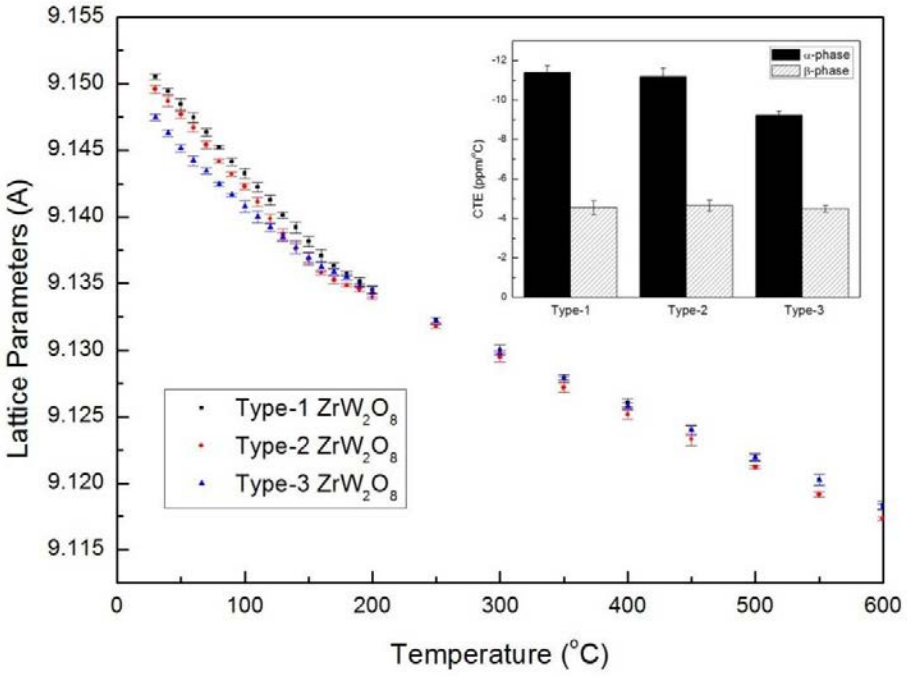

Fig. 4-3 Lattice parameter comparisons of three types of ZrW_2O_8 nanoparticles

Table 4-2 Rietveld refinements of different types of ZrW_2O_8 nanoparticles at various temperatures from 30 to 600 °C

Temperature (°C)	Type-1 nanoparticles			Type-2 nanoparticles			Type-3 nanoparticles		
	a (Å)	χ^2	R_{wp} (%)	a (Å)	χ^2	R_{wp} (%)	a (Å)	χ^2	R_{wp} (%)
30	9.15052 ± 0.00020	2.4	4.5	9.14959 ± 0.00030	3.4	4.8	9.14749 ± 0.00026	2.8	4.2
40	9.14946 ± 0.00023	2.1	4.3	9.14870 ± 0.00038	2.5	4.6	9.14627 ± 0.00025	3.1	4.5
50	9.14846 ± 0.00042	2.2	4.6	9.14770 ± 0.00026	2.3	4.5	9.14515 ± 0.00030	2.6	4.0
60	9.14748 ± 0.00036	3.5	4.1	9.14670 ± 0.00036	3.8	4.1	9.14422 ± 0.00036	2.9	4.8
70	9.14635 ± 0.00030	4.1	5.1	9.14540 ± 0.00029	4.2	5.3	9.14346 ± 0.00024	2.8	4.3
80	9.14522 ± 0.00013	4.5	5.3	9.14417 ± 0.00014	4.7	6.2	9.14244 ± 0.00014	3.9	5.7
90	9.14414 ± 0.00027	3.7	4.8	9.14321 ± 0.00016	4.9	6.8	9.14165 ± 0.00012	4.2	6.5
100	9.14329 ± 0.00036	4.2	5.8	9.14229 ± 0.00024	4.3	5.5	9.14081 ± 0.00041	4.9	6.3
110	9.14224 ± 0.00032	4.8	5.9	9.14114 ± 0.00035	5.1	5.6	9.14002 ± 0.00042	5.2	6.5
120	9.14126 ± 0.00036	4.8	5.6	9.13986 ± 0.00036	4.0	6.1	9.13923 ± 0.00033	4.9	5.9
130	9.14014 ± 0.00024	3.9	5.3	9.13869 ± 0.00044	3.8	5.6	9.13851 ± 0.00034	5.1	5.8
140	9.13922 ± 0.00041	4.0	4.6	9.13762 ± 0.00038	4.2	5.2	9.13772 ± 0.00048	4.0	6.7
150	9.13818 ± 0.00035	4.6	6.2	9.13684 ± 0.00045	5.2	6.7	9.13693 ± 0.00038	3.6	4.5
160	9.13707 ± 0.00047	4.2	5.8	9.13581 ± 0.00018	4.1	5.9	9.13624 ± 0.00038	4.8	5.6
170	9.13630 ± 0.00025	3.9	4.9	9.13525 ± 0.00029	4.1	5.3	9.13587 ± 0.00024	5.0	5.3
180	9.13572 ± 0.00019	3.0	4.7	9.13486 ± 0.00011	3.9	5.1	9.13550 ± 0.00021	4.4	6.2
190	9.13511 ± 0.00031	3.7	4.2	9.13458 ± 0.00017	3.4	4.6	9.13483 ± 0.00015	4.7	6.5
200	9.13452 ± 0.00026	4.5	5.5	9.13398 ± 0.00018	4.2	4.6	9.13435 ± 0.00038	3.9	5.6
250	9.13224 ± 0.00018	4.2	5.3	9.13180 ± 0.00016	3.2	4.9	9.13219 ± 0.00026	3.6	4.9
300	9.13003 ± 0.00036	4.8	6.3	9.12947 ± 0.00036	2.9	4.2	9.12982 ± 0.00016	3.4	4.8
350	9.12790 ± 0.00030	3.2	4.6	9.12715 ± 0.00035	3.5	4.5	9.12789 ± 0.00015	2.8	4.2

400	9.12602 ± 0.00032	3.8	4.6	9.12516 ± 0.00035	2.4	4.2	9.12578 ± 0.00025	2.1	5.3
450	9.12401 ± 0.00029	2.5	4.2	9.12329 ± 0.00045	4.3	5.6	9.12397 ± 0.00035	3.0	4.8
500	9.12196 ± 0.00029	2.7	4.3	9.12122 ± 0.00013	3.8	4.8	9.12193 ± 0.00023	4.2	6.0
550	9.12026 ± 0.00039	3.1	5.7	9.11917 ± 0.00020	4.5	6.2	9.12027 ± 0.00042	3.3	4.2
600	9.11838 ± 0.00030	3.2	5.2	9.11734 ± 0.00015	2.8	4.2	9.11823 ± 0.00025	2.6	4.6

The CTE values of three types of ZrW_2O_8 nanoparticles in their two phases are summarized in Table 4-3. Since the phase transition occurs in the temperature range of 70°C to 160 °C, the CTE value of the α-phase ZrW_2O_8 could be determined at a temperature between 30 °C to 90 °C. The pure or predominant α-phase existed and the CTE value of β-phase was estimated at higher temperature from 180°C to 600 °C. It was interesting to find that the nano-sized ZrW_2O_8 presented a slightly more negative CTE value than the bulk ZrW_2O_8 with reported a value of -8.8×10^{-6} °C^{-1} in α-phase, while keeping its β-phase consistent with the reported CTE value. In addition, the CTE of α-phase ZrW_2O_8 was found to be dependent on the crystallite size of the nanoparticles. The type-3 ZrW_2O_8 nanoparticles with crystallite sizes of approximate 32 nm showed CTE of -9.25×10^{-6} °C^{-1}. However, it was less negative compared with the CTE of nanoparticles that are type-1 (-11.4×10^{-6} °C^{-1}) and type-2 (-11.2×10^{-6} °C^{-1}) with relatively larger crystallite sizes of about 50 nm. Nonetheless, the effect of the crystallite sizes on the CTE values were weakened at higher temperatures after the phase transition, the CTE of the three types of ZrW_2O_8 in their β-phase exhibited similar CTE values of 4.55×10^{-6} °C^{-1}, 4.65×10^{-6} °C^{-1} and 4.94×10^{-6} °C^{-1} as indicated in Table 4-2. Based on the data, the ZrW_2O_8 nanoparticles with larger crystallite sizes seemed to be more promising in their NTE behavior. On the other hand, the nanoparticles with larger crystallite sizes displayed larger dimensional scales, which reduced the potential of decreased loadings of filler to produce nanocomposites. As a result, further study is needed to learn about which type of the ZrW_2O_8 nanoparticles can be used as filler and still yield the polymer nanocomposites with superior thermomechanical properties.

Table 4-3 CTE values of different types of ZrW_2O_8 nanoparticles

Nanoparticle type	Crystallite size (nm)	CTE value (ppm/°C)	
		α-phase	β-phase
1	50±4	-11.4±0.352	-4.55±0.341
2	46±4	-11.2±0.420	-4.65±0.283
3	32±5	-9.25±0.243	-4.94±0.161

4.3 Hydration of ZrW_2O_8 nanoparticles

As the ZrW_2O_8 nanoparticles undergo hydration it could have a detrimental effect of the negative CTE behavior and impact their potential for use as negative CTE fillers[36]. The understanding of the correlations between particle morphology and tendency for hydration was crucial for the synthesis purpose. Hence, in this work three types of ZrW_2O_8 nanoparticles were sealed in ambient conditions and placed in 20 ml vials for two weeks and two months respectively to observe the hydration phenomenon.

The hydration of ZrW_2O_8 nanoparticles could be identified by changes in X-ray diffraction patterns as suggested by previous works[35, 36]. The cubic lattice parameter changes from 9.12 to 8.95 Å as the insertion of water into frame structure forms $ZrW_2O_8 \cdot 1H_2O$. In this experiment, the hydration of ZrW_2O_8 nanoparticles was also observed in all the samples that were exposed to the ambient atmosphere. Type-3 ZrW_2O_8 nanoparticles were used to compare the changes in the XRD patterns during the hydration process. As shown in Fig. 4-4, the hydrated nanoparticles appeared differently in the XRD patterns from the pristine nanoparticles'. The particles which underwent hydration for 2 weeks showed broader peaks and as the hydration process continued further, the pattern displayed a shift in all the peaks to higher angles and several peaks disappeared completely. This resulted the cubic phase with a smaller lattice constant.

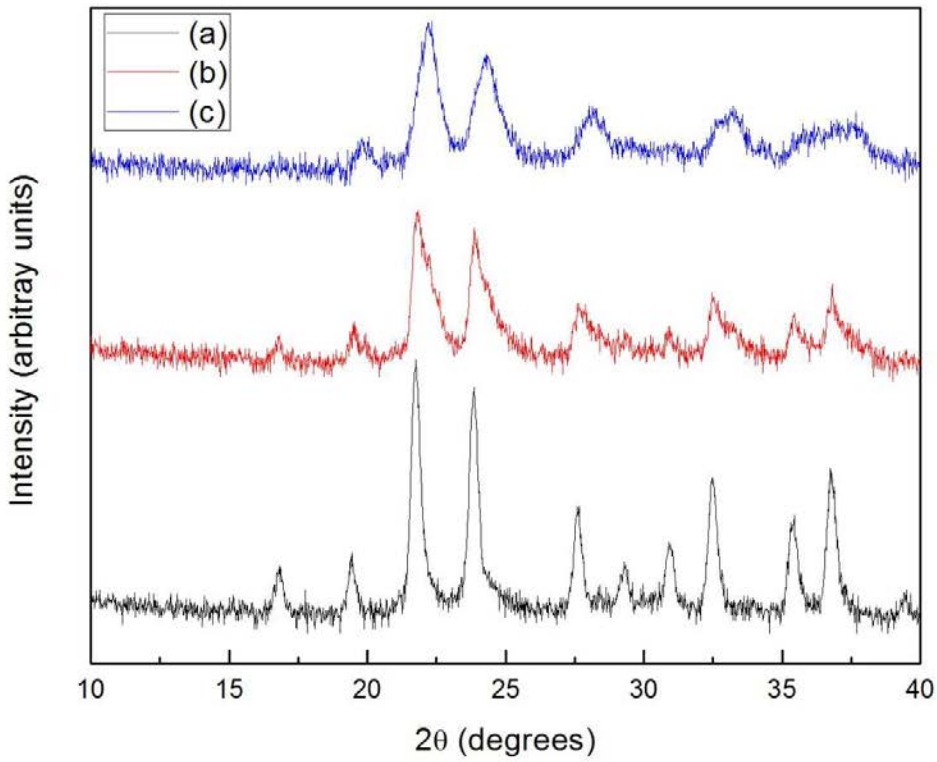

Fig. 4-4 X-ray diffraction patterns of ZrW_2O_8 nanoparticles for (a) newly prepared, (b) hydrated for 2 weeks, and (c) hydrated for 2 months

Subsequently, TGA was employed to quantify the extent of the hydration based on the weight loss by heating samples up to 190 °C. As shown in Fig. 4-5, an increase in storage time from two weeks to two months resulted in a higher degree of hydration due to the greater weight loss. Furthermore, for any given storage time the three types of ZrW_2O_8 nanoparticles displayed different extents of hydration. For example, among the samples stored for 2 months, type-1 nanoparticles showed the lowest weight loss (1.36 wt%) followed by type-2 ZrW_2O_8 with 1.75 wt% weight loss. Type-3 nanoparticles exhibited the most severe hydration phenomena, and exhibited a total weight loss of 2.26 wt%. Banek, N. and coworkers[36] first indicated that the

origin of nano-sized ZrW_2O_8 hydration was attributed to the increasing defect cites on the surface of nanoparticles. As the recent work done by our research group[42] shows, moisture adsorption and the surface area of the ZrW_2O_8 particles played a significant role in extent of hydration. The reason for differences in the amount of hydrates in each type of ZrW_2O_8 should be investigated from the physical properties of the nanoparticles.

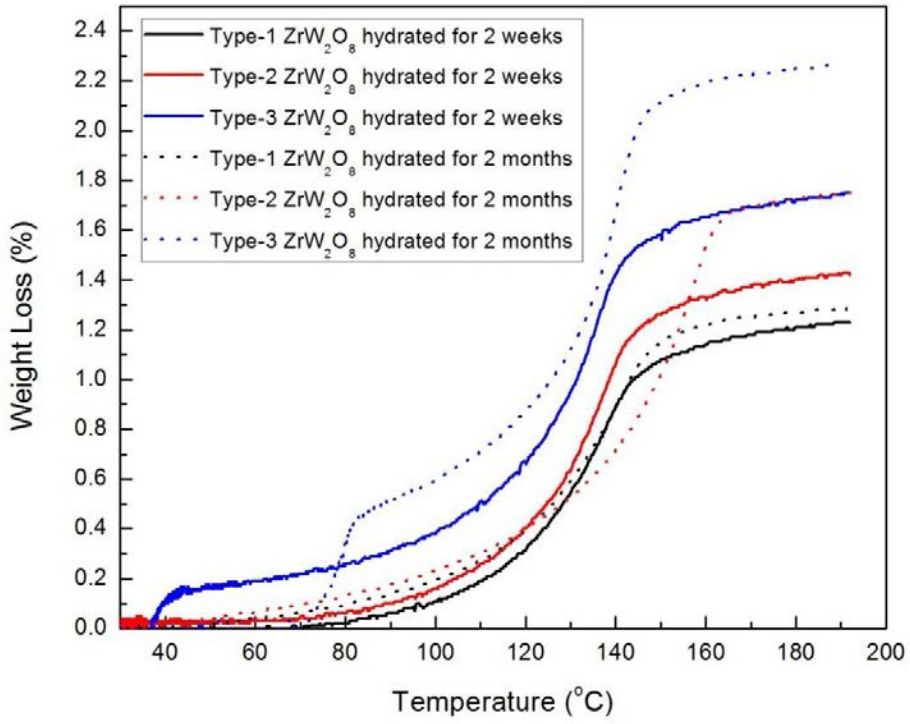

Fig. 4-5 Comparison of weight loss of hydration contents in ZrW_2O_8 nanoparticles synthesized under different experimental conditions

4.4 Characterization of pore structures of ZrW_2O_8 nanoparticles

To investigate differences in the extent of hydration for the different types of ZrW_2O_8 nanoparticles and causes for that hydration, it is necessary to understand the differences in their physical properties, such as pore structures.

As a solid is exposed to a gas or vapor it begins to adsorb its surroudnings by increasing mass or decreasing its pressure, the amount of adsorbed gas or vapor will reach a final fixed value, which can be quantified in the volume of a solids pores. The adsorbed film formed at lower pressures serves as the nucleus for condensation at a higher relative pressure. However, during the evaporation process, there is no need for nucleation and evaporation occurs as long as the pressure reaches a low level. Due to the processes of condensation and evaporation the hysteresis loop is present as a result. In this experiment, pore structures of ZrW_2O_8 nanoparticles were characterized by isotherm curves of N_2 adsorption-desorption shown in Fig. 4-6. It was noticeable that all three types of ZrW_2O_8 nanoparticles exhibited similar type IV isotherm curves with a typical characteristic hysteresis loops present for both the adsorption and desorption processes. This type model for isotherm curves was proposed by Zisgmondy, who assumed that the initial part of the isotherm at lower pressures, adsorption is restricted to a thin layer on the surface of sample until at higher relative pressure is reached. Then the N_2 starts to push into the surface and fill in voids in the samples, this process is called capillary condensation. As the pressure is continuously increased, more and more pores are filled until the entire system is full of condensation at the saturation pressure. In this case, at low relative pressures ($P/P_0 < 0.8$), the absorption of N_2 was restricted to the surface of particles to form thin multilayers resulting in a slow linear increase of N_2 adsorption with increasing pressure. At higher relative pressures ($P/P_0 > 0.8$), the N_2 adsorption-desorption curves of the three types of synthesized ZrW_2O_8 nanoparticles

exhibited significant increases in quantity of N_2 absorption due to capillary condensation. A significant drop in desorption of N_2 from the isotherm curve occurred by evacuating pressure indicated the possible shape of pores, which could be described as ink-bottle type. In addition, it was found that noticeable differences in the extent of the N_2 adsorption were displayed among the three types of ZrW_2O. Since the amount of N_2 adsorption represents the pore volume in the samples, and type-1 ZrW_2O_8 showed the lowest quantity of adsorbed N_2 it then had the lowest pore volumes, which is followed by type-2 nanoparticles, and type-3 ZrW_2O_8 exhibited highest level of adsorbed N_2 and with the largest pore volumes.

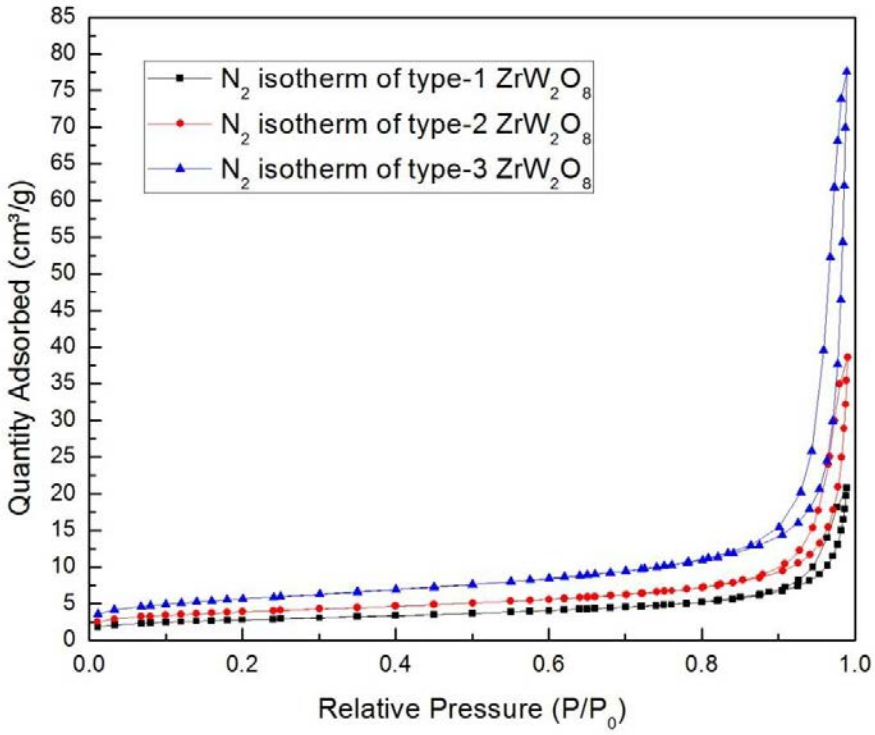

Fig. 4-6 Comparison of N_2 adsorption-desorption isotherms of ZrW_2O_8 nanoparticles synthesized under different experimental

The pore size distribution curves were obtained by Barret-Joyner-Halenda (BJH) desorption of N_2 isotherms. From the hysteresis of adsorption and desorption, it makes it possible to calculate the pore sizes based on the Kelvin equation (4-2)

$$ln\frac{p}{p^0} = -\frac{2\gamma V_L}{RT}\frac{1}{r_m} \quad (4\text{-}2)$$

Where, V_L is the molar volume of the liquid adsorptive, p/p^0 is relative pressure of the vapor in equilibrium, γ is surface tension, and r_m is mean radius of curvature given by:

$$\frac{1}{r_1} + \frac{1}{r_2} = \frac{2}{r_m} \quad (4\text{-}3)$$

As shown in Fig. 4-7, the three types of nanoparticles exhibited a broad pore size distribution ranging from 10 to 100 nm with majority of pore volumes concentrated at approximately 50 nm. Based on the conventional classification of pores according to their average width, the synthesized three ZrW_2O_8 nanoparticles are characterized as mesopores. In addition, a significantly higher pore volume was observed for type-1 nanoparticles in comparison to type-2 and type-3 particles, which was in good agreement with the results obtained from Fig. 4-6.

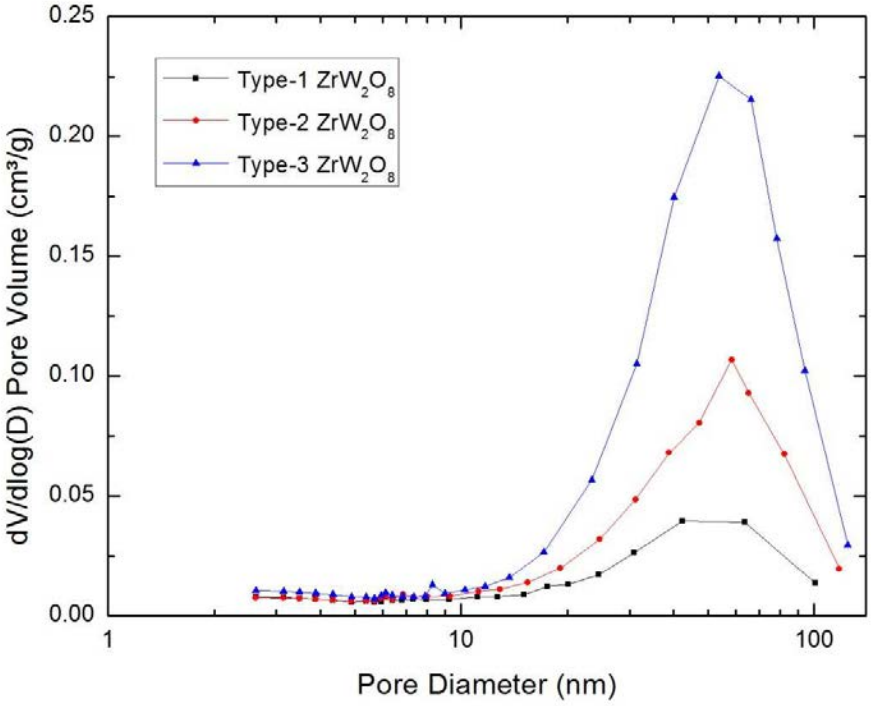

Fig. 4-7 Comparison of BJH pore size distribution of ZrW_2O_8 nanoparticles synthesized under different experimental conditions

4.5 Study on correlation of hydration and pore structures in ZrW_2O_8 nanoparticles

Table 4-4 summarized the pore properties and TGA weight loss for the three selected ZrW_2O_8 nanoparticle types. It was found that size scales of the nanoparticles influenced the pore structures significantly. Type-1 ZrW_2O_8, exhibited a morphology resembling a large bundle rods, showed the smallest BET surface area (9.96 m^2/g), the smallest total pore volume (0.0280 cm^3/g), and the smallest average pore size (18.5 nm). In comparison to type-1 particles, type-2 ZrW_2O_8 were characterized by a morphology resembling long individual rods, and had a greater BET surface area (13.9 m^2/g), higher pore volume (0.0541 cm^3/g), and higher average pore diameter (25.5 nm). Among the three types of particles, the type-3 ZrW_2O_8 had the smallest particles sizes,

exhibited the largest values in surface area (20.3 m^2/g), total pore volume (0.114 cm^3/g), and pore diameter (30.5 nm). The correlation between particles size-scales and the pore structures could be explained by the degree of agglomeration within the nanoparticles. The formation of pore structures in samples was greatly dependent on the dimensional scale of ZrW_2O_8 nanoparticles. Due to the tendency of nano-sized particles to agglomerate together, caused by a strong electrostatic attraction on their surface, smaller particle tend to create more voids among them thus causing pores with larger volumes and sizes.

Table 4-4 Pore structures and hydrate weight loss of different types of ZrW_2O_8 nanoparticles

Nanoparticles type	Particle size (nm)	BET surface area (m^2/g)	BJH cumulative pore volume (cm^3/g)	BJH desorption average pore diameter (nm)	Weight loss (wt%)	
					2 weeks	2 months
1	Length: 900-1400 Width: 80-130	9.96	0.0280	18.5	1.23	1.36
2	Length: 600-1200 Width: 70-120	13.9	0.0541	25.5	1.43	1.75
3	Length: 100-400 Width: 40-60	20.3	0.114	30.5	1.73	2.26

From Table 4-4, it was interesting to notice that the pore volumes and diameters in nanoparticles played a crucial role in the hydration process during storage in an ambient environment. The observation of type-1 ZrW_2O_8 nanoparticles exhibited the lowest degree of hydration among the three types of samples and could be explained by the fact that the moisture was less likely to be adsorbed by particles with a lower total pore volume and smaller average pore diameter. Type-3 ZrW_2O_8 nanoparticles showed the largest pore volumes and diameters and consequently underwent greater degrees of hydration. On the other hand, the observed time dependent process of hydration also could be explained by the pore structures effects on moisture

adsorption. As the adsorbed hydrate molecules began to occupy pores, less space was left for further adsorption of the hydrates from the environment. This resulted in fewer amounts of hydrates to be adsorbed as times goes on until finally it reaches a saturation point. Consequently the hydration rate was faster at beginning of the process than in later periods of time as observed experimentally.

4.6 Conclusion

Detailed studies on the analysis of the thermal and physical properties of three types of ZrW_2O_8 nanoparticles with distinct morphologies and crystallites sizes were investigated in this chapter. First, the morphologies of the nanoparticles can be preserved during the calcination process to transform the precursor $ZrW_2O_7(OH)_2 \cdot 2H_2O$ to cubic ZrW_2O_8. Regarding CTE values for nano-sized ZrW_2O_8, it was found that the NTE property effects the crystallite sizes of the synthesized nanoparticles. ZrW_2O_8 with larger crystallite sizes displayed more negative CTE values in the α-phase, but there was no obvious influence on CTE values in the β-phase. In addition, the hydration of nano-sized ZrW_2O_8 was studied by characterizing the content of the hydrates using X-ray diffraction patterns and pore structures with different techniques. A possible interpretation of the hydration problem for ZrW_2O_8 nanoparticles was originated from the moisture adsorption caused by the formation of pores within the nanoparticles. Based on the correlation among the degree of hydration, particle size, and pore size, it was suggested that ZrW_2O_8 nanoparticles with smaller sizes tended to create larger pores and underwent the most severe hydration problems.

Chapter 5. Summary and Future works

Precursors with different morphologies to the nanoparticulate $ZrW_2O_7(OH)_2 \cdot 2H_2O$ were successfully synthesized with a hydrothermal reaction by controlling various experimental conditions. To study each synthetic variables' effect on the morphologies of the nanoparticles, a series of systematic research trails comparing the morphologies and crystallite sizes of $ZrW_2O_7(OH)_2 \cdot 2H_2O$ nanoparticles were conducted. This includes different initial raw materials, acid types, acid concentrations, reaction times, and reaction temperatures. Based on the experiments, the $ZrW_2O_7(OH)_2 \cdot 2H_2O$ nanoparticles were synthesized with various morphologies by utilizing different initial reactants, and $Na_2WO_4 \cdot 2H_2O$ was chosen as the optimized tungsten source for a reaction since the yielded nanoparticles displayed optimized homogenous size distribution and an overall smaller size. The acidic medium was an important factor in controlling the nanoparticles' morphologies and crystallite size as well. The $ZrW_2O_7(OH)_2 \cdot 2H_2O$ nanoparticles displayed individual and well defined shapes as the reaction proceeded in HCl. Higher concentrations of HCl caused rougher surfaces on the particle than lower concentrations. However, the nanoparticle obtained from the $HClO_4$ solution showed different levels of agglomeration by joining the thin individual nanoparticles lengthwise, and the extent of agglomeration was found to be higher in an acidic medium of a higher concentration. In case of reaction temperature, the larger nanoparticles in both dimensional size and crystallite size were found at higher temperatures indicating that a hydrothermal temperature influenced the kinetic nucleation and crystal growth of $ZrW_2O_7(OH)_2 \cdot 2H_2O$ nanoparticles. The comparison of reaction times in this study suggested that the observation of increasing crystallite sizes in a few systems, was due to the Ostwald ripening phenomena during synthesis. Also there are no significant

changes in the formation of nanoparticles under the hydrothermal condition after 12 h, so the nucleation of nanoparticles was carried on within a 12 h time frame.

The three types of ZrW_2O_8 nanoparticles synthesized under different reaction conditions, were selected for the investigation of negative thermal expansion behaviors dependent upon their morphologies and crystallite sizes. As expected, all three nanoparticles displayed a phase transition between α and β-ZrW_2O_8 at about 170 °C during the measurement. The magnitude of the negative CTE was found to increase with increasing crystallite size of ZrW_2O_8 in the α-phase. It was found that type-1 and type-2 nanoparticles with larger crystallite sizes (~50 nm) present more negative CTE values in α-ZrW_2O_8, which were about -11 ppm/°C. However, the CTE of the three ZrW_2O_8 nanoparticles in the β-phase showed nearly identical values the previously reported values at -4.9 ppm/°C, regardless of crystallite size.

In this work, the hydration problems of the three synthesized ZrW_2O_8 nanoparticles were observed and analyzed. They were identified by the differences in their X-ray diffraction patterns between the pristine and hydrated ZrW_2O_8 and the weight loss of the contents upon heating. Also hydration can be described as a time-dependent procedure due to longer exposure periods resulting in higher hydration contents, and a hydration rate was found to be faster in the initial period than as the reaction progressed. To understand the hydration problem happening in nano-sized ZrW_2O_8, characterization of the physical properties of nanoparticles provided considerable evidence to explore the explanation. The origin of hydration for nano-sized ZrW_2O_8 resulted from the moisture adsorption caused by the formation of pores among the nanoparticles. As nanoparticles exhibited a higher tendency of agglomeration, they tended to aggregate together and create voids among each particle. These voids can be regarded as pores that serve in adsorbing and storing moisture from environment. Also, it was found that the pores dimensions

were greatly dependent on the nanoparticles sizes. In this experiment, ZrW_2O_8 nanoparticles with smaller sizes produced larger pore diameters and total pore volume showed a greater tendency of hydration problems. A candidate with a tendency for hydration problems was not a promising candidate for using as a filler in nanocomposites applications.

Following the efforts on synthesis and characterization of zirconium tungstate nanoparticles, it will be important to investigate the effects of ZrW_2O_8 nanoparticles with different morphologies on the properties of their polymer nanocomposites. The three types of studied ZrW_2O_8 nanoparticles in this work can be applied as nano-fillers to incooperate with different types of polymer matrices, such as epoxy resin and bisphenol E cyanate ester, to study their effects on the thermo-mechanical and dielectric properties of nanocomposites.

References

[1] A. W. Sleight Inorg. Chem. 1998; 37: 2854-2860.

[2] J. S. O. Evans Journal of the Chemical Society-Dalton Transactions 1999; 3317-3326.

[3] J. S. O. Evans, T. A. Mary and A. W. Sleight Physica B 1997; 241: 311-316.

[4] V. Korthuis, N. Khosrovani, A. W. Sleight, N. Roberts, R. Dupree and W. W. Warren, Jr. Chemistry of Materials 1995; 7: 412-417.

[5] A. K. A. Pryde, K. D. Hammonds, M. T. Dove, V. Heine, J. D. Gale and M. C. Warren Journal of Physics-Condensed Matter 1996; 8: 10973-10982.

[6] C. Lind, A. P. Wilkinson, Z. B. Hu, S. Short and J. D. Jorgensen Chemistry of Materials 1998; 10: 2335-2336.

[7] T. A. Mary, J. S. O. Evans, T. Vogt and A. W. Sleight Science 1996; 272: 90-92.

[8] J. S. O. Evans, T. A. Mary, T. Vogt, M. A. Subramanian and A. W. Sleight Chemistry of Materials 1996; 8: 2809-2823.

[9] J. S. O. Evans, T. A. Mary and A. W. Sleight J. Solid State Chem. 1997; 133: 580-583.

[10] J. S. O. Evans, T. A. Mary and A. W. Sleight J. Solid State Chem. 1998; 137: 148-160.

[11] L. L. Y. Chang, M. G. Scroger and B. Phillips Journal of the Less Common Metals 1967; 12: 51-56.

[12] J. S. O. Evans, W. I. F. David and A. W. Sleight Acta Crystallographica Section B-Structural Science 1999; 55: 333-340.

[13] A. K. A. Pryde, K. D. Hammonds, M. T. Dove, V. Heine, J. D. Gale and M. C. Warren Phase Transit. 1997; 61: 141-153.

[14] J. S. O. Evans, Z. Hu, J. D. Jorgensen, D. N. Argyriou, S. Short and A. W. Sleight Science 1997; 275: 61-65.

[15] C. A. Perottoni and J. A. H. da Jornada Science 1998; 280: 886-889.

[16] T. Varga, A. P. Wilkinson, C. Lind, W. A. Bassett and C. S. Zha Solid State Commun. 2005; 135: 739-744.

[17] T. Varga, A. P. Wilkinson, A. C. Jupe, C. Lind, W. A. Bassett and C. S. Zha Phys. Rev. B 2005; 72:

[18] C. A. Figueiredo, J. Catafesta, J. E. Zorzi, L. Salvador, I. J. R. Baumvol, M. R. Gallas, J. A. H. da Jornada and C. A. Perottoni Phys. Rev. B 2007; 76: 184201(1-7).

[19] D. A. Keen, A. L. Goodwin, M. G. Tucker, M. T. Dove, J. S. O. Evans, W. A. Crichton and M. Brunelli Physical Review Letters 2007; 98: 225501 (1-4).

[20] T. Varga and A. P. Wilkinson Phys. Rev. B 2009; 79: 224119 (1-5).

[21] J. Graham, A. D. Wadsley, J. H. Weymouth and L. S. Williams J. Am. Ceram. Soc. 1959; 42: 570-570.

[22] C. Lind and A. P. Wilkinson J. Sol-Gel Sci. Technol. 2002; 25: 51-56.

[23] A. P. Wilkinson, C. Lind and S. Pattanaik Chemistry of Materials 1999; 11: 101-108.

[24] M. S. Dadachov and R. M. Lambrecht J. Mater. Chem. 1997; 7: 1867-1870.

[25] C. Georgi and H. Kern Ceram. Int. 2009; 35: 755-762.

[26] L. M. Sullivan and C. M. Lukehart Chemistry of Materials 2005; 17: 2136-2141.

[27] Q. F. Xing, X. R. Xing, R. B. Yu, L. Du, J. Meng, J. Luo, D. Wang and G. R. Liu J. Cryst. Growth 2005; 283: 208-214.

[28] X. R. Xing, Q. F. Xing, R. B. Yu, J. Meng, J. Chen and G. R. Liu Physica B 2006; 371: 81-84.

[29] J. A. Colin, D. V. Camper, S. D. Gates, M. D. Simon, K. L. Witker and C. Lind J. Solid State Chem. 2007; 180: 3504-3509.

[30] L. C. Kozy, M. N. Tahir, C. Lind and W. Tremel J. Mater. Chem. 2009; 19: 2760-2765.

[31] S. Allen, N. R. Warmingham, R. K. B. Gover and J. S. O. Evans Chemistry of Materials 2003; 15: 3406-3410.

[32] J. Yang, Q. Q. Liu, X. J. Sun, G. F. Xu and X. N. Cheng Ceram. Int. 2009; 35: 441-445.

[33] M. I. Ahmad, K. Lindley and M. Akinc J. Am. Ceram. Soc. 2011; 94: 2619-2624.

[34] Q. Q. Liu, J. Yang, X. J. Sun, X. N. Cheng, G. F. Xu and X. H. Yan J. Mater. Sci. 2007; 42: 2528-2531.

[35] N. Duan, U. Kameswari and A. W. Sleight J. Am. Chem. Soc. 1999; 121: 10432-10433.

[36] N. A. Banek, H. I. Baiz, A. Latigo and C. Lind J. Am. Chem. Soc. 2010; 132: 8278-8279.

[37] X. B. Yang, J. Xu, H. J. Li, X. N. Cheng and X. H. Yan J. Am. Ceram. Soc. 2007; 90: 1953-1955.

[38] X. Yan, X. Cheng, G. Xu, C. Wang, S. Sun and R. Riedel Materialwiss. Werkstofftech. 2008; 39: 649-653.

[39] J. Tani, H. Kimura, K. Hirota and H. Kido J. Appl. Polym. Sci. 2007; 106: 3343-3347.

[40] P. Badrinarayanan, B. Mac Murray and M. R. Kessler J. Mater. Res. 2009; 24: 2235-2242.

[41] X. G. Zheng, KubozonoH, YamadaH, KatoK, IshiwataY and C. N. Xu Nat Nano 2008; 3: 724-726.

[42] P. Badrinarayanan, M. I. Ahmad, M. Akinc and M. R. Kessler Materials Chemistry and Physics 2011; 131: 12-17.

[43] E. Foo, M. Jaafar, A. Aziz and L. C. Sim Composites Part A: Applied Science and Manufacturing 2011; 42: 1432-1437.

[44] P. Badrinarayanan and M. R. Kessler Compos. Sci. Technol. 2011; 71: 1385-1391.

[45] C. Lind, M. R. Coleman, L. C. Kozy and G. R. Sharma Phys. Status Solidi B-Basic Solid State Phys. 2011; 248: 123-129.

[46] S. Brunauer, P. H. Emmett and E. Teller J. Am. Chem. Soc. 1938; 60: 309-319.